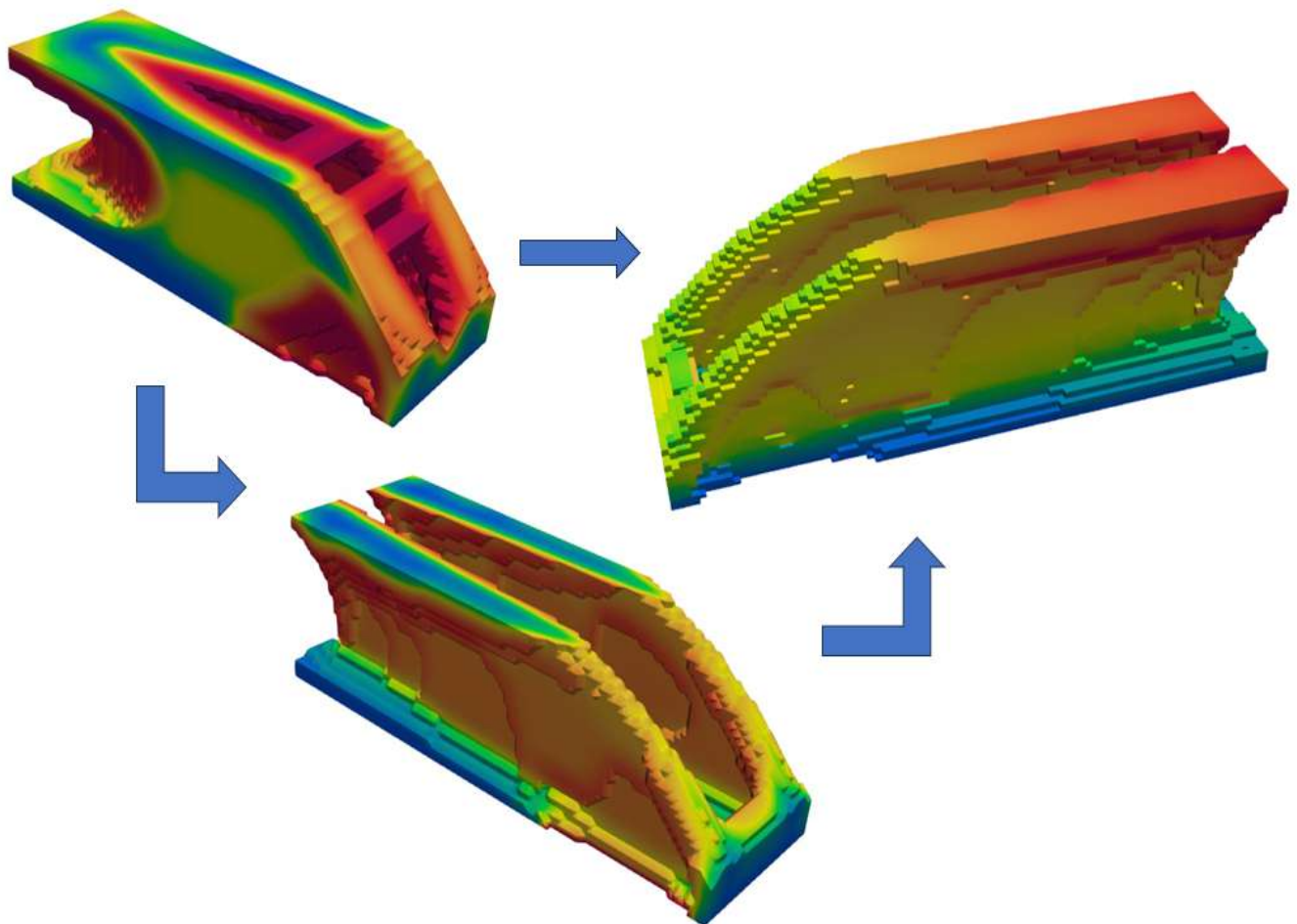


Department of Precision and Microsystems Engineering

A geometric approach for controlling local overheating in topology optimization for additive manufacturing

Manabendra Nath S. Das

Report no : 2023.068
Coach : Dr. Ir. Rajit Ranjan, Ir. Kai Wu
Professor : Dr. Ir. Can Ayas, Dr. Jun Wu
Specialisation : Computational Design and Mechanics
Type of report : M.Sc. Thesis
Date : 29 August 2023



A geometric approach for controlling local overheating in topology optimization for additive manufacturing

by

M.N.S. Das

to obtain the degree of Master of Science
at the Delft University of Technology,
to be defended publicly on Tuesday August 29, 2023 at 15:30 PM.

Student number:	5501113	
Project duration:	September 1, 2022 – August 29, 2023	
Thesis committee:	Dr. ir. Can Ayas,	TU Delft-3ME-PME
	Dr. Jun Wu,	TU Delft-IDE-SDE
	Prof. dr. ir. Matthijs Langelaar	TU Delft-3ME-PME
	Dr. ir. Trayana Tankova	TU Delft-CITG-ES

An electronic version of this thesis is available at <http://repository.tudelft.nl/>.

Acknowledgement

I would like to express my heartfelt gratitude to all those who have been instrumental in the successful completion of my master's thesis during my time at TU Delft, specializing in high-tech engineering in Mechanical Engineering. This journey spanned a dedicated year of rigorous effort, and I am truly thankful for the support and encouragement I received along the way.

First and foremost, I extend my sincere appreciation to Can and Jun for their guidance and expertise. Your valuable insights and unwavering encouragement played a pivotal role in shaping the direction of my research and inculcating a deeper understanding of the subject matter. I am deeply indebted to my daily supervisors, Kai and Rajit, for their constant support and mentorship throughout this endeavor. Your guidance, feedback, and patience have been invaluable, allowing me to navigate through the challenges and complexities of my research with confidence. The regular weekly meetings and discussions were crucial in keeping everyone on the same page and the project on track at all times. This thesis wouldn't have been possible without your help and guidance. Also, I would like to thank my space-time topology group colleagues without whom the thesis wouldn't have been as interesting as it was.

Though the research wasn't initially within my comfort zone, I committed myself wholeheartedly to the task. I would like to acknowledge the ups and downs that dotted this journey, and my unwavering determination to persevere. Overcoming these hurdles has been a defining experience for me. I must express my heartfelt gratitude to my family members for their unwavering belief in me and their unending love and support. Your constant encouragement provided me with the strength to overcome obstacles and reach this significant milestone. In times of struggle, it was the support of dear friends that illuminated the path ahead. My friends Shreya and Dhanesh stood by me through thick and thin, offering solace and encouragement when it was needed most. To my group of friends, the "Pitstop Bois," thank you for being a constant source of motivation and camaraderie. Maintaining a healthy body and mind has been integral to my journey. Engaging in sports and focusing on well-being not only provided respite from the academic rigors but also contributed to a holistic growth process. Lastly, I would like to express my gratitude to my team Formula Student Team Delft for making the 2 years of my Master's the best time of my life.

With this thesis, I aim to express my growing interest in the realm of research and my willingness to contribute to its advancement. My time at TU Delft has been transformative, and I cherished every second of it. The joy of learning and the thrill of discovery has left an indelible mark on me, and I look forward to a future where I can apply and further cultivate the knowledge and skills gained during this period.

Once again, I extend my heartfelt appreciation to all those who have played a role in this significant achievement. Your collective support has made this journey not just successful, but also deeply enriching.

Thank you.

M.N.S. Das
Delft, August 2023

Summary

Additive manufacturing (AM) has revolutionized the way parts are manufactured by increasing the design freedom and ability to fabricate intricate design structures. The increase in form freedom offered by AM is best capitalized by computational design tools such as topology optimization (TO). AM provides unprecedented design advantages over other traditional manufacturing techniques. However, there are some immanent manufacturing constraints that should be imposed during the design stage to ensure manufacturability of the parts. One such constraint is the issue of local overheating in parts, a prevalent source of defects and part distortion in metal additive manufacturing. Overheating in AM is a thermal phenomenon that is caused by the overshooting of temperatures above the melting point. Overheating during the AM process can cause diminished mechanical properties, build failures, and dimensional inaccuracy in the parts.

Overheating in parts is usually associated with overhangs and attempts have been made to control the overhangs below a threshold value as a constraint in TO. However, it has been studied in the literature that overhang avoidance does not ensure designs are free from local overheating. Earlier a physics-based hotspot constraint utilizing a simplified thermal model has been used to generate a topological optimized structure limiting overheating. However, for high-resolution models, the computation becomes cumbersome. Also, the method is currently not suitable for parts that have a curved layer deposition. To tackle these issues certain contributions are made in this thesis:

- Development of a geometry-based hotspot detection approach that estimates the local conductivity by evaluating the material distribution in the vicinity of each element. The local conductivity information is used to generate the temperature field (hotspot map) which gives a qualitative estimate of the overheating risk in parts.
- Integration of the geometry-based hotspot detection method as a constraint in TO to suppress the features that cause local overheating by optimizing the structural layout.
- Integration of the geometry-based hotspot detection method in space-time topology optimization (STTO) to limit the risk of local overheating in parts whose structural layout and fabrication sequence are optimized simultaneously.

The optimized structures are compared with currently existing methods that limit the risk of local overheating. It is found that the geometry-based constraint for local overheating has a huge computational advantage over other methods. Also, the maximum temperature that is obtained from the transient simulation as a post-analysis step was comparable with the existing physics-based method. As a result, this geometry-based strategy has successfully added to the toolbox of techniques used to reduce the severity of overheating in AM-produced metal parts.

Contents

Acknowledgement	i
Summary	ii
1 Introduction	1
1.1 Background	1
1.1.1 Introduction to Additive Manufacturing	1
1.1.2 Integration of AM with Topology Optimization	3
1.2 Problem Statement: Overheating issues associated with AM	4
1.3 State of the art	5
1.4 Gap in the state of the art	5
1.4.1 Computational efficiency when incorporating AM thermal models with TO	5
1.4.2 Incorporation with various AM methods	6
1.5 Contributions	6
1.5.1 Geometry-based method to detect and prevent local overheating	6
1.6 Thesis structure	7
2 Literature Study	8
2.1 State of the art	8
2.1.1 Heat accumulation prevention	8
2.1.2 Thermal models for Additive Manufacturing	8
2.1.3 Introduction to density-based topology optimization	9
2.1.4 Physics-based method for detecting and preventing local overheating	11
3 A geometric approach for controlling local overheating in topology optimization for additive manufacturing	14
3.1 Introduction	15
3.2 Geometry-based hotspot detection method	16
3.2.1 Conductivity estimation	17
3.2.2 Using penalization to capture actual behavior of heat conduction in AM	18
3.2.3 Determination of the conductivity estimation filter radius	18
3.2.4 Application of conductivity estimation filter in detecting overheating zones in geometries	19
3.2.5 Comparison of conductivity estimation with current hotspot detection approaches	20
3.3 Integration with Topology Optimization (TO)	22
3.3.1 Formulation of conductivity estimation method as a constraint	22
3.3.2 Topology optimization problem	23
3.3.3 Topology optimization result using hotspot constraint	25
3.4 Reformulation of constraint	25
3.4.1 Determination of critical temperature T_{cr}	27
3.4.2 Robust formulation on the design	28
3.5 Parameter study	30
3.5.1 Influence of conductivity penalization and interpolation factor	30
3.5.2 Influence of critical temperature T_{cr}	32
3.5.3 Influence of conductivity filter radius cf	34
3.6 Comparison between different designs used for controlling local overheating	36
3.6.1 Temperature results from transient LBPf process simulation	36
3.6.2 Computation time comparison	39
3.7 Extension to 3D	39
3.8 Conclusion	42

4	Integration with Space-time Topology Optimization	44
4.1	Introduction to space-time topology optimization	44
4.1.1	Background	44
4.1.2	Space-time topology optimization	45
4.1.3	Intermediate structures	45
4.1.4	Volume and continuity constraints on intermediate structures	46
4.2	Hotspot detection in STTO designs using conductivity estimation method	47
4.2.1	Modifications to conductivity estimation filter to incorporate with STTO	47
4.3	Influence of both fabrication sequence and structural layout to limit the heat accumulation	49
4.3.1	STTO problem formulation	49
4.4	Results for different fabrication sequences	51
5	Discussion and Recommendations	53
5.1	Shortcomings of the conductivity estimation method in detecting hotspots	53
5.1.1	Cluster operator	54
5.1.2	Results	56
5.2	Future scope	57
6	Conclusions	58
	References	59
A	Appendix for Chapter-3	62
A.1	Influence of nonlinear weights and different conductivity filter size for the conductivity estimation method	62
A.2	Comparison of conductivity estimation method on geometry obtained from overhang filter	65
A.3	Analytical sensitivities for the hotspot constraint	66
A.4	Hotspot constraint on eroded, intermediate, and dilated designs	67
A.5	Compliance and max temperature values for different q and r values	68
A.6	Robust TO with hotspot constraint with different load cases and boundary conditions	68
B	Appendix for Chapter-4	71
B.1	Analytical sensitivities for the hotspot constraint for STTO	71

1

Introduction

1.1. Background

Additive manufacturing (AM) has gained a lot of importance in the manufacturing industries. It refers to technologies that grow three-dimensional objects layer-by-layer. Each successive layer bonds to the preceding layer of melted or partially melted material. Its undeniable advantage, which distinguishes it from conventional production techniques such as milling, forging, or casting, is the design freedom it gives for producing highly intricate geometries. The material wasted in manufacturing the part is negligible as compared to other traditional manufacturing techniques. The advantages of additive manufacturing are best utilized with topology optimization (TO). Topology optimization is a tool that optimizes material layout within a given design space subject to certain constraints. However, the optimized geometries are complicated and are sometimes even difficult to be manufactured using additive manufacturing. This leads to the formulation of certain manufacturing constraints, making the optimized part more manufacturable. The recent development in robotic manufacturing allows for the deposition of layers in curved layers. This increased flexibility in production further expands the design space with the planning of the fabrication sequence.

1.1.1. Introduction to Additive Manufacturing



Figure 1.1: Part manufactured using AM process [43].

Additive manufacturing (AM) is a manufacturing process that produces 3-dimensional objects through layer-by-layer addition of material Fig 1.1. The terms additive manufacturing and 3D printing are used interchangeably. Although, for technical discussions, the term AM is often favored and can refer to printing steps and considerations for processing printed parts. AM involves digitally designing an object and then producing it by either deposition and bonding of material or selectively solidifying layers on top of each other to get the final desired shape. It is completely opposite to the conventional subtractive manufacturing methods, such as machining where material is removed from a stock to get the desired shape. This results in less wastage of material and unprecedented design flexibility.

AM has huge advantages that have enabled industries with faster prototyping and customization, and the production of complex geometries which were earlier not possible with traditional manufacturing techniques. Rapid Prototyping is different from AM in the sense that AM specifically aims to the manufacturing of final product rather than just prototyping. As a result, AM has found its applications in all major industries such as aerospace, automotive, healthcare, consumer products, etc.

The process of AM involves the following steps: It starts with the computer-aided design (CAD) of the object to be produced. This digital model serves as the representation of the manufacturing process. The next step is slicing the object layer by layer digitally, each slice representing the physical layer of the final object. It is basically a blueprint for the fabrication of the object. Then, the material is deposited layer-by-layer e.g. filaments, powders, or liquids based on the manufacturing technology used. A huge range of materials can be printed which includes metals, plastics, ceramics as well as composites. The ability to print different materials is largely based on the AM technology being used. After the layer is deposited, the material is either solidified or bonded together through different methods. This involves the use of light (lasers), heat, chemical reactions, or mechanical processes, all dependent on the specific AM technology being used.

There are various types of AM technologies, each with the capability of printing different materials and using different methodologies to manufacture them. Some of the most commonly used AM technologies are Fused Deposition Modeling (FDM) which involves the extrusion of a thermoplastic filament through a nozzle. The molten filament layer is deposited on top of each other and bonds together when it cools down. Stereolithography (SLA) uses a container filled with liquid photopolymer resin and a UV laser. The laser selectively solidifies the resin and as it does this the platform is lifted incrementally to build the new layer. Similar to this is Digital Light Processing (DLP) but instead of lasers it uses a digital light projector to simultaneously cure the entire layer. Next is Selective Laser Sintering (SLS) and Electron Beam Melting (EBM) which melts and fuses the powder together by using a high-powered laser in the former and an electron beam in the latter. In Binder Jetting (BJ), a liquid binding agent is deposited on top of powdered metal or sand. The binder then selectively binds the powder particles together layer-by-layer to form the object. However, in Metal Binder Jetting (MBJ), the process is followed by a sintering step to remove the binder and fuse the metal particles together. Another method that is gaining quite some importance in the field of AM is Wire Arc Additive Manufacturing (WAAM), which is a metal AM process that uses an electric arc to melt and deposit metal wire layer by layer to build the object. The advantage of this method is that it utilizes a robotic arm that can deposit layers in a curved manner which opens possibilities for improving the fabrication sequence to avoid issues such as part distortion. It offers a relatively high material deposition rate, making it suitable for the production of large-scale components. The advantages of the WAAM method will be later discussed in detail in Section 5.

Applications of AM are widespread across various industries. It allows for rapid prototyping which makes iterations faster and new concepts can be developed and tested easily. Because of the faster development cycles compared to traditional methods, highly customized and unique products can be manufactured based on customer needs. As a result, it has gained importance in the healthcare industries where patient-specific implants, prosthetics, and surgical equipment can be produced. AM enables the manufacturing of highly complex and intricate geometries which allows for lightweight and optimized structures which is the need in aerospace and automotive industries, as the ability to reduce weight while maintaining the required strength is crucial for performance and efficiency. Finally, because of the hands-on learning experience it provides due to the reduced cost of these machines making them affordable to everyone, they allow students, engineers, and researchers to explore new concepts, materials and designs faster. Although AM provides numerous advantages, it also has some downsides. AM is limited in terms of material selection as compared to traditional manufacturing processes. The parts produced may require post-processing to get the required surface finish and dimensional accuracy which can increase cost, time, and manufacturing complexity. It is good for low-volume prototyping but when it comes to large-scale production it is still inferior to traditional manufacturing methods. Also, there are some design limitations when it comes to overhangs as they need additional support structures.

In conclusion, AM is revolutionizing the way products are designed and manufactured. Its unparalleled design freedom allows for the manufacturing of complex and intricate geometries that were previously not possible. As technology advances, the issues are being thoroughly researched, and new solutions are actively implemented to mitigate the limitations mentioned above and make AM feasible for a wider application.

1.1.2. Integration of AM with Topology Optimization

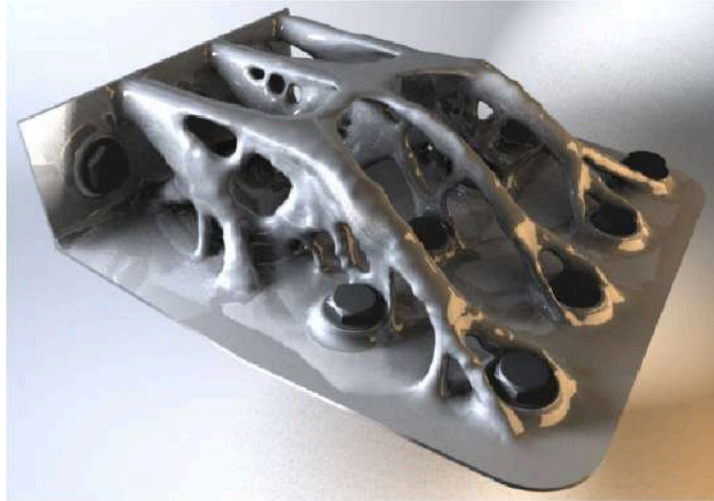


Figure 1.2: A topology-optimized structure manufactured using AM process [26].

Topology optimization (TO) is a computational design method that determines the optimal material distribution inside a given design space in order to achieve the desired performance subject to certain constraints. It identifies the optimal load paths and comes up with organic shapes by removing unnecessary materials or redistributing them. This way the structural performance is improved with reduced material usage. TO is basically a mathematical optimization technique that has some predefined steps to get to the optimized result. This includes defining an objective such as maximizing stiffness or minimizing stress. The objective function is then subjected to some constraints like volume fraction, and maximum allowable stress/ displacement. Next is to define the design domain which represents the boundaries within which material distribution can be altered. This design domain is then discretized into a finite element mesh and a structural analysis is performed using FEA. Different optimization algorithms are used such as density-based, evolutionary, and level-set-based methods, to iteratively change the material distribution within the design domain. For example in density-based TO, the sensitivities wrt the design variables determine which elements should be updated to improve the objective function. By doing this, the optimizer allocates material in regions that have a higher sensitivity as they have a larger influence on the objective function. While doing this the optimizer aims to achieve the desired objective while satisfying the given constraints. Finally, the optimization process continues iteratively until a convergence criterion is met or the desired performance objective is achieved. As TO enables the possibility of innovative designs by discovering efficient material distribution that may not be intuitively apparent. This leads to organic designs, which are sometimes not possible to produce using traditional manufacturing techniques. Thus, AM techniques become crucial in terms of the realization of those parts.

The integration of TO with AM opens a wide range of design possibilities. When coupled with AM, TO can use unique AM technologies to realize parts that would have otherwise not been possible with traditional manufacturing ways. Following are the ways in which topology-optimized design has benefits when manufactured with AM methods: The complex and intricate geometry output of the TO can be fabricated easily using AM. As mentioned earlier, TO structures have an organic shape and thus manufacturing them layer-by-layer is a lot more convenient than subtractive manufacturing. Lightweight structures can be produced as TO aims to remove unnecessary material, which can also

happen internally while maintaining structural integrity and using traditional tooling may not be sufficient but can be easily manufactured using AM methods. This way, lightweight components can be fabricated without compromising strength and performance as shown in Fig 1.2. AM allows the creation of highly integrated and consolidated parts. This is done by combining multiple components into a single monolithic structure. Examples of these are compliant mechanisms and metamaterial design. This reduces the maintenance, and cost of producing multiple components. Customization of parts can be easily done and can be tailored to specific performance needs. Lastly, AM's rapid prototyping capabilities allow engineers and designers to quickly iterate between designs, get feedback, and evaluate the designs which improve the efficiency of topology-optimized design.

1.2. Problem Statement: Overheating issues associated with AM

In Additive Manufacturing, heat is very closely related as it plays a crucial role in several aspects of the fabrication process such as material melting or softening and layer bonding. The material used in the AM processes is typically in solid form such as powder, filaments, and granules. and heat has to be applied in order to get them to a state suitable for the printing process. E.g., in the FDM process as discussed in Section 1.1.1, the thermoplastic filament material is heated to its molten or softened state. This molten material is then extruded from the extruder in a controlled manner and deposited layer upon layer. Similarly, in SLS, or EBM, heat from the laser or electron beam in the latter is used precisely to selectively melt or soften the powder bed, causing the particles to fuse together. The process is repeated layer by layer until the entire object has been printed. Also, in the AM process, the layer-by-layer approach of building the part is achieved by bonding or fusing the successive layers to create a cohesive structure. In the SLS process, heat is applied in a concentrated manner which causes the powder to reach its melting point, which leads to its fusion and solidification. As the heat is localized, the layers bond to themselves forming a dense and continuous object. The heat must be controlled accurately in order to ensure proper melting and layer bonding. Numerous factors such as scan speed, input energy, and material properties need to be calibrated in order to optimize the heat distribution which may otherwise lead to insufficient melting or overheating issues. Thus, in order to achieve the required performance from the parts printed, careful thermal management is very important.

The layer-by-layer deposition of material implies that heat basically flows from the topmost layer onto the subsequent bottom layers and into the baseplate which acts as a heat sink. The deposited heat if not evacuated to the baseplate can lead to heat accumulation or local overheating as shown by Mertens et al. [27]. It primarily refers to process temperatures outside the desired range due to different thermal conditions the material experiences locally. This results in deviation of the product from its required quality. Overheating in AM can be expressed in different ways. Overheating in AM is a thermal phenomenon that is caused by overshooting of simulation temperatures above the melting point in a study conducted by Hodge et al. [14]. In other studies conducted for in situ monitoring by Hooper et al. [15] overheating is found to be caused due to the enlarged melt pool observed in close proximity to the lower conductivity features which obstructs the heat flow. There are various factors that can cause overheating in the part. Recent studies show that process parameters such as laser power, scan speed, layer thickness, and hatch spacing can significantly affect the temperature distribution, which if not controlled can lead to overheating in parts. This leads to the dross formation in part as investigated by Charles et al. [7]. Another cause of dross formation is due to enlargement of the melt pool caused by local overheating which leads to undesired sintering of loose powder just underneath it as studied by Mertens et al. [27]. Local overheating can also be caused due to the insufficient evacuation of heat due to an increase in the height of the object. This is due to the fact that as the number of layers increases, they act as thermal barriers which cause high heating time and slow cooling rates. This phenomenon has been investigated in wire-arc additive manufacturing (WAAM) by Yang et al. [49] where they are associated with large component sizes. According to a different aspect studied by Parry et al. [30], areas that are prone to overheating produce considerable residual stresses that are likely to cause unwanted deformations and even probable structural failures. Kastsian and Reznik [18] examined the geometry of a part where local overheating resulted in severe deformations that led to a jammed recoater. The overheating issue typically affects downfacing or overhanging features because loose powder, which has a much poorer thermal conductivity than the bulk material does not allow for quick heat evacuation. When the overhang angle (defined as the angle between the part surface and the base plate) decreases,

the degree of overheating normally increases. But it has been discussed in Ranjan et al. [33], [32] that controlling overhanging features is not sufficient and the thermal response should also be considered for detecting and preventing overheating. With proper process parameter tuning and prior knowledge of overheating zones, these issues can be mitigated. Therefore, early detection of geometric elements that are prone to local overheating can help designers and machine operators assess the final design's manufacturability.

Local overheating can lead to a severe reduction in the performance of the parts. Parry et al. [30] studied that local overheating causes significant residual stresses in the parts which result in part distortion when these stresses are relieved. Also, heat accumulation can lead to a change in the microstructure which significantly impacts the physical properties as given by Leary et al. [24]. Moreover, local overheating can lead to undesired deformations in the part that could cause re-coater jamming that eventually leads to part failure as explained by Kastsian et al. [18]. Finally, poor surface quality results from the dross formation and balling which is directly associated with heat accumulation as examined by Craeghs et al. [10]. Thus, local overheating in parts can lead to a lack of dimensional accuracy, part failure, poor surface finish, and diminished mechanical properties. Thus, it is of utmost importance to address this issue during the production of parts.

1.3. State of the art

Local overheating in parts can be avoided during the fabrication stage by changing the process parameters. It can also be suppressed through some external cooling during the fabrication. A detailed explanation of these heat accumulation prevention techniques is explained in Section 2.1.1. There are a number of thermal models made to simulate the thermal behavior of the AM process. These models are useful in determining the size of the melt pool, heat flow through the part into the substrate, and generating temperature fields. These simulations help to determine the process parameters for a specific AM process. Some of the thermal models used to simulate AM are discussed in Section 2.1.2.

Controlling local overheating during the fabrication stage can be expensive due to the requirement of external means to cool the part. Also, the cooling may not be sufficient and the results may not up to the mark. Thus, it is more efficient if the local overheating is controlled during the design phase itself. Thus, topology optimization becomes useful as the designs can be optimized such that they limit the risk of local overheating. Overhangs in the design are a major reason for local overheating in parts as the medium underneath (air or loose powder) has a lower thermal conductivity than the material printed. This acts as a thermal barrier and causes heat accumulation. However, it was shown by Ranjan that even for the same degree of overhangs, the temperature distribution around them could be different depending on the neighboring features. The heat accumulation in parts can be reduced if heat is evacuated quickly. It was shown in Ranjan et al. [33] that heat loss through conduction was orders of magnitude more than convection and radiation. Heat conduction can be improved if there are higher conductivity regions in the domain. Generally, the thin connections and acute overhangs are the regions of lower conductivity which are prone to overheating. Thus, in order to limit the risk of local overheating these features should be avoided in the design.

1.4. Gap in the state of the art

1.4.1. Computational efficiency when incorporating AM thermal models with TO

The heat transfer models described in Section 2.1.2 use high-fidelity models and are computationally expensive. In topology optimization, these heat transfer calculations needed to be done in every iteration to generate the current structural layout's hotspot map. Thus, incorporating these models in the topology optimization scheme would further increase the computational burden and make the optimization intractable. Hence, it is necessary to use a computationally inexpensive model which uses certain assumptions and simplifications in performing the heat transfer calculations yet can accurately predict the hotspot map. The hotspot analysis method in [32] is able to detect and suppress geometric features that cause local overheating and outputs optimized results in a computationally efficient manner. However, as the mesh gets more refined, the time taken to solve the thermal equations at every iteration

increases significantly. Hence it is necessary to devise a method that takes less computation effort and detects and prevents heat accumulating zones in the final geometry.

1.4.2. Incorporation with various AM methods

The hotspot method by Ranjan et al. [32] is able to detect and prevent local overheating in the LPBF process where planar layers are involved. But the hotspot method cannot detect overheating if the layers are curved or some fabrication sequence is involved in the printing process. As a result, there hasn't been a method in the literature that can detect and prevent local overheating in parts where the fabrication sequence is involved. Also, every AM method has some specifics with regard to process parameters, the material used, etc. which has to be addressed every time you are doing a simulation for a different AM technique. For example, the process parameters used in the LPBF method cannot be used in the WAAM method and vice versa. Therefore, a method that can be incorporated into different AM techniques efficiently, by using the underlying physics of the process is necessary if there are computational limitations. Also, the method should be able to be incorporated into existing TO methods that involve fabrication sequences [48].

1.5. Contributions

In this section, the work done to fill in the gap in the state of the art is discussed in brief. A new approach to tackle the issue of local overheating in parts manufactured using AM is studied. At first, the need for a computationally inexpensive method to detect zones prone to local overheating is explained. Later, this method is integrated with TO to generate optimized designs that suppress the heat-accumulating features. Lastly, this method of detecting hotspots is modified to incorporate different printing strategies like curved layers and not limited to just planar layers.

1.5.1. Geometry-based method to detect and prevent local overheating

The developed approach for hotspot detection is rooted in geometry-based analysis, enabling the estimation of material distribution (local conductivity) surrounding each geometric element. This localized conductivity information serves as the foundation for generating a temperature field, effectively producing a heatmap of potential hotspots. This innovative technique offers a qualitative insight into the areas at risk of overheating within components or structures. Since the method is geometry-based and uses a mesh-independent domain, it has a computational advantage as compared to other hotspot detection methods.

To enhance design optimization, the geometry-based hotspot detection method is seamlessly integrated as a constraint within Topology Optimization (TO). By incorporating this constraint, the optimization process becomes more refined, as it actively suppresses design features that could lead to local overheating. This ensures that the resulting structural layout not only meets performance and strength requirements but also mitigates potential thermal issues, thus enhancing the overall reliability of the design.

Furthermore, the methodology's application is extended to Space-Time Topology Optimization (STTO), a dynamic optimization framework that accounts for structural evolution over time. Integrating the geometry-based hotspot detection within STTO is a pioneering step that considers both the structural layout and fabrication sequence simultaneously. By doing so, the approach not only optimizes the design for mechanical attributes but also strategically manages the risk of local overheating during the fabrication and operational phases. This holistic approach empowers engineers and designers to create components that not only excel in performance but also guarantee long-term durability and thermal stability.

1.6. Thesis structure

The current state-of-the-art is reviewed in Chapter 2, where the technology used to address the problem stated in Section 1.2 is discussed. Also, the limitations of the present methods, and how they can be rectified are addressed. This thesis is directed toward formulating a computationally efficient geometry-based hotspot detection method and using it as a constraint to limit the heat accumulation in the topology-optimized structures which can be produced using additive manufacturing. Chapter 3 is the research paper that was written during the thesis. The paper is divided into two main sections. In the first section, the geometry-based hotspot detection method is introduced, where it is compared with high-fidelity models, and its feasibility is evaluated. In the second section, modifications in the geometry-based method are done for it to be incorporated into the TO scheme. Various modifications which are done to the constraint and optimization problem to refine the final result are discussed in this chapter. In Chapter 4, a new method called space-time topology optimization will be discussed which optimizes the structural layout as well as the fabrication sequence simultaneously to improve the performance of the structures to limit overheating. The constraint will then be modified to be integrated with this method of optimization. Chapter 5 discusses the limitations of the hotspot detection method and how it can be improved in the future. Finally, a conclusion on this research is provided in Chapter 6.

2

Literature Study

2.1. State of the art

2.1.1. Heat accumulation prevention

Heat accumulation is a critical factor that influences the stability of the WAAM process in terms of the geometrical accuracy, deposition defects, microstructural evolution, material properties of as-fabricated parts, non-homogeneous material along the building direction, modification of the metal transfer mechanism, and possible workpiece structural collapse. Common ways to avoid heat accumulation in the WAAM method is by the introduction of idle times during printing to cool the workpiece down. But this reduces the productivity of the production. Another way is to use a water-cooled fixture to increase the heat sink effect of the substrate. Heat accumulation in the WAAM method can be prevented in two ways. The first is to cool the part by dissipating the heat from it through external means such as jet impingement (Montevecchi et al. [28]), natural cooling (NC), near-immersion active cooling (NIAC) (da Silva et al. [40]). Some typical thermal management approaches for WAAM reported in the recent literature and their selected highlights are given by da Silva et al. [40]. The second is to reduce the geometric features such as thin sections, funnel-like shapes, overhang structures, etc. in the part during the design phase itself which leads to heat accumulation. Recent developments in Laser Powder Bed Fusion (LPBF) machines have allowed for in situ control of input laser energy through a geometry-based algorithm with the aim of reducing overheating.

2.1.2. Thermal models for Additive Manufacturing

Various mathematical models have been created to depict heat transfer physics in the wire-arc additive manufacturing method. A 3D numerical model of Wire Arc Additive Manufacturing to simulate the material deposition and the temperature field from the operating parameters. This predictive model applied to a Cold Metal Transfer (CMT) process, takes into account electromagnetism, fluid flow, and heat transfer in all domains (wire, arc, melt pool, substrate) given by Cadiou et al. [cadiou20203d]. A 3D numerical model has been developed to investigate the fluid flow and heat transfer behaviors in multilayer deposition of plasma arc welding (PAW) based wire and arc additive manufacture (WAAM). The volume of fluid (VOF) and porosity enthalpy methods are employed to track the molten pool surface and solidification front, respectively (Bai et al. [3]). A computationally efficient, 3D, transient, heat transfer, and fluid flow model to calculate temperature and velocity fields, deposit geometry, cooling rates, and solidification parameters that affect the microstructure, properties, and defect formation (Ou et al. [29]). Also, numerical approaches for predicting temperature fields, distortions, and mechanical properties using the Finite Element (FE) software MSC Marc have been developed by Graf et al. [13]. A computationally efficient thermo-mechanical model based on a semi-analytical thermal approach incorporating Goldak heat sources is developed for the process modeling of wire arc additive manufacturing. The semi-analytical thermal model makes use of the superposition principle and thereby decomposes the temperature field into an analytical temperature field to account for the heat sources in a semi-infinite space and a complementary temperature field to account for the boundary conditions (Yang et al. [50]). These models are able to predict the thermal history in the part and a hotspot map can be generated

by further processing of the data obtained. In this way, the features which are responsible for heat accumulation can be found.

2.1.3. Introduction to density-based topology optimization

Topology optimization is a computational method that seeks to determine the optimal material distribution within a predefined design space to meet certain performance requirements. It is different from shape optimization and size optimization in the sense that topology optimization aims to find the most efficient configuration by removing unnecessary material while maintaining structural integrity. Whereas, in shape optimization, the geometry of the given design is modified while keeping constant material distribution to get performance gains. In size optimization, the shape and material distribution is constant and the only thing that varies is the dimensions of the design to achieve the desired objectives.

The general topology optimization problem is to find the most optimum material distribution that minimizes an objective function f , subject to a global volume constraint $g_0 \leq 0$, with m other constraints $g_i \leq 0$, where $i = 1, \dots, m$. The material distribution $\rho(\mathbf{x})$ is the density field that takes the value 0 (void) or 1 (solid) inside the design domain Ω . There are different approaches to solving element-based topology optimization problems such as topological derivatives, level sets, and phase fields, but the most commonly used is the density-based topology optimization by Sigmund et al. [39]. For the density approach, the topology optimization problem is solved by discretization of the design domain Ω into finite elements and the material distribution is given by N elements (or nodal) design variables. But the problem with discretization is that it makes the optimization problem difficult to solve as the design variable can only take values 0 and 1 and optimization becomes cumbersome for larger design domains (Sigmund et al. [39]). Therefore, a continuous density design approach is used which enables the use of efficient gradient-based optimization algorithms and convergence can be found quickly. The continuous topology optimization problem in its mathematical form is given as

$$\begin{aligned} \min_{\rho} \quad & f = f(\mathbf{u}(\rho), \rho) = \sum_e \int_{\Omega_e} f(\mathbf{u}(\rho_e), \rho_e) dV \\ \text{s.t.} \quad & g_0(\rho) = \int_{\Omega_e} \rho(\mathbf{x}) dV - V_0 = \sum_e v_e \rho_e - V_0 \leq 0 \\ & g_i(\mathbf{u}(\rho), \rho) \leq 0, \quad i = 1, \dots, m \\ & 0 \leq \rho_e \leq 1 \quad e = 1, \dots, N \end{aligned} \quad (2.1)$$

where \mathbf{u} is a state field (displacement for compliance minimization) that satisfies a set of linear or nonlinear state equations. The objective function can be calculated as the integral over a local function in the domain (strain energy for compliance minimization). Multiple constraint functions can be added to satisfy manufacturing needs and other real-life applications. The SIMP (Simplified Isotropic Material with Penalization) or power-law approach was introduced to reduce the complexity and improve the convergence of the solutions. A physical justification of SIMP was given by Bendsue et al. [4]. The relation between the density design variables and the material property is given by the power-law e.g.

$$E_e(\rho_e) = \rho_e^p E_0 \quad (2.2)$$

where E_0 is Young's Modulus of the solid material, and p is the penalization parameter. The function $f(\mathbf{u}(\rho), \rho)$ given in Equation 2.1 can be written in the form $b(\rho)f_0(\mathbf{u})$, where $b(\rho)$ is the density interpolation function $E_e(\rho_e)$ and $f_0(\mathbf{u})$ is a function of the field for solid material (strain energy from the density field in case of compliance minimization). The optimization problem corresponds to the "variable-thickness-sheet" for $p = 1$, which is a convex problem with a unique solution for a compliance minimization objective. For $p > 1$, the objective function penalizes the intermediate structures and outputs a 0-1 solution. If p is too high, it causes very fast convergence to local minima and if it is too low it causes too much grey scale or intermediate densities. The ballpark number that ensures 0-1 convergence is $p = 3$ for a poisson's ratio $\nu = 1/3$ as it ensures the physical realizability of elements with intermediate densities (Sigmund et al. [39]). Also, the penalization effect works when there is a constraint that limits the volume or with some filtering techniques. The mathematical formulation of

a general compliance minimization topology optimization is given as:

$$\begin{aligned}
\min_{\boldsymbol{\rho}} \quad & c(\boldsymbol{\rho}) = \mathbf{U}^T \mathbf{K} \mathbf{U} = \sum_{e=1}^N E_e(\rho_e) \mathbf{u}_e^T \mathbf{k}_0 \mathbf{u}_e \\
\text{s.t.} \quad & V(\boldsymbol{\rho})/V_0 = vf \\
& \mathbf{K} \mathbf{U} = \mathbf{F} \\
& 0 < \rho_{min} \leq \rho_e \leq 1 \quad e = 1, \dots, N
\end{aligned} \tag{2.3}$$

where c is the compliance of the structure, \mathbf{U} is the global displacement, \mathbf{F} is the force vector, \mathbf{K} is the global stiffness matrix, \mathbf{u}_e is the element displacement vector, \mathbf{k}_0 is the element stiffness matrix for an element with unit Young's Modulus, $V(\boldsymbol{\rho})$ is the material volume, V_0 is the design domain volume, and vf is the prescribed volume fraction. ρ_{min} is a vector of minimum relative densities to avoid densities becoming zero and the global stiffness matrix becoming singular.

MMA solver for optimization

The optimization problem given in Equation 2.3 can be solved using different optimization algorithms such as Sequential Linear Programming (SLP), Optimality Criteria (OC), Method of Moving Asymptotes (MMA by Svanberg [42]). The Method of Moving Asymptotes (MMA) is an optimization algorithm where in each step of the optimization, a strictly convex approximation of a subproblem is generated and evaluated. The formation of these subproblems is controlled by the term called "moving asymptotes" which not only stabilizes but also speeds up the convergence of the general process. In this thesis, the MMA optimization algorithm is used because of its computational efficiency, convergence, and flexibility with regard to handling the design variables, and multiple objective functions using appropriate weighting factors. The dual variables or the Lagrange multipliers allow for efficient handling of multiple constraints. MMA uses smooth approximation functions to solve the mesh dependence problem that frequently arises in topology optimization. By using these estimates, MMA can create material patterns that are more consistent and fluid. As a result, the designs that are produced are less susceptible to the discretization or mesh that lies beneath, which can increase the robustness and dependability of the optimization process.

Sensitivities

The MMA optimization algorithm utilizes the sensitivities to calculate the gradient of the objective and the constraint function wrt the design variables in order to provide the direction and magnitude of change required to improve the performance. The values of the asymptotes used in the MMA, which controls the magnitude of the update of the design variable at each iteration are initially set based on the initial values of the sensitivities. Thus, the calculation of the analytical sensitivities is an important step in getting the optimization result. The sensitivities of the objective function and the constraint function given in Equation 2.3 wrt the design variable ρ_e , are given by:

$$\frac{\partial c}{\partial \rho_e} = -p \rho_e^{p-1} E_0 \mathbf{u}_e^T \mathbf{k}_0 \mathbf{u}_e \tag{2.4}$$

$$\frac{\partial V}{\partial \rho_e} = 1 \tag{2.5}$$

Equation 2.5 refers to when each element has a unit volume.

Filtering

A filtering method is used to ensure that there exists a solution to the topology optimization problem and formation of a checkerboard pattern is avoided. The filtering can either be implemented on the sensitivities or the densities. The different ways to apply a filter are discussed in [38]. The sensitivity filter given Sigmund et al. [37] modifies the sensitivities given in Equation 2.4 as follows:

$$\widehat{\frac{\partial c}{\partial \rho_e}} = \frac{1}{\sum_{i \in N_e} H_{ei}} \sum_{i \in N_e} H_{ei} \rho_i \frac{\partial c}{\partial \rho_i} \quad (2.6)$$

where N_e is the set of elements i for which the center-to-center distance $\Delta(e, i)$ to element e is smaller than the filter radius r_{min} and H_{ei} is a weight factor defined as:

$$H_{ei} = \max(0, r_{min} - \Delta(e, i)) \quad (2.7)$$

A density filter given by Bruns et al. [5] transforms the original densities ρ_e referred to as the design variables to the physical densities $\tilde{\rho}_e$. It is important to note that the application of a density filter causes the original densities ρ_e to lose their physical meaning and thus the physical densities should be used as the solution to the optimization problem (Sigmund et al. [38]). The density filtering is given as:

$$\tilde{\rho}_e = \frac{1}{\sum_{i \in N_e} H_{ei}} \sum_{i \in N_e} H_{ei} \rho_i \quad (2.8)$$

Note that, whenever a density filter is applied, the sensitivities given in Equation 2.4 and Equation 2.5 need to be modified wrt the physical densities $\tilde{\rho}_e$, and a chain rule should be applied in order to achieve them. The approach will be discussed in detail in the later sections of this thesis.

2.1.4. Physics-based method for detecting and preventing local overheating

Attempts have been made in order to combine the thermal models of additive manufacturing with TO to get the desired performance. In the Ranjan et al. [33] paper, the heat transfer process for a typical (Laser Powder Bed Fusion) LPBF process has been mentioned. In this, the newly deposited layer is subjected to heat flux. The newly deposited layer conducts heat to its previously deposited layers. It is assumed that the entire deposited top layer is subjected to the incident heat flux at once and no scanning strategy is involved. The newly deposited layer conducts heat to its previously deposited layers and loses heat to the surroundings through convection and radiation. The base and previously deposited layers are assumed to be at sink temperature. The rest of the domain-environment interface is assumed to be insulated i.e. the heat flux is zero. A total of six physics-based simplifications were presented. Convection and radiation heat losses are neglected as they are negligible compared to the conduction heat losses. Also, temperature-dependent thermal properties are assumed to be at a constant temperature. Next, temporal decoupling is done where each new layer is assumed to be added at the initial temperature, and peak temperatures at the end of the heating step are used for preparing the hotspot map. This enables parallel simulation of all the layer additions providing computational gains. In this model, no data is shared between the simulations which is indicated by the horizontal broken arrows. The fifth simplification is the spatial decoupling where only a relevant sub-geometry is considered for transient thermal analysis. Lastly, steady-state analysis is done instead of a transient simulation as lower conductivity regions within a given domain influence the steady-state response, which can generate the hotspot map. Also, it is computationally faster than a transient simulation. A comparative study has been done where each simplification is compared against the reference high-fidelity thermal model using different metrics to study the influence of these simplifications in detecting the hotspot zones as shown in figures 2.1a and 2.1b.

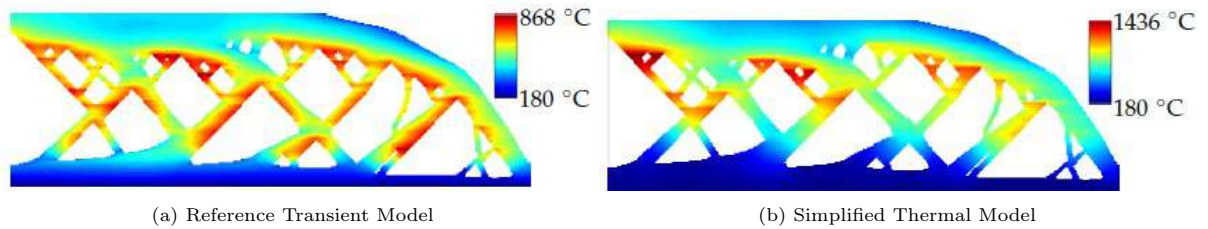


Figure 2.1: Peak temperature plots, i.e., the hotspot maps comparison between transient simulation 2.1a and simplified thermal model 2.1b from [32].

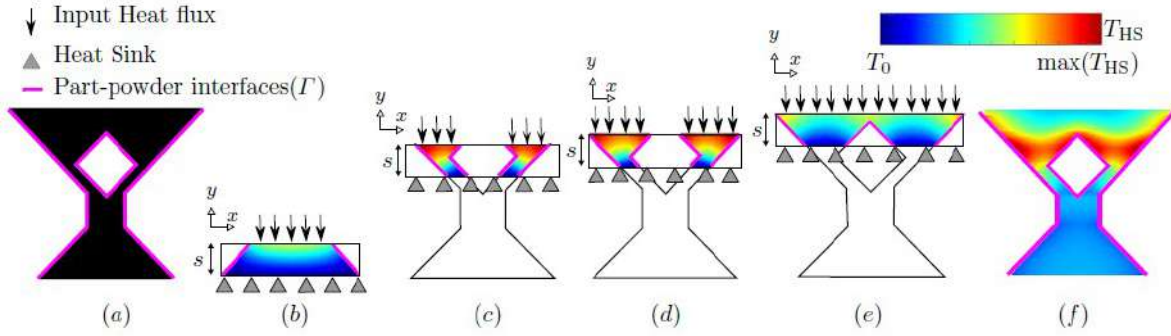


Figure 2.2: Detecting heat accumulation using slab-based analysis from [32]. a The geometry under consideration, b Subsections of the geometry with the contour levels of temperature attained with a steady-state thermal analysis. For each slab, heat flux is applied at its top, while its bottom act as a heat sink. Part-powder interfaces Γ are insulated and denoted by magenta. The maximum temperature for each material point is recorded and shown in f, which is referred to as a hotspot map T_{HS} .

The computationally inexpensive steady-state process model presented by Ranjan et al. [33] is coupled with density-based topology optimization in the Ranjan et al. [32] paper. In further sections, the slab-based hotspot detection method has been discussed. The first consideration associated with the use of steady-state thermal response is that the temperature field no longer represents a quantitative representation of the temperature transients as thermal history is lost during the temporal decoupling. Instead, it gives a qualitative representation of the temperature i.e. features that are prone to overheating. The second consideration is that steady-state analysis is only done on a local domain and not on the entire part. This is because heat transfer during AM is a transient process and only features close to the topmost layer are affected. This subset geometry close to the vicinity of the heat source is called a slab. Based on the simplifications mentioned above the 2D steady-state heat equation for each slab is given as

$$\frac{\partial^2 T}{\partial x^2} + \frac{\partial^2 T}{\partial y^2} = 0 \quad (2.9)$$

while the heat flux, insulated, and sink boundary conditions are given as

$$-k_0 \frac{\partial T}{\partial y} \Big|_{y=s} = q_0 \quad (2.10)$$

$$\frac{\partial T}{\partial x} v_x + \frac{\partial T}{\partial y} v_y = 0 \quad \text{on } \Gamma \quad (2.11)$$

$$T(x, 0) = T_0 \quad (2.12)$$

Here $T(x, y)$ is the temperature field, T_0 is the sink temperature, x and y represent spatial coordinates within the slabs with the origin located at the left bottom, v_x and v_y are the x and y components of the outward unit normal vectors on Γ , and k_0 and q_0 are thermal conductivity and input heat flux, respectively. The boundary value problem is given by Equations (2.9) to (2.12) are solved numerically using finite element analysis (FEA) and temperature field $T(x, y)$ is obtained for each slab. Figure 2.2 represents different stages of the AM process when the part is manufactured with a vertical build direction. The slabs move in the print direction and subsequently, a material point in the domain is associated with multiple slabs as the slabs may overlap each other. To generate the hotspot map, the maximum temperatures obtained for each material point for every slab it is associated with are plotted.

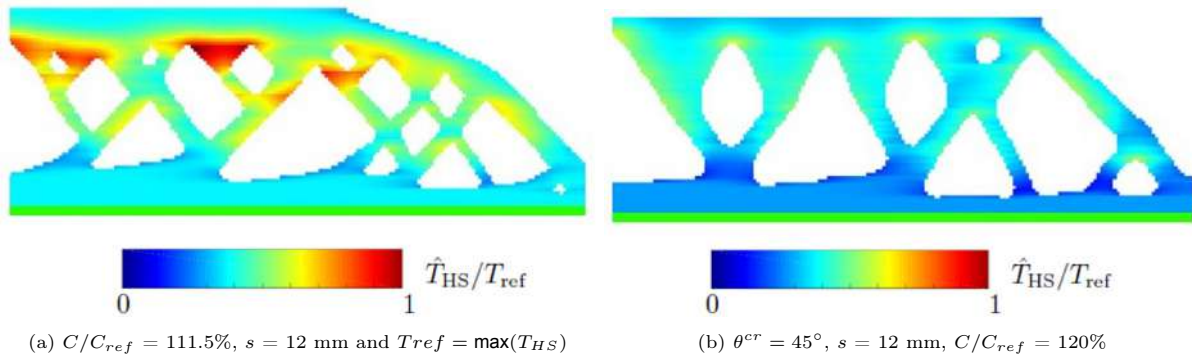


Figure 2.3: Comparison of hotspot fields for designs found by optimizing the cantilever problem using 2.3a AM filter-based TO [20], 2.3b hotspot-based robust TO [32].

A comparison was made between the Langelaar et al. [20] geometry-based overhang control where the geometry was subjected to a hotspot analysis and compared with the design obtained using hotspot constraint having a similar set of parameters used as shown in figures 2.3a and 2.3b. Both fields are normalized to a common scale for comparison. Fig 2.3a. It can be seen that a geometry-based TO for overhang control is insufficient for controlling local overheating and redistribution of material to avoid funnel-like structures is important to avoid the hotspots as seen in Fig 2.3b.

3

A geometric approach for controlling local overheating in topology optimization for additive manufacturing

¹This chapter is intended as a manuscript for journal submission.

Additive manufacturing (AM) has revolutionized part manufacturing, offering unprecedented design freedom and the ability to fabricate intricate structures. Computational design methods like topology optimization (TO) effectively capitalize on AM's design freedom. However, manufacturability constraints must be considered to ensure reliable manufacturing. A significant constraint is local overheating, prevalent in metal additive manufacturing, leading to defects, part distortion, and diminished mechanical properties. While overhangs are commonly associated with overheating, they are not the only geometric features prone to overheating. This thesis addresses the overheating issue in topology optimization by a novel geometric approach. Specifically, we propose to estimate the local conductivity around each element by evaluating the material distribution in its vicinity. This is then used to generate a pseudo temperature field (i.e., hotspot map) to assess overheating risks. Formulated as a constraint in topology optimization, our approach creates optimized structural layouts free of local overheating during additive manufacturing. Compared with existing overheating prevention methods, the geometry-based constraint demonstrates significant computational advantages. Transient thermal AM simulations were conducted on the final designs obtained using the physics-based method from the literature and the novel geometry-based overheating prevention method. The numerical results have shown that the proposed geometric approach is efficient and effective in controlling local overheating in topology optimization for metal additive manufacturing.

3.1. Introduction

Additive manufacturing (AM) has gained a lot of importance in the manufacturing industries. Its unprecedented advantage of producing highly intricate geometries distinguishes it from conventional production techniques such as milling, forging, or casting. The material usage for the same part size is less as compared to other production techniques as it grows three-dimensional objects through layer-by-layer material addition that bonds together. The advantages of additive manufacturing are best utilized in combination with topology optimization (TO). Topology optimization is a method that optimizes material layout within a given design space subject to certain constraints. However, the optimized geometries are complicated and are sometimes even difficult to manufacture even using additive manufacturing. This leads to the formulation of certain manufacturing constraints, making the optimized part more manufacturable. As the parts that are built using AM processes are getting more intricate and the requirement of high dimensional accuracy is a must, importance is given to other manufacturing constraints as well. One such issue is local overheating or heat accumulation in the parts during the fabrication which causes detrimental effects on mechanical properties as well as dimensional accuracy. Overheating is seen in both polymer and metal AM fabrication, but the effect is more prominent in metals due to the higher production temperatures involved.

The local overheating of the components causes a multitude of problems that lead to a decrease in performance. Local overheating causes significant residual stresses in the parts which result in part distortion when these stresses are relieved as given by Parry et al. [30]. Also, poor surface quality results from the dross formation and balling which is directly associated with heat accumulation as studied by Craeghs et al. [10]. Moreover, local overheating can lead to undesired deformations in the part that could cause re-coater jamming that eventually leads to part failure as explained by Kastsian et al. [18]. Finally, heat accumulation can lead to a change in the micro-structure which significantly impacts the physical properties given by Leary et al. [24].

In most of the AM techniques whether LPBF or filament deposition, heat is used to melt or soften the material in a layer-by-layer fashion and fuse them together to form a solid part. In doing so, heat flows from the topmost layer which is currently deposited, through the previous layers and into the baseplate. Heat accumulation occurs whenever this incident thermal energy does not have a conductive path to go to the baseplate. The regions that obstruct the heat flow cause the enlargement of melt pools which results in local overheating as studied by in situ monitoring by Craeghs et al. [11].

Overheating can be classified into three main categories. The first is the process parameters associated with the manufacturing process such as laser power, scan velocity, and scan pattern. The local thermal history is greatly influenced by the energy density which is controlled by the process parameters. The second category is the thermal properties of the printing material as material with higher thermal diffusivity and thermal conductivity will allow for efficient heat evacuation. And the last category depends on the part design. Local overheating is caused in regions where the features do not facilitate faster heat evacuation. In this paper, the main focus is put on the third category i.e. heat accumulation due to part layout. This means that the first two categories i.e. process parameters and material properties are kept constant and only the overheating effects due to part design are analyzed.

One of the main reasons that results in overheating in parts is the overhanging features. The lack of material underneath the down-facing features causes inefficient conduction of heat to the baseplate. Developments have been made in the past to counter these limitations by controlling the overhang angles by Liu et al. [17], and Langelaar et al. [20]. However, it has been shown by Adam et al. [1] and Ranjan et al. [33] that even with the same degree of overhang angles, the overhangs showed a different thermal behavior based on the heat evacuation capacity of the features in the vicinity. Thus, using a single overhang angle may not be sufficient in preventing overheating and might be too conservative. As the features in the vicinity of the overhang may allow for heat conduction to the baseplate, a more acute overhang angle may be allowed making the design less restrictive. Topology optimization (TO) allows for the exploration of the designs for AM techniques. Attempts have been made in the past to integrate manufacturing constraints with TO but it's mainly for geometrical overhangs. A TO strategy that could prevent overheating by explicitly accounting for the thermal evolution throughout the AM process would have significant advantages over currently used geometric techniques. Zhou et al. [52]

successfully integrated a transient thermal AM simulation with the density-based TO. However, the computational time taken was very high. Ranjan et al. [33] provided a simplified thermal model for detecting hotspots and it was later used by Ranjan et al. [32] to suppress these features and deliver optimized results within a practical time frame. The method used was typically for the LPBF process where layer-by-layer deposition is done. However, a computationally efficient method that can easily be implemented in any AM process where the fabrication sequence is also specified is still lacking.

In this paper, a geometry-based method for detecting overheating zones in parts is introduced. The approach called the 'Conductivity estimation method' primarily captures the material distribution around a given element and outputs a local conductivity for that element. It is intended to replicate the actual physics of thermal conduction but in a geometric manner and presents a qualitative estimate of the temperature obtained during the manufacturing process from the local conductivity information obtained earlier. The method is compared against other existing AM overheating control methods to show its effectiveness. Furthermore, this conductivity estimation method is used as a constraint in the robust TO problem given by Wang et al. [47] that could create a design that allows for efficient heat conduction to the baseplate. The main idea is that the features in a part produced using AM should have sufficient material in the vicinity to allow for maximum heat conduction and thus minimize the risk of overheating.

3.2. Geometry-based hotspot detection method

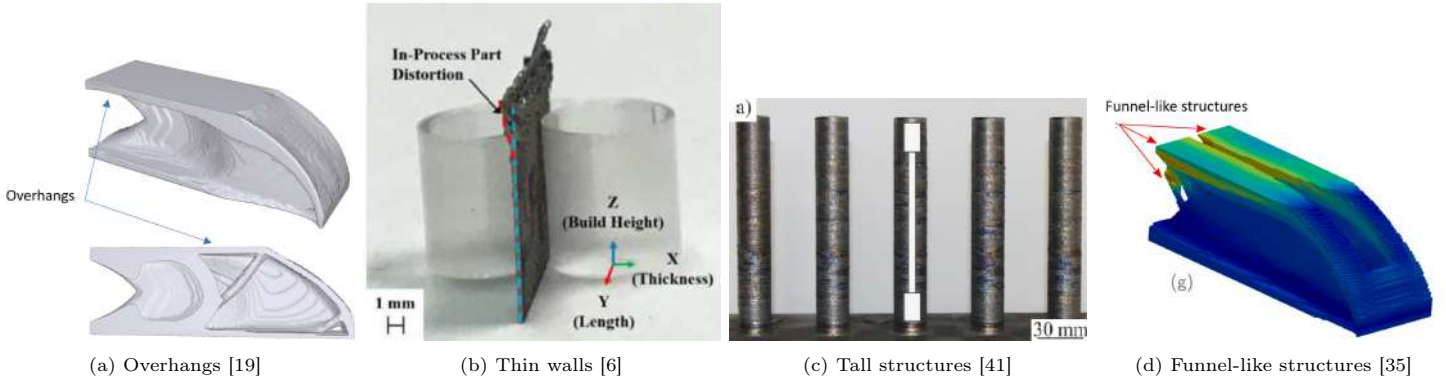


Figure 3.1: Features that cause local overheating in AM process

In this paper, we are going to use the part design factor to control the local overheating in the geometry. The two phenomena i.e. local overheating and progressive heat accumulation during manufacturing are closely related. Elevated temperatures brought on by local overheating aid in the progressive buildup of heat in the succeeding layers, and conversely accumulated heat will exacerbate local overheating. Overhangs are one of the major reasons that contribute to heat accumulation in parts, as the layer that is deposited has very little to no material underneath it to allow for sufficient heat conduction Figure 3.1a. This is because the conductivity of air or loose powder is less than that of the solidified material. The part-powder interface basically acts as an insulator and traps the heat. This obstruction in heat flow results in high temperatures near the overhangs. But there are other features that also contribute to local overheating. Thin sections as shown in Figure 3.1b that have very little material in the vicinity can cause obstruction to the heat flow and cause enlargement of the melt pool in that region causing overheating as studied by Craeghs et al. [11]. Therefore, it is necessary to have a minimum feature size throughout the part geometry to ensure effective heat evacuation. Also for tall structures as shown in Figure 3.1c, overheating increases as more layers are deposited that act as thermal barriers causing prolonged heat accumulation and slower cooling rates. Another feature that causes overheating in parts is the funnel-like structures as shown in Figure 3.1d that are formed in the parts that act like a thermal bottleneck to the heat flow as studied by Ranjan et al. [32], [35]. Thus, these features discussed are the major cause of local overheating and should be avoided to minimize the overheating risks in parts.

The thermal model presented by Ranjan et al. [33] uses certain simplifications from the transient

AM simulation such as temporal and spatial decoupling, neglecting convective and radiative heat losses, constant material properties, and lastly a steady-state thermal simulation to quickly detect the approximate temperatures generated in the part during fabrication. A similar idea is used in this paper but instead of the physics-based model, we use a geometry-based model to capture the features in a smaller region close to the moving heat source. As the effect of heat conduction saturates after a certain length called the mean conduction length which is discussed in Section 3.2.3, only the elements which are within this bound can be used to get an estimate of the local conductivity in the region. Since the temperature generated is inversely proportional to the conductivity, we can use this local conductivity information to generate a hotspot map from the temperatures obtained. This hotspot map is a qualitative representation of the maximum temperature which could occur during the manufacturing process. Since the method is purely geometrical, it gives a huge computational advantage compared to the existing physics-based method, where thermal simulation has to be done over the entire domain.

3.2.1. Conductivity estimation

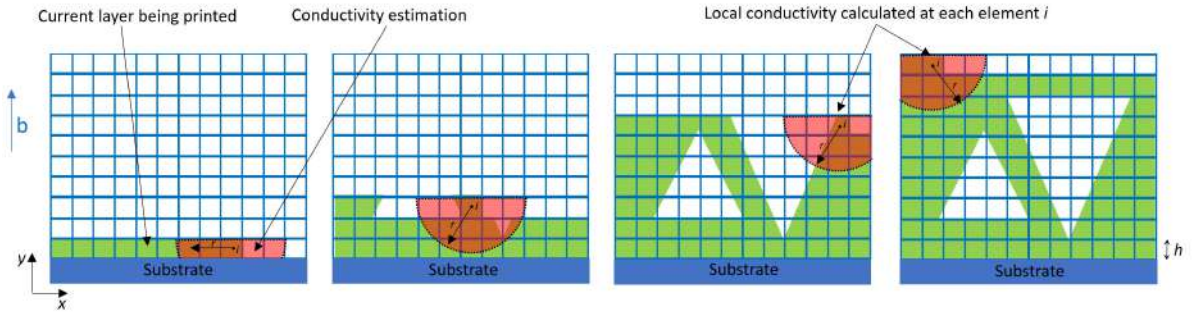


Figure 3.2: Illustration of the conductivity estimation over a part build using AM. The design domain is discretized into regular 4-noded rectangular elements with a substrate at the bottom. The build direction b is indicated by a blue arrow. The layer-by-layer deposition of the material is shown in green which forms the part. The conductivity estimation as shown in red captures elements that are within the thermal interaction length r . The layer thickness is given by h .

Local overheating in parts is a direct result of enlarged melt pools observed in the vicinity of lower conductivity regions (Hooper [15] and Kruth [10]). Certain features like overhangs, and thin walls usually have a lower material distribution around them that aid in lower conductivity and accumulation of heat. If heat is quickly evacuated, the accumulation of heat in these features can be reduced. Heat loss by conduction was demonstrated to be orders of magnitude greater than heat loss through convection and radiation in Ranjan et al. [33]. If the geometry has areas with higher conductivity, heat conduction can be improved. Hence it is important to understand the material distribution of a part as it influences the thermal behavior during the AM process. To estimate the distribution of material underneath the newly deposited layer which are directly under the influence of the heat source, a method has been developed called conductivity estimation. In the AM process, the heat from the source flows through the material in all directions up to a certain length called the thermal interaction length r given in Section 3.2.3. This results in a thermal domain that is close to a hemisphere as only the layers that are printed are considered. The material that is within this hemispherical domain will influence the heat conduction. For our 2D simulations, this becomes a semicircular domain. As shown in Figure 3.2, the design domain is discretized into regular four-noded rectangular elements. The green region is the solid geometry whose local conductivity in each of the elements is to be found. The solid green region is assigned a density value of 1 and the voids have a density value of 0. The conductivity estimation considers the densities of the elements ρ_j around the centroid of a given element i w.r.t the total no. of elements N that are there inside the domain as shown in Figure 3.2. The conductivity estimation domain moves through each and every element across the layer and along the build direction to capture the features in the design domain. Then based on the ratio between their density and the total number of elements in the domain, it gives an estimate of the local conductivity which lies in the range $[0,1]$. The local conductivity of an element i is given as

$$\kappa_i = \sum_{j \in S_i}^N \frac{\rho_j}{N(S_i)} \quad (3.1)$$

where, S_i represents the set of elements in the vicinity of element i defined as $|x_i - x_j| < r$ and $y_j \leq y_i$

Finally, the temperature field $\tilde{\mathbf{T}}$ is obtained by subtracting the local conductivity and multiplying it with the density field given by

$$\tilde{\mathbf{T}} = (\mathbf{I} - \boldsymbol{\kappa})\boldsymbol{\rho} \quad (3.2)$$

The lower the local conductivity of the element, the higher the temperature. Thus, if the local geometry has too many hollow regions or overhangs, the conductivity in that region is poor and the conductivity filter will be able to detect the hotspot zones.

3.2.2. Using penalization to capture actual behavior of heat conduction in AM

The conductivity estimation is combined with a radial weight function in order to illustrate the effect of neighboring elements as their distance changes from the central element whose local conductivity is being calculated. The elements which are far away from the central element of the filter have less contribution in conducting heat and hence they are penalized with a low weight. Conversely, the elements closer to the central element have a higher contribution to heat conduction, and hence their influence is upsurged. Also, an angular weight function is used to penalize the elements that are adjacent to the element under consideration to suppress the side flow effect of heat. This is done because the elements that are on the same layer as the element whose local conductivity is found, do not contribute much to heat evacuation and the heat conduction becomes more pronounced as we go along the build direction.

$$\kappa_i = \frac{\sum_{j \in S_i}^N \rho_j w_j}{\sum_{j \in S_i}^N w_j} \quad (3.3)$$

where $w = wr \times wa$, wr is the distance weight function and wa is the angular weight function.

The distance weight function wr is given by,

$$wr_j = r - \sqrt{(x_i - x_j)^2 + (y_i - y_j)^2} \quad (3.4)$$

The angular weight function wa is given by,

$$wa_j = \frac{1}{\psi} \left(\arctan \left(\frac{y_i - y_j}{x_i - x_j} \right) \right) \quad (3.5)$$

here, r is the thermal interaction length or radius of the semicircle and ψ is the scaling factor.

As shown in Figure 3.3, wa is higher for elements that are closer to the central element and decreases linearly as it goes towards the boundary of the filter. The wa is higher for elements that are furthest away in the build direction (for $\theta = 90^\circ$) and decreases linearly as the angle of the elements decreases and becomes 0, as shown in Figure 3.3. With these weight functions, the neighboring elements are penalized linearly and approximately capture the actual thermal behavior of heat conduction. However, the weight functions used can be made nonlinear to control how fast or slow the effect of neighboring elements changes as given in Appendix A.1.

3.2.3. Determination of the conductivity estimation filter radius

In the paper Ranjan et al. [33], the impact of the simplifications mentioned in Section 3.2 in detecting overheating was studied. Here, the relation between the peak temperature and the domain size of conduction and heat flow in a one-dimensional transient simulation was given. This analysis found that there exists a saturation domain length and peak temperatures remain unaffected if we analyze elements beyond this domain size. Therefore, the domain beyond this length can be discarded and no effect will be seen in the peak temperatures. This saturation length is called the mean conduction

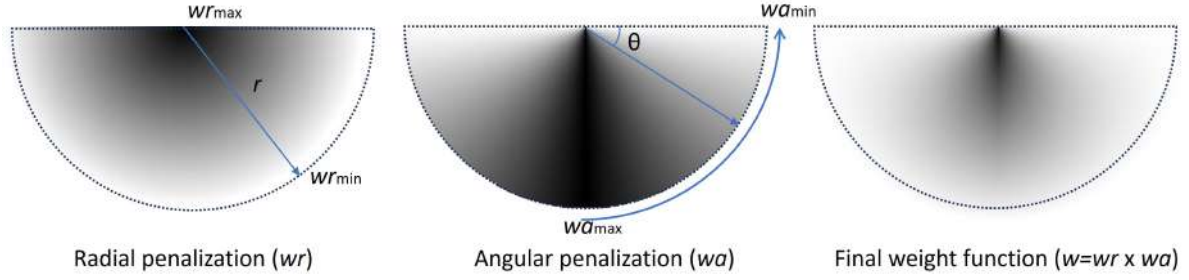


Figure 3.3: Illustration of the weights used in the conductivity estimation filter

length or thermal interaction length s and it depends upon the thermal diffusivity α and heating time t_h of the layer. A detailed explanation of the selection of α and t_h values is given in Ranjan et al. [33]. The heat evacuation is during the cooling stage of the AM process, but only the material that is within this thermal interaction length will help in the heat conduction. Thus, the same saturation length can be used to find the conductivity estimation filter radius. Therefore, only the material which is inside this saturation length domain will be considered for the calculation of local conductivity. Even though there may be less material for conduction outside the saturation length, they won't increase the peak temperatures for that given element, since features in the vicinity of the topmost layer are relevant for the heat flow in the transient AM process. Hence, the mean conduction length r is given by

$$r = \sqrt{\alpha t_h} \quad (3.6)$$

Here, α and t_h is given as

$$\alpha = \frac{k}{\rho C_p} \quad (3.7)$$

where k is the thermal conductivity, ρ is the density and C_p is the specific heat of the material.

$$t_h = \frac{A}{hv} \quad (3.8)$$

where A is the layer area, h is the hatch spacing and v is the scan velocity.

3.2.4. Application of conductivity estimation filter in detecting overheating zones in geometries

The working of the conductivity estimation method is illustrated using the 2D geometry shown in Figure 3.4. It is similar to the geometry used in [32] which was used to test the hotspot detection method. This has been done so that a comparison could be made about the effectiveness of the conductivity estimation method in detecting hotspot zones. The geometry is made in such a way that it encapsulates all the features that are responsible for generating local overheating such as overhangs, thin sections, and funnel-like structures (Leary et al. [24], Craeghs et al. [10], Wang et al. [45], Ranjan et al. [32]). In order to observe the variation in the thermal response due to the material distribution in the vicinity of the topmost layer, all the overhangs are kept at an angle of ($\theta = 45^\circ$). The conductivity filter radius r is calculated based on the mean conduction length as given in Section 3.2.3 which depends upon the penetration depth of heat for this geometry size. The filter scans the entire geometry element by element in such a way that it simulates the printing first along the layer (x axis) and then along the build direction (y axis). The conductivity estimation method, however, can be added to the entire geometry without concern for the scan strategy or build direction because it is merely a filter that passes through each element, and the entire geometry is already provided. The semicircular shape of the filter ensures that only the features that are already deposited are captured inside the filter and thus simulate the build direction. The angular penalization w_2 and radial penalization w_1 given in Figure 3.3 penalize the effect of the elements which are adjacent and away from the element respectively whose local conductivity is been evaluated. This way only the elements which are closer to the central element and along the build direction are taken into consideration for the evaluation of the local conductivity. Another advantage of using penalization weights is that sometimes the filter

may capture nearby features that are not connected to the central element and may not help in heat conduction but these weights nullify their effect. This way the conductivity estimation filter doesn't overestimate the conductivity and outputs the appropriate temperature as can be seen from Figure 3.4f.

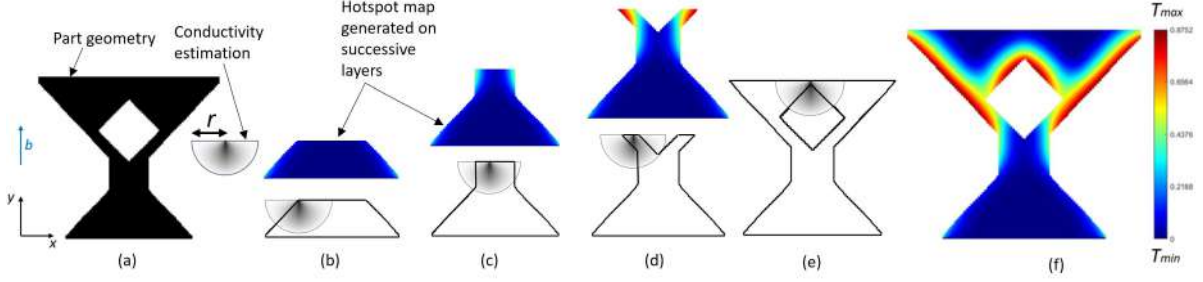


Figure 3.4: Illustration of the working of the conductivity estimation in detecting heat accumulation zones. The build direction is given by b . The domain size r is calculated from the thermal interaction length for this part geometry. 3.4a shows the geometry used, 3.4f shows the final hotspot map. 3.4b,c,d,e shows the layer-by-layer movement of the conductivity estimation filter and generating local temperature data.

The local conductivity of the entire geometry κ is calculated using Equation 3.3 and the hotspot map of the temperature field $\hat{\mathbf{T}}$ is generated using Equation 3.2 is shown in Figure 3.4f. T_{max} and T_{min} indicate the maximum and minimum normalized temperature in the hotspot map. Figure 3.4b-e shows the intermediate stages of the build during the AM process on the left and the respective hotspot map on the right. As can be seen in Figure 3.4b,c, since there are a large number of elements that contribute to heat conduction, the heat evacuation is adequate, and overheating risks are low as observed in their corresponding hotspot map. As we reach near the thin feature section which is also an overhang in Figure 3.4d, the number of elements to conduct heat as captured by the conductivity estimation filter decreases and thus the hotspot map shows a rise in temperature. Similar is the case when we encounter the overhang junction section in Figure 3.4e. Since the side flow of heat is penalized, it shows a relatively high temperature in that region as very less material is available underneath that point for proper heat conduction. This analysis is in accordance with the experimental findings in Adam et al. [1], Van et al. [44], and Patel et al. [31]. Note that even though all overhangs have the same degree of overhang (45°), the temperature field is different throughout based on the distribution of the materials in the vicinity of the topmost layer being analyzed. Thus, this method proves to be effective in detecting hotspots in geometry and is computationally inexpensive. A study on the effect of variation of conductivity estimation filter radius is given in Appendix A.1.

3.2.5. Comparison of conductivity estimation with current hotspot detection approaches

To test the feasibility of the conductivity estimation method it is compared with the geometry obtained using the slab analysis hotspot constraint from the paper Ranjan et al. [32]. A transient simulation has also been done in this geometry obtained as a post-optimization step that acts as a reference model for both the hotspot detection method from Ranjan et al. [32] and the conductivity estimation method which is given in this paper. Since both the slab analysis hotspot detection and conductivity estimation method give a pseudo temperature field which is then plotted as a hotspot map, the temperature field is normalized for both methods by dividing with their respective maximum temperature in both fields i.e., $\hat{\mathbf{T}} = \mathbf{T}/\max\mathbf{T}$, where $\hat{\mathbf{T}}$ represents the normalized temperature field. Also, the transient simulation hotspot map is divided by its maximum temperature so that everything is on the same scale. Details of the approach and parameters of the transient simulation can be found in [33]. Let's call the normalized transient simulation temperature field obtained as $\hat{\mathbf{T}}_{ref}$. The normalized temperature field for the slab analysis method and conductivity estimation method will be called $\hat{\mathbf{T}}_{slab}$ and $\hat{\mathbf{T}}_{cest}$ respectively. Since all three temperature fields are normalized, the error in the maximum temperature recorded cannot be obtained. Therefore, a different comparison metric is used called the Jaccard index to get the spatial similarity between the two temperature fields $\hat{\mathbf{T}}_{slab}$, $\hat{\mathbf{T}}_{cest}$ w.r.t the transient reference temperature field $\hat{\mathbf{T}}_{ref}$. The Jaccard index is known as the ratio of intersection and union between the two images and is a regularly used metric in the field of image recognition for assessing the similarity between two images

from Jaccard et al. [16]. It is given as:

$$J = \frac{\sum_{i=1}^n \min(\hat{T}_1^{(i)}, \hat{T}_2^{(i)})}{\sum_{i=1}^n \max(\hat{T}_1^{(i)}, \hat{T}_2^{(i)})} \times 100\% \quad (3.9)$$

where $\hat{T}_1^{(i)}, \hat{T}_2^{(i)}$ indicates the normalized temperatures for the node i for the two fields being compared, n is the total number of elements in the geometry. A high value of the Jaccard index indicates that the spatial distribution of the temperature field is very similar.

Table 3.1: Jaccard index for different analysis

JI	Conductivity estimation	Slab analysis	Transient analysis
Conductivity estimation	-	$(\hat{T}_1, \hat{T}_2) = (\hat{T}_{slab}, \hat{T}_{cest})$ =40.2%	$(\hat{T}_1, \hat{T}_2) = (\hat{T}_{ref}, \hat{T}_{cest})$ =32.22%
Slab analysis	-	-	$(\hat{T}_1, \hat{T}_2) = (\hat{T}_{ref}, \hat{T}_{slab})$ =64.67%

Figures 3.5a, 3.5c and 3.5e show the normalized hotspot map for the transient, slab, and conductivity analyses, respectively. It is apparent that the spatial distribution of the temperature field in conductivity estimation analysis is very different from that in transient and simplified slab analysis. This difference can also be calculated from the Jaccard index value given in Table 3.1, where there is only a 32.22% match in the spatial distribution of the temperature field value between the conductivity estimation and slab analysis methods, as compared to a match of 64.47% between the slab analysis and transient analysis. Also, there is only a 40.2% match between conductivity estimation and slab analysis hotspot maps. This is because the feature size is larger than the conductivity filter radius size. Since the filter radius is close to completely filled, it detects a high local conductivity for that element and doesn't show a very high temperature in that region.

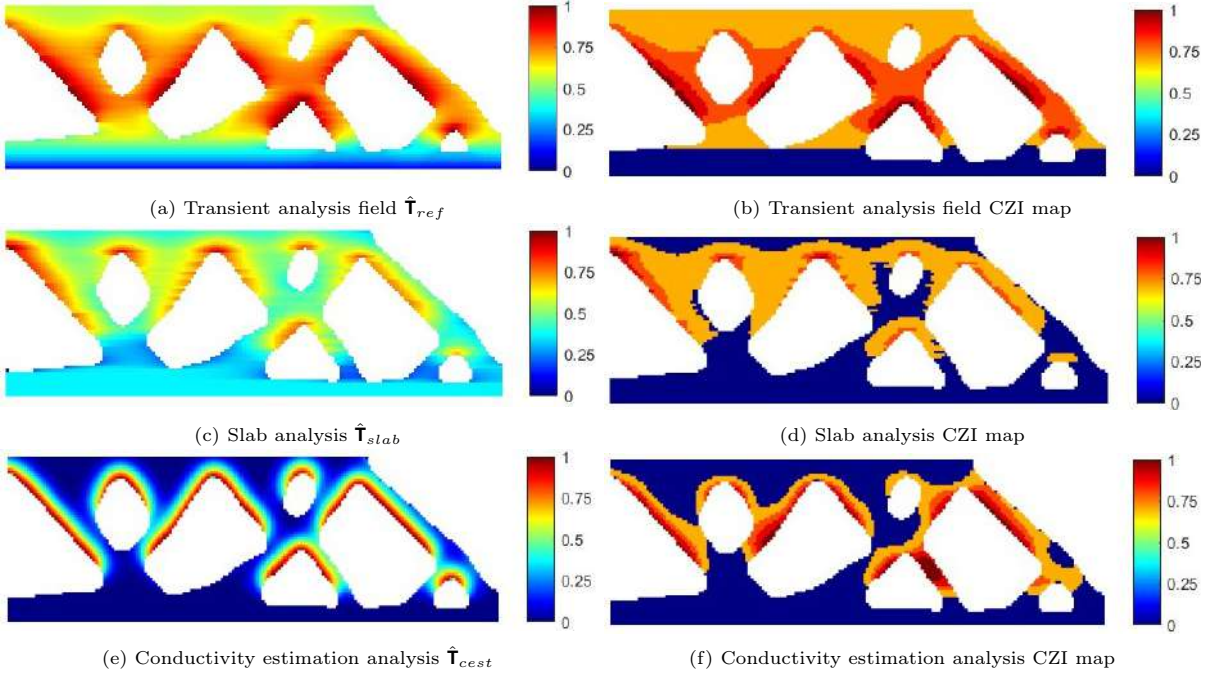


Figure 3.5: Normalized temperature field, i.e., the hotspot maps for different analyses are presented in Figures 3.5a, 3.5c and 3.5e and the corresponding CZI maps are presented in Figures 3.5b, 3.5d and 3.5f. Sub-captions are provided to specify the respective analysis being done.

However, in our study, our primary focus lies not on the entire temperature distribution, but rather on identifying the critical temperature zones within the geometry. By honing in on these crucial areas,

we aim to gain a deeper understanding of the potential overheating risks and effectively address them. Therefore, we introduce another comparison metric called a critical zone identification (CZI) map to locate the critically affected zones for overheating. It basically suppresses the cooler zone below a threshold and highlights the critical zones at certain levels. It is described as the normalized temperature field's contour map with four contour levels, which were here selected at 50%, 70%, 80%, and 90% of the field's maximum temperature. A similar approach was used in [33] to identify the critical temperature zones in each of the simplifications to the thermal AM model. Figure Figures 3.5b, 3.5d and 3.5f shows the CZI maps for the transient, slab, and conductivity analyses, respectively. It can be clearly seen that the critical heating zones are highlighted in the contours. The CZI map of the conductivity estimation analysis Figure 3.5f is very similar to the transient simulation analysis 3.5b which shows that it is able to identify the critical overheating zones correctly. Thus, this method proves to be beneficial when detecting local overheating or heat accumulation zones in the geometry. Another application of this conductivity estimation method in detecting overheating zones on a geometry with different feature sizes is given in Appendix A.2.

3.3. Integration with Topology Optimization (TO)

The conductivity estimation method presented in Section 3.2 gives a qualitative estimate of the temperature field from the derived local conductivity of the geometry. Note that, the temperatures do not represent the actual temperature that will occur during the transient AM process, nor does the conductivity signifies the actual thermal conductivity. It is a representation of the overheating risks associated with having certain design features in the geometry which will have a poor conductivity due to lack of material beneath them to conduct heat, thereby lowering the efficiency of heat evacuation. In TO, in order to limit the risk of local overheating in the designs obtained there should be some constraint that could easily detect those features and restrict them from appearing in the final design. The conductivity estimation method proved to be efficient in detecting heat accumulation zones when compared with a transient thermal AM simulation as given in Section 3.2.5. Thus, the conductivity estimation method can be used as a constraint in the TO formulation as it can avoid the heat accumulating features such as thin features, overhangs, and funnel-like structures, that will result in lower thermal conductivity from the conductivity estimation filter and therefore, a higher output temperature. As a result, the final geometry is expected to have design features that will allow for efficient heat evacuation to the baseplate and thus reduce the risk of local overheating.

3.3.1. Formulation of conductivity estimation method as a constraint

The conductivity estimation filter is used as a constraint (described as hotspot constraint hereafter) to limit the maximum temperature generated in the geometry below a critical value during the additive manufacturing process. The conductivity estimation method used for the hotspot constraint will evaluate the local conductivity of each element based on the features around them. This local conductivity will be used to calculate the temperature field (hotspot map). The constraint is to limit the maximum temperature value occurring in each of these elements below a critical value in order to prevent the risk of overheating. In order to limit the maximum temperature in each of these elements, the constraint will drive the optimizer to add sufficient material everywhere, conforming with the global volume constraint, and thus the minimum local conductivity everywhere will be above a certain value in the base design. As discussed in Section 3.2.2, the local conductivity $\kappa_e \in [0,1]$ of each element is found using Eqn 3.10. The hotspot map showing a pseudo temperature $T_e \in [0,1]$ can be calculated using the Eqn 3.11 which states lower the local conductivity higher the temperature of that element and vice-versa.

$$\kappa_e = \frac{\sum_{j \in N_e} \rho_j w_j}{\sum_{j \in N_e} w_j} \quad (3.10)$$

$$T_e = 1 - \kappa_e \quad (3.11)$$

where, N_e represents the set of elements in the vicinity of element e defined as $|x_e - x_j| < r$ and $y_j \leq y_e$

The pseudo temperature T_e of the element should be lower than a critical value called the critical

temperature value T_{cr} to control the local overheating and is given by:

$$T_e \leq T_{cr} \quad e = 1, 2, \dots, n \quad (3.12)$$

where e is the no. of elements which means having n constraints. But having n constraint which is also equal to the no. of design variables is very large and thus the sensitivity analysis is going to be computationally expensive. In order to improve the computational efficiency, a single maximum temperature $\tilde{\mathbf{T}}^\Omega$ given by the conductivity estimation filter is put on the entire domain Ω , and this global maximum temperature should be less than the critical value T_{cr} . Thus, the hotspot constraint can be formulated by,

$$\max(\tilde{\mathbf{T}}^\Omega) \leq T_{cr} \quad (3.13)$$

The max operator is non-differentiable, whereas a smooth operation is required for calculating the sensitivities needed in TO. Therefore, a P-mean aggregation scheme is used for specifying the constraint which is a smooth continuous function used to find the maximum temperature over the entire design domain.

$$\left[\frac{1}{n} \sum_e (\tilde{T}_e^\Omega)^P \right]^{1/P} \leq T_{cr} \quad (3.14)$$

here, \tilde{T}_e^Ω is the e -th member of the array $\tilde{\mathbf{T}}^\Omega$, P is the exponent used for defining P-mean, and n is the total number of elements. Thus from Eqn 3.14 and Eqn 3.11 we get the hotspot constraint g as:

$$g = \frac{1}{T_{cr}} \left[\frac{1}{n} \sum_e ((1 - \kappa_e))^P \right]^{1/P} - 1 \leq 0 \quad (3.15)$$

However, this P-mean tends to underestimate the maximum temperature. This error can be reduced by increasing the P value. As $P \rightarrow \infty$ the P-mean approaches the maximum value but loses the smoothness and for $P \rightarrow 1$ the value approaches an average value. But in our case, a correct estimation of the true maximum is required otherwise the overshoot or undershoot beyond T_{cr} would result in incorrect constraint value which will eventually affect the designs obtained as they will be far from optimum. Therefore, the maximum discovered by the P-mean is corrected by scaling it with the genuine maximum according to an adaptive scheme proposed by Le et al. [23]. This indicates that the hotspot constraint includes a scaling factor α given by:

$$g = \frac{\alpha}{T_{cr}} \left[\frac{1}{n} \sum_e ((1 - \kappa_e))^P \right]^{1/P} - 1 \leq 0 \quad (3.16)$$

where α is defined as the ratio between the true maximum temperature obtained from the design domain and the P-mean maximum from previous iterations given by:

$$\alpha_{(I)} = \left[\frac{\max(\tilde{\mathbf{T}}^\Omega)}{\left[\frac{1}{n} \sum_e (\tilde{T}_e^\Omega)^P \right]^{1/P}} \right]_{(I-1)} \quad (3.17)$$

where I is the current iteration number. Note that, since α changes in a discontinuous manner, the adaptive scheme may cause convergence issues. Therefore, the scaling factor is changed every 25 iterations as a continuation approach which solves this issue of non-convergence. The value of P is found to be 25 which gives a decent accuracy in determining the smooth maximum and has good convergence over the design iterations. A similar approach for scaling the P-mean maximum to the true maximum is used by Ranjan et al. [32].

3.3.2. Topology optimization problem

The 88-line MATLAB code given by Andrea et al. [2] was used to incorporate the conductivity estimation hotspot constraint. The optimization algorithm used is the method of moving asymptotes (MMA) by Svanberg[42] where all the default parameters of MMA are used. The study of the effects of modifying the MMA parameters in the design obtained is beyond the scope of this paper. The main objective of this paper is to investigate the effects of having a conductivity estimation-based hotspot constraint in

the design and thus, a linear elastic compliance minimization objective with a global volume constraint is used. The SIMP interpolation model by Bendsue et al. [4] is used which is the most common material model in the density-based TO. Thus, the hotspot constraint presented in Section 3.3.1 is used on top of the compliance minimization problem to suppress the features resulting in local overheating. The TO is defined as:

$$\begin{aligned}
\min_{\rho} \quad & c(\rho) = \mathbf{U}^T \mathbf{K} \mathbf{U} = \sum_{e=1}^n E_e(\rho_e) \mathbf{u}_e^T \mathbf{k}_0 \mathbf{u}_e \\
\text{s.t.} \quad & V(\rho)/V_0 - vf \leq 0 \\
& \mathbf{K} \mathbf{U} = \mathbf{F} \\
& g = \frac{\alpha}{T_{cr}} \left[\frac{1}{n} \sum_e ((1 - \kappa_e))^P \right]^{1/P} - 1 \leq 0 \\
& \mathbf{0} \leq \rho \leq 1
\end{aligned} \tag{3.18}$$

where c is the compliance of the structure, \mathbf{U} is the global displacement, \mathbf{F} is the force vector, \mathbf{K} is the global stiffness matrix, \mathbf{u}_e is the element displacement vector, \mathbf{k}_0 is the element stiffness matrix for an element with unit Young's Modulus, $V(\rho)$ is the material volume, V_0 is the design domain volume, and vf is the prescribed volume fraction. The domain is discretized with a structured mesh of bi-linear four-noded elements. The density filtering given by Bruns et al. [5] is used to smoothen the field and avoid the checkerboard pattern and impose a length scale in the optimized design. For optimization, the most commonly used example of the half MBB beam is used. The design domain dimensions, the external load, and the boundary conditions for the half MBB beam are shown in Figure 3.6. The same half MBB beam is used for all the simulations in this paper unless otherwise specified. The parameters used in the optimization are given in Table 3.2.

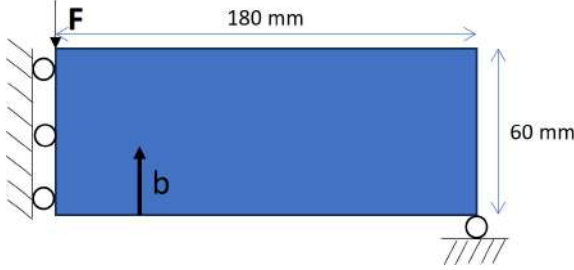


Figure 3.6: Half MBB beam used for the optimization. The load \mathbf{F} and build direction \mathbf{b} are as shown.

Parameters	Values
SIMP penalization	3
Volume fraction vf	0.5
Poisson's ratio	0.3
Density filter radius d	2
Critical temperature T_{cr}	0.8
Conductivity filter radius cf	12
P-mean exponent P	15
No. of iterations	600

Table 3.2: TO parameters

The design domain is discretized into 180×60 elements where 1 element is considered to be of size $1mm \times 1mm$. The 2D problem dictates a plane stress condition. Even though the out-of-plane thickness has no influence on the 2D conductivity estimation filter given in Section 3.2.3, an out-of-plane thickness of $50mm$ is considered for the calculation of the conductivity estimation filter radius cf . From this, the value is computed as $cf = 12mm$. The critical temperature value is taken as $T_{cr} = 0.9$ which means that every element will have at least 10% material surrounding them.

3.3.3. Topology optimization result using hotspot constraint

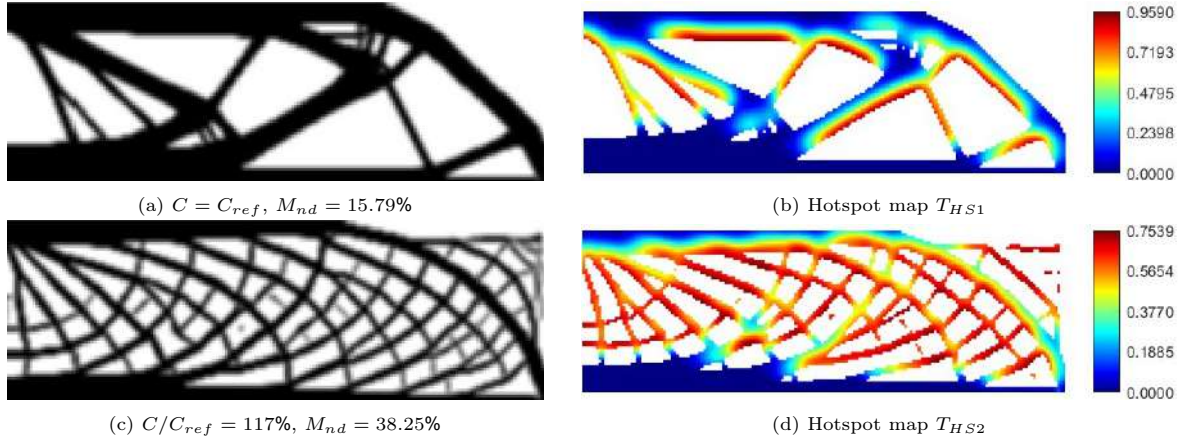


Figure 3.7: 3.7a TO without hotspot constraint, 3.7c TO with hotspot constraint and their corresponding hotspot maps in 3.7b and 3.7d respectively. Both designs have the same parameters except for the ones specific to the hotspot constraint.

The compliance minimization design with the hotspot constraint Figure 3.7c is compared against the reference design obtained without the hotspot constraint Figure 3.7a with compliance as C_{ref} . As seen in Figure 3.7c, because of the hotspot constraint there is a reduction in the length of the overhangs compared to the reference design, and thus, the maximum temperature in the domain reaches a value below $T_{cr} = 0.9$ Figure 3.7d which is lower than that in the reference design Figure 3.7b. However, in doing so the optimizer is adding material everywhere in the design domain even outside the base design that does not contribute structurally and thereby does not help in minimizing the compliance of the structure. This is because there is an upper bound on the maximum temperature $\max(\tilde{T}^\Omega) \leq T_{cr}$. This is mathematically equivalent to having a lower bound on the minimum conductivity $\min(\tilde{\kappa}^\Omega) \geq K_{cr}$, where $K_{cr} = 0.2$ is the critical conductivity, due to the relation given in Eqn 3.11. Because of this, the optimizer is trying to add material everywhere in order to have at least 20% local material distribution. Also, there is a significant utilization of intermediate densities $M_{nd} = 38.25\%$ as compared to $M_{nd} = 15.79\%$ in the reference design to artificially satisfy the constraint. The likelihood of utilization of intermediate densities becomes more dominant when the constraint becomes strict ($T_{cr} = 0.75, 0.7, \dots$) in order to satisfy the minimum conductivity requirement. The compliance of the design with the hotspot constraint is higher than the reference design by $C/C_{ref} = 117\%$ which is due to the reduced design freedom caused by the activation of the hotspot constraint.

3.4. Reformulation of constraint

The previous formulation had two major issues. Firstly, it was forming features outside the base design that did not contribute structurally. And secondly, overutilization of intermediate densities for artificially satisfying the constraint led to inferior designs. Also, a lot of thin features were forming everywhere just to have the minimum local conductivity satisfied. In AM printing process, these thin features will obstruct the heat flow leading to the enlargement of the melt pool just above it, and will therefore cause local overheating in those regions by Craeghs et al. [11]. Since there was no direct connection of the topmost layer to the baseplate as features were distributed everywhere, the heat had to conduct through a longer path causing inefficient heat evacuation which would defeat the purpose of this constraint. Therefore, it was necessary to modify the hotspot constraint presented in Section 3.3.1 to ameliorate the issues and serve its purpose correctly.

To avoid the intermediate densities for the calculation of local conductivity, the densities were penalized in a similar way as the SIMP method such that the intermediate densities are penalized to a very low value and the solids ($\rho = 1$) and voids ($\rho = 0$) are unaffected. The modified conductivity estimation filter is thus given as:

$$\bar{\mu}_e = \frac{\sum_{j \in N_e} \rho_j^q w_j}{\sum_{j \in N_e} w_j} \quad (3.19)$$

$$\tau_e = (1 - \bar{\mu}_e) \quad (3.20)$$

where, N_e represents the set of elements in the vicinity of element e defined as $|x_e - x_j| < r$ and $y_j \leq y_e$. $\bar{\mu}_e$ is the modified local conductivity with penalization on densities and $q > 1$ is the conductivity penalization factor, τ_e is the new pseudo elemental temperature. For initial iterations, a value of $q = 3$ was chosen in order to comply with the physics of the SIMP interpolation value. In order to make the constraint work, the constraint should be violated at the overhangs, which relates to the condition when there is a void below a solid element. Thus, when the constraint is violated at these solid elements, the constraint will force the optimizer to modify the densities around the solid element with void below. earlier, the constraint was getting violated at the voids leading to the addition of material (increase in local conductivity $\bar{\mu}_e$) around the void to satisfy the constraint which indeed led to the geometries forming outside the base design. To avoid this, the pseudo temperature is multiplied by an interpolation factor ϵ to relax the constraint at voids. Along with this, the constraint is now getting violated when there is a void below a solid element (overhang case). Thus, in order to satisfy the constraint the optimizer would increase the $\bar{\mu}_e$ by a finite amount. The constraint should be driven by the solid elements and not the void elements. Thus, it was necessary to relax the constraint at the void elements so there is no modification of local conductivity $\bar{\mu}_e$ because of them. The interpolation factor is defined as $\epsilon_e = \rho_e^r$ where ρ_e is the density of the central element over which the local conductivity $\bar{\mu}_e$ is being calculated and r is the interpolation exponent to which it is raised. ϵ_e is chosen in such a way that the constraint is relaxed when it is at a void ($\rho_e \approx 0$) i.e. the constraint is satisfied at void even without modifying the local conductivity $\bar{\mu}_e$. The value of r should be such that it should bring the density value close to 1 in order to make the constraint satisfy around voids. Also, it shouldn't do this in a sharp manner as a small perturbation in the design variable can lead to difficulties in the convergence of the problem, and it shouldn't be too smooth otherwise the constraint will not get relaxed at the void elements. From careful observation, a value of $r = 0.05$ was chosen as it had the best convergence among other values of r . A detailed parameter study of different values of q and r is given in Section 3.5.1.

Finally, a similar approach was taken as in the previous formulation to have the maximum temperature generated $\tilde{\tau}$ multiplied with the interpolation factor ϵ in the entire domain Ω to be less than a critical temperature value T_{cr} .

$$\max(\tilde{\tau}^\Omega) \leq T_{cr} \quad (3.21)$$

Applying P-mean and scaling factor α the reformulated constraint is given as:

$$g = \frac{\alpha}{T_{cr}} \left[\frac{1}{n} \sum_e (\tau_e \epsilon_e)^P \right]^{1/P} - 1 \leq 0 \quad (3.22)$$

$$g = \frac{\alpha}{T_{cr}} \left[\frac{1}{n} \sum_e ((1 - \bar{\mu}_e) \rho_e^r)^P \right]^{1/P} - 1 \leq 0 \quad (3.23)$$

3.4.1. Determination of critical temperature T_{cr}

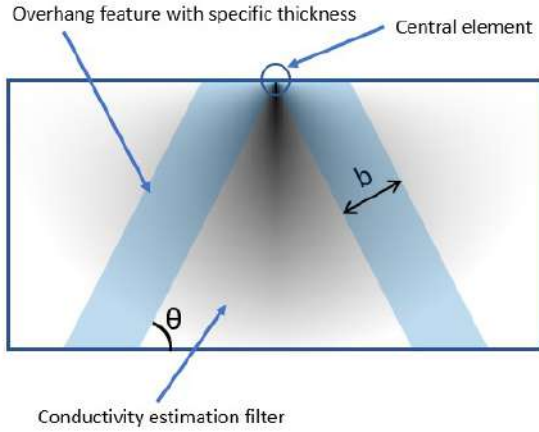


Figure 3.8: Overhang geometry for different angles θ and feature size b

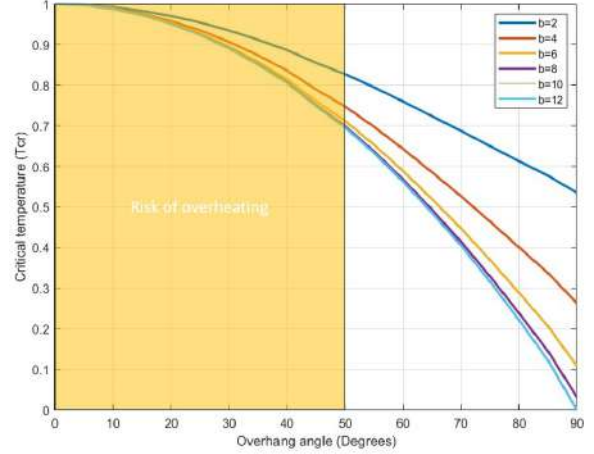


Figure 3.9: Critical temperature vs overhang angle for different feature size ($cf = 12$)

The critical temperature T_{cr} mentioned in Section 3.3.1 is defined in this section. The maximum temperature calculated using the conductivity estimation method depends upon the size of the conductivity filter radius cf as only the features captured inside the conductivity filter will be used to calculate the local conductivity and depending upon the feature size, the local temperature will be either high or low. Thus, a calibration process is used that involves the use of geometric features that are most prone to overheating and analyze them using the conductivity estimation method. This will give a relationship between the temperature and geometric features appearing in the design. Since the overhanging features are the worst performing when it comes to heat evacuation as given by Mertens et al. [27], they are used for the calibration of the critical temperature. This is not the only method and other calibration methods can also be used to determine T_{cr} . The goal is not to provide an overhang avoidance strategy but to evaluate the local conductivity behavior around these overhangs and link it to the maximum temperature that may occur in them.

The value of a critical overhang angle is experimentally determined using benchmark geometries in AM systems as given by Cloots et al. [9]. This implies that overheating may occur due to the thermal conditions when constructing overhangs with $\theta < \theta_{cr}$. From the design of an overhang, it is evident that the least conductivity will be for the element that is at the junction of the two overhangs as shown in Figure 3.8. The conductivity estimation method also complies with this as there are more elements adjacent to the central element that does not contribute much towards the heat evacuation and there is no material along the build direction that does contribute. Therefore, to test the maximum temperature for different overhang angles, a set of overhangs with different feature thicknesses b for a range of angle from $0^\circ - 90^\circ$ in the interval of 5° are taken. The conductivity filter is placed on the central element which is at the junction of the two overhangs and the local conductivity for that element is calculated. The maximum temperature is then evaluated using Eqn 4.17. The conductivity filter is chosen as 12 and feature sizes from 2-12 in the interval of 2 are taken in the interval of 2 for the calculation of maximum temperature. This maximum temperature will be used to set the limit T_{cr} for a given design having the maximum overhang angle as θ_{cr} .

The variation of critical temperature with overhang angle for different feature sizes is shown in Figure 3.9. The overhang angle θ is defined from the horizontal i.e. $\theta = 0^\circ$ which means maximum overhang and $\theta = 90^\circ$ means the entire layer is supported underneath. From this, it can be seen that the lower the angle θ , the higher the overhang and the greater the critical temperature and overheating risk. The most commonly followed threshold for the maximum overhang to have self-supporting structures is 45° . If we want to go higher than this i.e. $\theta < 45^\circ$, the risk of overheating increases. The critical temperature for all the feature sizes is 0 for $\theta = 0^\circ$. This is because there is no material underneath ($\mu_e = 0$) to conduct heat and thus, the local temperature (τ_e) goes to 1. As θ increases, the overhang decreases. Correspondingly, the local conductivity of the central element increases, and we see a drop in the maximum temperature obtained. It is important to note that for the same critical temperature,

the maximum overhang angle θ_{cr} is possible for a relatively lower feature size increases i.e. overhang decreases. For e.g., in a design with $T_{cr} = 0.8$, the features with thickness 2 will have a maximum overhang angle of 53° (less overhang), whereas features with thickness 12 and above can go up to a maximum overhang angle of 40° (more overhang). This is because the lower feature size has less material to conduct heat and to have the same critical temperature it has to increase θ (lower the overhang). Therefore, the limiting case would be the feature size equal to the conductivity filter radius size. For $b = 12$, which is equal to the conductivity filter size, the local conductivity of the central element goes to 1 for $\theta = 90^\circ$ as all the material is available for conduction and the critical temperature goes to 0. Therefore, the critical temperature value will be crucial to limit overhang features in the design from going beyond a specific critical overhang angle based on their feature size. A detailed evaluation of designs for different T_{cr} is given in Section 3.5.2.

3.4.2. Robust formulation on the design

The reformulated constraint given in Section 3.4 was used in the robust TO given by Wang et al. [46] in order to have a length-scale control over the features formed and to better utilize the black-and-white geometry for the calculation of local conductivity $\bar{\mu}_e$. Also, it has been shown by Wang that, a simple Heaviside threshold projection method is not sufficient for having a length scale control as the length scale can be ensured only on the solid $\eta = 0$ or the void $\eta = 1$ phases, where η is the threshold parameter. Hence, in robust TO two different projection thresholds are used to have a length-scale control on both the solid and void phase. The robust approach is typically employed to offer robustness against manufacturing process uncertainties where the part boundaries may vary during fabrication. It uses three designs called the eroded $\bar{\phi}_e$, intermediate $\bar{\phi}_i$, and dilated $\bar{\phi}_d$ designs using thresholds as η_e, η_i , and η_d respectively. Here, $\eta_e = 1 - \eta_d$ and the intermediate design threshold η_i is taken as 0.5. Based on the thresholds, the designs are either projected to 1 if they are greater than the threshold or 0 if they are lower than the threshold by the equation:

$$\rho = \bar{\phi} = \frac{\tanh(\beta\eta) + \tanh(\beta(\bar{\phi} - \eta))}{\tanh(\beta\eta) + \tanh(\beta(1 - \eta))} \quad (3.24)$$

where β is the sharpness of the projection and η and ρ are the threshold value parameter and projected design variable respectively. The constraint was added to all three designs to investigate the best-performing design as shown in Figure A.4. The designs obtained were analyzed using the slab analysis hotspot detection method given by Ranjan et al. [32], see Appendix A.4. From this, the best performing one was when the constraint was added to the eroded design. This is because, they have the least volume and thus, the least heat conduction among the three designs. The compliance is computed as a min-max problem such that the maximum compliance out of the eroded, intermediate, and dilated design is taken for the computation of minimum compliance optimization. However, it is shown by Lazarov et al. [22] that for the sake of computational benefits, only the eroded design can be used for compliance minimization as it will have the highest compliance out of the three designs. The volume constraint is added to the dilated design as it has the highest volume among the three designs and the intermediate design volume is scaled to that of the dilated design in a continuation approach so that the volume fraction is consistent with the prescribed value.

The result for the new formulation is given in Figure 3.23. The intermediate design is shown on the left 3.11a, 3.11c, and the hotspot constraint on the intermediate design is shown on the right 3.11b, 3.16h for both with and without the hotspot constraint. The parameters used for the simulation are given in Table 3.3. A critical temperature value of 0.8 was chosen to generate the design with the hotspot constraint. The projection sharpness β was initiated to 1 and incremented every 100 iterations to a maximum of 16. This was done to have a smoother transition from the intermediate design and give the constraint enough time to modify the design variables leading to better convergence. However, this increases the number of iterations needed to achieve proper convergence. A larger density filter radius $d = 4$ is used to avoid thin sections in the design. It can be seen from Figure 3.10 illustrates how P-mean underestimates the maximum temperature in the design domain and scaling to the true maximum of the domain is required as explained in Section 3.3.1.

The conductivity estimation hotspot constraint pushes the optimizer to redistribute the material in such a way that there is at least a certain amount of material (local conductivity) defined by the Eqn

3.19 around each element it goes through. This will result in the temperature to be lower than the specified limit given by Eqn 4.18. E.g., for $T_{cr} = 0.8$ as in this case, there should be at least 0.2 or 20% material distribution around each element for the local temperature to be lower than 0.8. This should be true for all the elements in the design domain. Thus, the global maximum from all the elemental temperatures will be lower than the critical temperature limit of 0.8 which ensures that local overheating is avoided in each of the elements. The idea of avoiding overheating risk is to prevent the features from going beyond the critical overhang angle θ_{cr} and provide a sufficient pathway for the heat to evacuate. The figure shows how the designs change over the iterations and that the constraint is eliminating the overhangs in the design because of which, the maximum temperature in the hotspot constraint design is much lower ($T_{max} = 0.77$) than the reference design ($T_{max} = 0.97$) as given in Figure 3.16h and 3.11b respectively. The images are generated using the equation given in Eqn 4.17. Note that, since the eroded design has the least volume, it will show the highest temperature among the three designs. If we run a conductivity estimation analysis post-optimization on the intermediate and dilated design, they will show a lower maximum temperature than the eroded design ensuring safer designs. Also, according to the T_{cr} vs overhang angle relation given in Section 3.4.1, the minimum overhang angle in the design is 40° , whereas, in the reference design, we can see overhang angles of 0° which causes serious issues of heat accumulation. The tear-drop-shaped voids allow for an acute overhang angle and also prevent thermal-bottleneck in the design which was seen in the previous iteration Figure 5.4. The compliance of the structure is only 20% higher than the reference design which means there is not much compromise in the compliance of the structure with the benefit of reduced overheating.

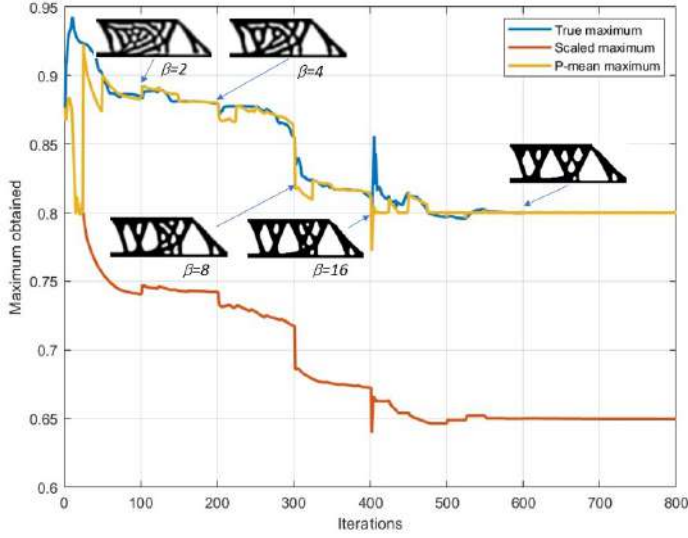


Figure 3.10: Illustration of the hotspot constraint being satisfied

Parameters	Values
SIMP penalization	3
Volume fraction vf	0.5
Poisson's ratio	0.3
Density filter radius d	4
Critical temperature T_{cr}	0.8
Conductivity filter radius cf	12
Projection sharpness β_{max}	16
Threshold dilated η_d	0.25
Threshold intermediate eta_i	0.5
P-mean exponent P	25
Conductivity penalization q	3
Interpolation exponent r	0.05
No.of iterations	800

Table 3.3: Robust TO parameters

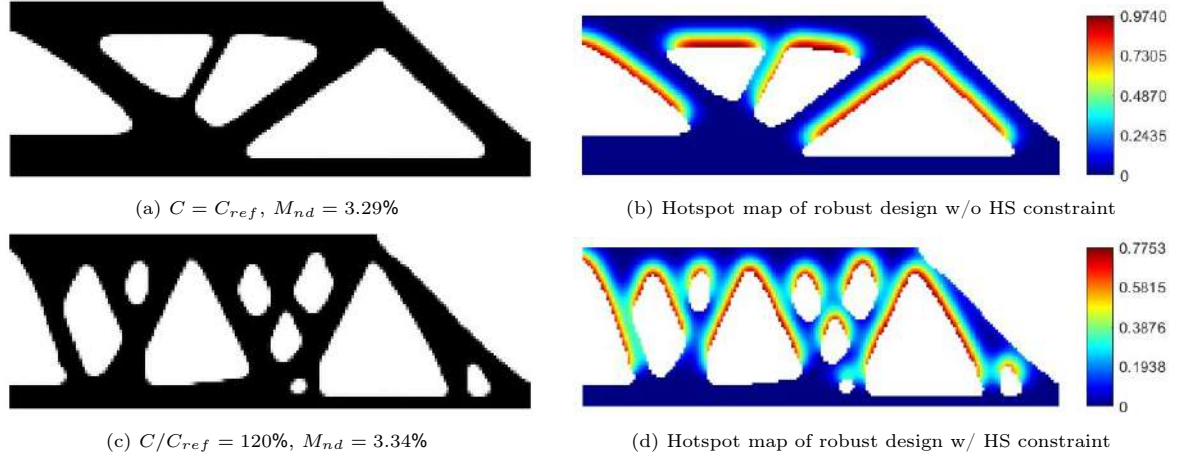


Figure 3.11: 3.7a Robust TO without hotspot constraint, 3.7c Robust TO with new hotspot constraint and their corresponding hotspot maps in 3.7b and 3.7d respectively. Both designs have the same parameters except for the ones specific to the hotspot constraint.

3.5. Parameter study

3.5.1. Influence of conductivity penalization and interpolation factor

It is important to understand the influence of the penalized conductivity $\bar{\mu}$ and the interpolation factor ϵ used in Eqn 4.18 in the constraint function and the respective designs obtained. For this, a parametric sweep has been done for different values of the conductivity penalization factor q and the interpolation exponent r as shown in Figure 3.12. The values of conductivity penalization are taken as $q = 1, 3, 5$ which are along the columns and interpolation exponent as $r = 0.5, 0.1, 0.05, 0.01$ which are along the rows in Figure 3.12. All the parameters are taken from Table 3.3 and only the q and r values were varied. The compliance and maximum temperature plot for all these designs are given in Appendix A.5.

A graph of the function value of using these exponents is shown in Figure 3.13. For the constraint to work it is important that the constraint is violated when there is a void below a solid element which is the overhang case, so that the optimizer tries to add more material underneath i.e. increase $\bar{\mu}_e$ in order to satisfy the constraint. From the figure, it is evident that the intermediate densities ρ are penalized for $q > 1$, and this effect becomes more prominent for higher values of q . As a result, the use of intermediate densities to artificially satisfy the constraint is reduced. However, it is only useful during the initial iterations of the optimization where β value is low. As the β value increases, the design becomes more crisp and densities are close to 1/0. But if the conductivity penalization is very high in the beginning i.e. $q = 5$, the effect of intermediate densities is drastically reduced and the design already converges to a black-and-white design even before the β is updated. Once this happens the optimizer finds it very difficult to update the design variables and satisfy the constraint. As a result, all the designs shown in Figures 3.12c, 3.12f, 3.12i and 3.12l violate the hotspot constraint as their maximum temperature value T_{max} exceeds $T_{cr} = 0.8$.

By having a high value of interpolation exponent i.e. $r = 0.5$, the constraint is very easily satisfied when there is a void below a solid element and is violated when there is a solid below a void element. Due to this, the constraint doesn't add material underneath the void element and modifies the densities around the solid element in order to satisfy the constraint. Thus, the maximum value goes beyond critical value as overhangs still exist in the design as shown in Figures 3.12a to 3.12c. If we lower the interpolation exponent to a very low value i.e. $r = 0.01$, the constraint is violated very much in the solid elements when there is a void below. As a result, the optimizer tries to increase the value of $\bar{\mu}_e$ to a very high value in order to satisfy the constraint. This is indicative from the design in Figures 3.12j and 3.12k that the optimizer tries to add material in very close proximity, which satisfies the constraint but leaves behind many isolated features. The designs shown in Figures 3.12d and 3.12g for $q = 1$ seem to be giving a good result for $T_{cr} = 0.8$. But as the constraint is made more strict i.e. for $T_{cr} = 0.7$, the densities are more densely packed in order to have the minimum local conductivity of 30%. As the densities are not penalized, the constraint is prematurely satisfied using intermediate densities. But as

β is updated to a higher value, the intermediate densities are eliminated and the designs converge to better results. However, their maximum temperature value goes beyond the critical temperature by a small amount. Out of the designs shown in Figures 3.12e and 3.12h, the design with $r = 0.05$ has a lower maximum temperature $T_{max} = 0.77$ as compared to $T_{max} = 0.79$ for $r = 0.1$, meaning the former one has better local overheating avoidance than the later. Since the objective of this paper is to limit the local overheating in designs, the values of $q = 3$ and $r = 0.05$ are chosen for the simulations. However, the compliance of 3.12e is slightly better than 3.12h design and depends upon whether our priority is limiting local overheating or minimizing the compliance of the structure for the selection of these values.

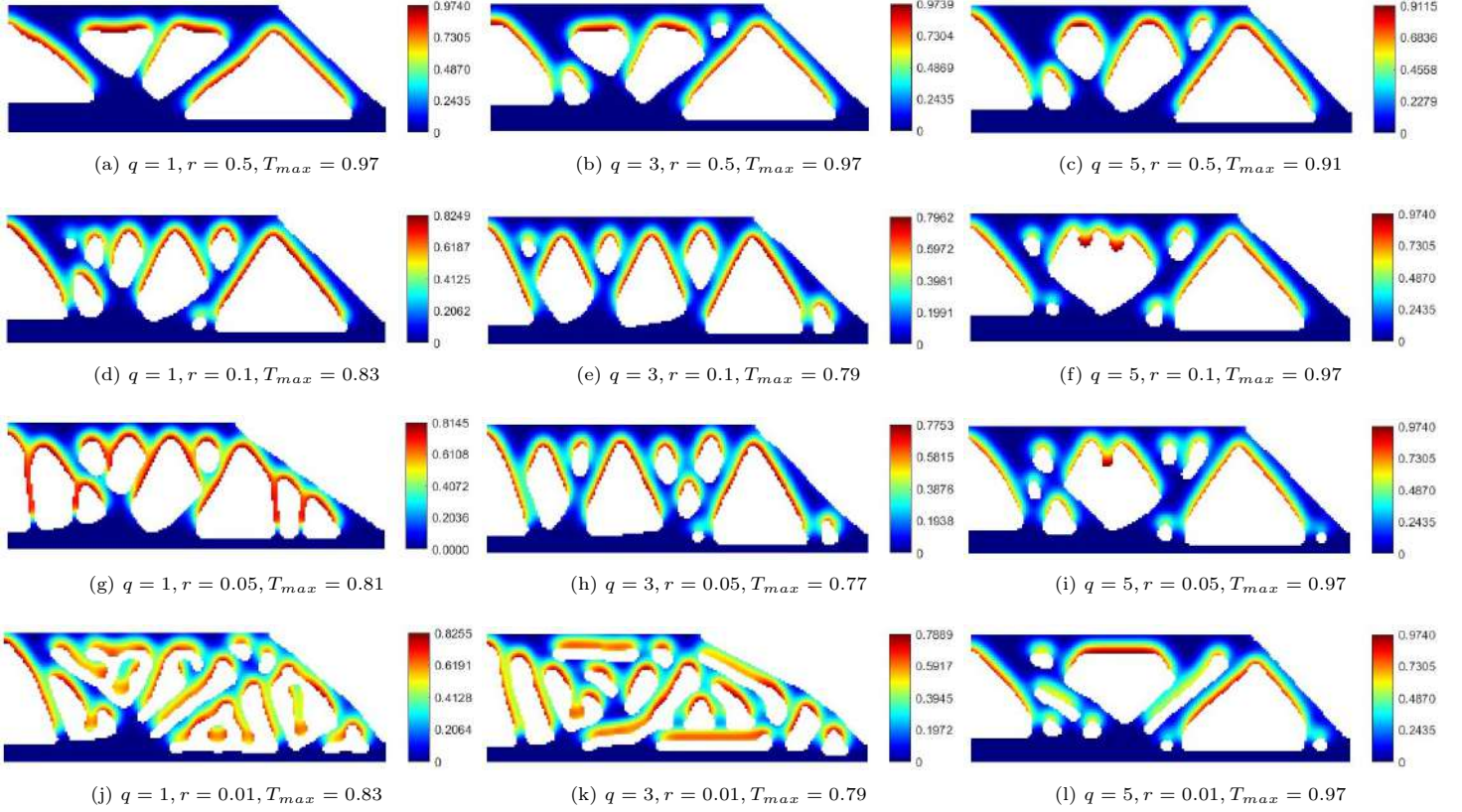


Figure 3.12: Parametric sweep of conductivity penalization q and interpolation exponent r for $T_{cr} = 0.8$

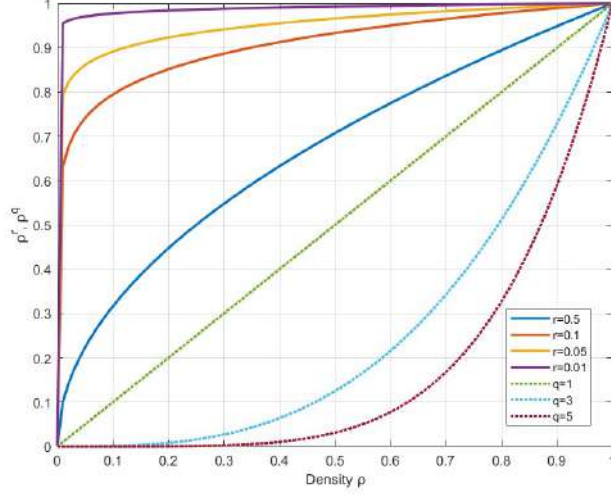


Figure 3.13: Plot for different values of interpolation factor $\epsilon = \rho^r$ and conductivity penalization ρ^q .

3.5.2. Influence of critical temperature T_{cr}

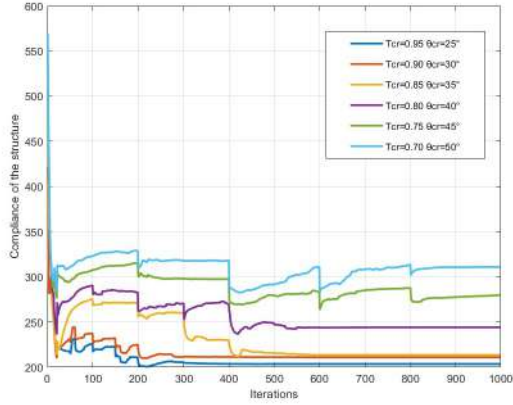


Figure 3.14: Compliance plot of the structures with different T_{cr}

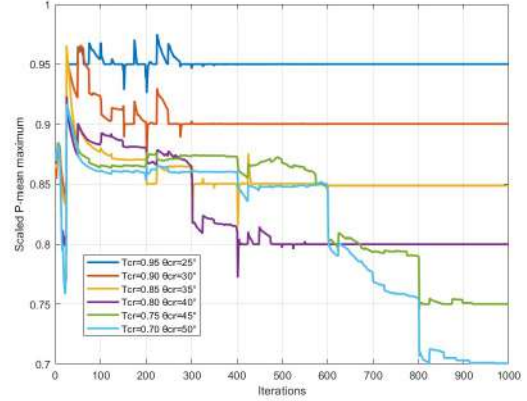


Figure 3.15: Scaled P-mean maximum value of the structures with different T_{cr}

In Section 3.4.1, a calibration scheme is used to determine critical temperature T_{cr} based on the overhang angle of different feature sizes. Recall that for a given T_{cr} , the limiting case for critical overhang angle θ_{cr} was when the feature size b was equal to the conductivity filter size cf . From Figure 3.9, since the filter size used for the simulation is $cf = 12$, the $b = 12$ curve will be used to determine the θ_{cr} . Another approach to finding the θ_{cr} for a given T_{cr} is to look at the relationship between η , b , R for determining the minimum length-scale in the design given in [46] as $b/2R$. For our case, it gives $b = 8$ for $\eta = 0.25$, and $R = 4$, whose curve is almost overlapping the $b = 12$ curve until the overheating risk zone given in Figure 3.9. The results for $T_{cr} = 0.95, 0.9, 0.85, 0.8, 0.75, 0.7$ which corresponds to $\theta_{cr} = 25^\circ, 30^\circ, 35^\circ, 40^\circ, 45^\circ, 50^\circ$ respectively is given in Figure 3.16. The maximum temperature constraint is met in all of these eroded designs as can be seen in Figure A.6. Since the intermediate design has more volume than the eroded one, the designs are even safer. Figure A.5 shows the compliance of the intermediate structure. It is clear that, as the constraint becomes more strict i.e. T_{cr} goes from 0.95 to 0.7, the optimizer has to compromise the objective function of minimizing the compliance in order to lower the maximum temperature in the design and satisfy the constraint which is a direct result of the design freedom getting reduced. Also, for a stricter constraint due to the slow β update the number of iterations taken to convergence increases.

The intermediate designs for different critical temperature values and their respective intermediate design hotspot maps are given in Figure 3.16. The figures on the left show the overhang angle θ that is associated with the given feature. The build direction b is shown by the upward arrow. All parameters are similar to that given in Table 3.3 except for the no.of iterations, β update cycle, and lower limit on constraint c in the MMA solver. As the constraint becomes more strict, it requires more iterations to converge and thus the β has to be updated slowly. Thus, β is updated after 50 iterations for $T_{cr} = 0.95, 0.9$, after 100 iterations for $T_{cr} = 0.85, 0.8$, and after 200 iterations for $T_{cr} = 0.75, 0.7$. Due to this, the number of iterations required for convergence also increases. The c parameter in the MMA solver is a degree of strictness applied to the constraint. Thus as we go for lower critical temperature values, this value is increased.

The hotspot constraint adds material around an element if its local conductivity $\bar{\mu}_e$ is low. The amount of material addition depends upon the maximum acceptable temperature in the design domain. Thus, the lower the temperature limit, the higher the material distribution requirement around each element. The high-temperature regions are indicated by the red color according to the color bar. They mostly highlight the overhangs and thin features in the design which due to low material distribution in their vicinity conduct heat poorly. It is evident from the figures that, as the constraint becomes strict the degree of overhang decreases in order to reduce the maximum temperature generated in the design. The overhangs tend to get more vertical as more material is required underneath a layer to satisfy the minimum material requirement. E.g., the critical overhang angle for $T_{cr} = 0.8$ is 40° Figure 3.16g whereas it is 50° for $T_{cr} = 0.7$ Figure 3.16k. However, some short overhangs can be seen to be below this θ_{cr} value for a given T_{cr} , but they do not cause a problem with local overheating as there is sufficient material around them for the heat to conduct as shown in Figure 3.16e. Also, the thinner features have a lower overhang than the thicker ones as they have less material to conduct heat and so they orient themselves in a way such that they don't go beyond the permitted temperature limit. E.g., in Figure 3.16c the thinner feature indicated by 'A' has a smaller overhang $\theta = 69^\circ$ than the thicker feature $\theta = 40^\circ$ indicated by 'B'. As the constraint becomes more strict, the topmost layer gets directly connected to the baseplate as the features tend to straighten up which ensures efficient heat evacuation. Also, the funnel-like structures creating thermal bottlenecks that appear for a lower critical temperature tend to go away as the constraint becomes more strict. This gives rise to the tear-drop-shaped voids which are also seen in the physics-based hotspot constraint topology optimized design by Ranjan et al. [32]. The measure of non-discreteness M_{nd} is more or less the same for all the geometries as they are all projected to the same β_{max} value of 16.

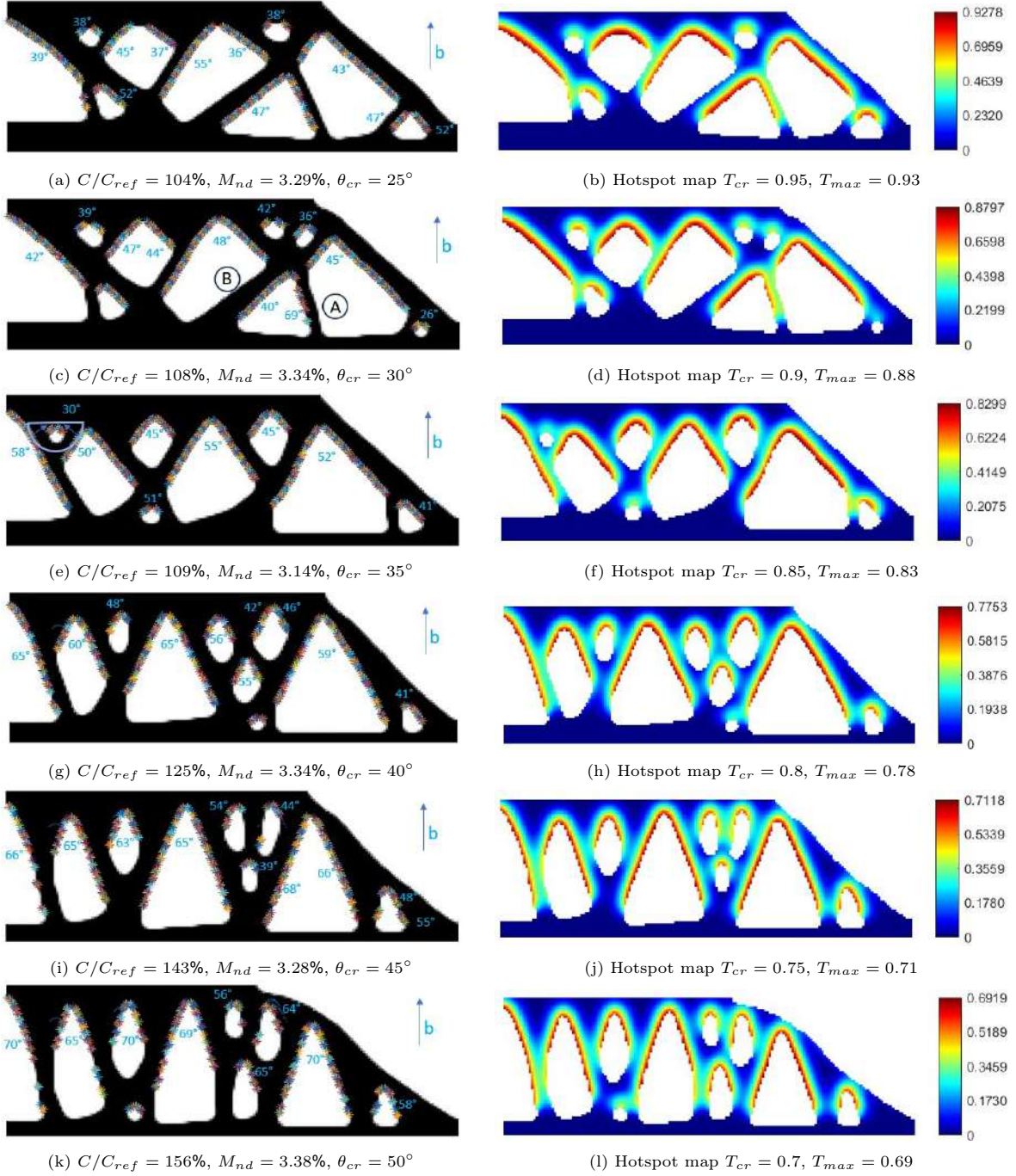


Figure 3.16: Robust TO designs with hotspot constraint for different T_{cr} Figures 3.16a, 3.16c, 3.16e, 3.16g, 3.16i and 3.16k. Corresponding hotspot map with maximum temperature value Figures 3.16b, 3.16d, 3.16h, 3.16j, 3.16l and 3.17d

3.5.3. Influence of conductivity filter radius cf

A conductivity filter radius of $cf = 12$ has been used until now to do all the simulations as this was the thermal interaction length s we got for our given design space and material properties as per the Eqn 3.7. To check the influence of the conductivity filter radius we do simulations using a smaller $cf = 6$ and a larger $cf = 20$ conductivity filter radius as shown in Figure 3.17. The size of the conductivity filter is shown using the blue semicircle. Both the designs converge and satisfy the constraint limit of $T_{cr} = 0.85$. The design for $cf = 12$ is also presented for comparison. From the analysis, it was found that the designs obtained were very much dependent upon the size of the conductivity filter used as it

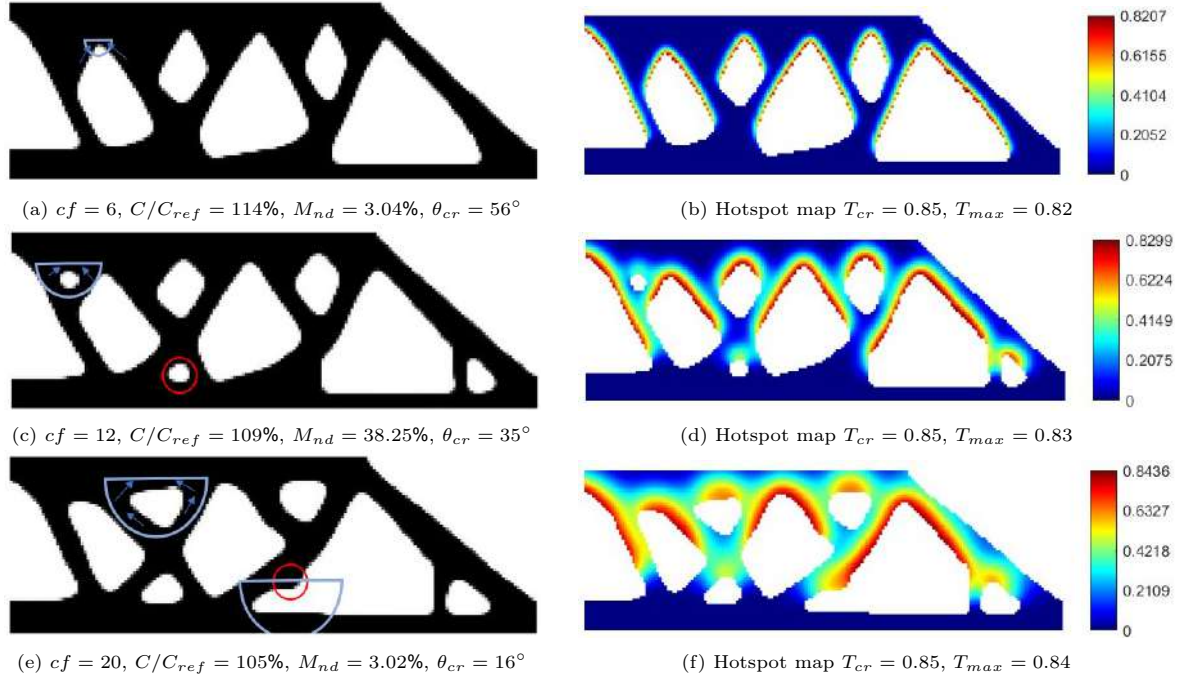


Figure 3.17: Robust TO designs using different conductivity filter size Figures 3.17a, 3.17c and 3.17e. Corresponding hotspot maps with maximum temperature Figures 3.17b, 3.17d and 3.17f

would govern the hotspot constraint for the available design freedom during the optimization process.

Figure 3.17a, 3.17e show the design for $cf = 6$ and $cf = 20$ and the corresponding hotspot map in Figure 3.17b, 3.17f respectively. In $cf = 6$, as the conductivity filter size is less, less material is captured by the conductivity estimation filter and thus, it shows the high temperature at every edge as the influence of neighboring elements is much less. Due to this, the constraint becomes strict and there is a reduction of the design freedom. This results in the compliance value to increase $C/C_{ref} = 114\%$ as compared to $cf = 12$ design whose $C/C_{ref} = 109\%$. Also, since the constraint becomes strict, the degree of overhang reduces in order to keep the maximum temperature below the specified limit. On the other hand, with $cf = 20$ a large number of elements are captured in the vicinity of the central element and thus, the influence of neighboring elements is more. This makes the constraint less strict and gives the optimizer more design freedom $C/C_{ref} = 105\%$. Since the conductivity filter radius is large, the influence of neighboring elements increases as shown in Figure 3.17e where the optimizer allows some overhangs in the design as the heat can conduct through the elements around the void (shown by blue arrows inside the conductivity filter). In Figure 3.17a, it can be seen that the circular void which is shown with a red circle in Figure 3.17c is gone. This is because, the size of the conductivity filter is lower than the size of the void and thus, it goes beyond the critical temperature limit due to lack of material to conduct. Whereas, in the $cf = 20$ design, due to the larger filter size, the overhang can appear anywhere as shown with a red circle in Figure 3.17e as there is enough material around it to conduct heat and lower the temperature. Thus, these features are avoided in the $cf = 6$ design. Note that, inside solids, since the filter size is low it captures all the material and yields a very low temperature in the inner regions as compared to $cf = 12$ and $cf = 20$ designs.

Another observation has been made by using a conductivity filter of size $cf = 6$ on the geometry made using $cf = 20$ as shown in Figure 3.18a and the other way around in Figure 3.18b. The blue semicircle shows the conductivity filter size used for making the design and the black semicircle shows the conductivity filter size used for hotspot analysis post optimization. As can be seen from Figure 3.18a the smaller conductivity filter is showing high-temperature regions in the overhangs due to a lack of material in the vicinity for heat evacuation. This results in the maximum temperature $T_{max} = 0.9$ in the geometry going beyond the critical temperature of 0.85. A different scenario is observed in Figure

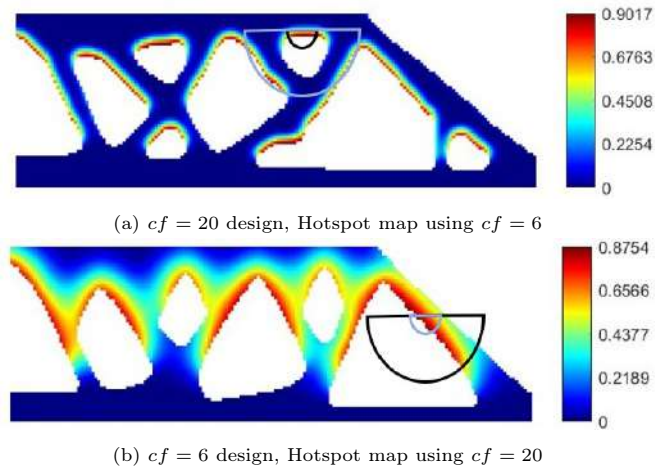


Figure 3.18: Hotspot map generated using different conductivity filter size post-optimization. The blue semicircle represents the conductivity filter size used for making the design and the black semicircle represents the conductivity filter size used for hotspot analysis post-optimization.

3.18b. Since the filter radius is large, it encapsulates a large amount of area and as shown using the conductivity filter, most of this area is void thus, it shows a high temperature in that region, and the hotspot constraint is violated. These results imply that if the conductivity filter size is much greater or lower than the thermal interaction length s appropriate for the specified set of process and material characteristics, overheating avoidance cannot be assured. Therefore, it is of utmost importance to choose the right thermal interaction length for the selection of the conductivity filter radius in order to obtain feasible designs.

3.6. Comparison between different designs used for controlling local overheating

3.6.1. Temperature results from transient LBPF process simulation

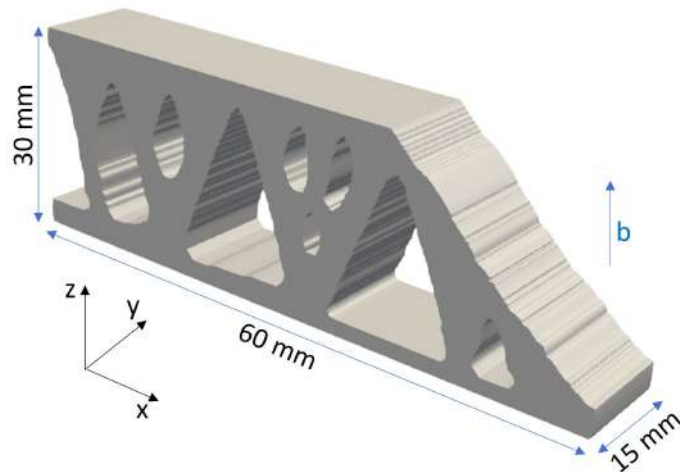


Figure 3.19: Part geometry dimensions used for the transient LBPF process simulation. The build direction is indicated by the blue arrow.

To study the effectiveness of the simplified models used for controlling local overheating, a high-fidelity LBPF process transient simulation was done. The goal was to understand the heat accumulation tendencies in these structures during the manufacturing process. The simulation was done on four

different structures: robust TO design by Wang et al. [46], TO design with an overhang constraint by Langelaar et al. [19], TO design with a simplified thermal model hotspot constraint by Ranjan et al. [32], and the TO design with conductivity estimation hotspot constraint given in this paper. The 2D geometries are extended in the third dimension to make a 2.5D model for the transient simulations. All four geometries have a size of $90\text{mm} \times 30\text{mm} \times 15\text{mm}$ with build direction along the z-direction as shown in Fig 3.19. The reference thermal LPBF process model used is the same as that used by Ranjan et al. [33]. The model uses a body that is attached to the baseplate, with layer-by-layer deposition. The part-powder interface is considered insulated due to the lower bulk conductivity of powder as compared to the solidified material. Heat loss through conduction, convection, and radiation as well as the temperature-dependent thermal properties are considered.

Finite element analysis is employed to solve the boundary value problem. The element birth-and-death method is used to simulate the growing domain during AM processes by Roberts et al. [36], Zhang et al. [51]. This is implemented in the open-source FE analysis code, CalculiX [12], using a structured mesh aligned with the layered structure. Eight-node linear cubic elements are utilized, with the mesh size set to match the superlayer thickness of $500\mu\text{m}$. Harrison et al. [51] support the choice of a super layer thickness of $480\mu\text{m}$ for accurate temperature responses under typical LPBF machine conditions. The actual LPBF layer thickness of $50\mu\text{m}$ is used, making the superlayer ten times thicker. In each simulation cycle, the deposited superlayer undergoes heating with a uniform volumetric heat source, for a given heating time. The bottom surface nodes act as heat sinks at a constant temperature. The absorbed energy matches the process energy, and the volumetric heat source accounts for the real LPBF layer thickness. An ILT of 100 seconds, derived from Harrison’s scaling [51], is chosen for cooling between layer depositions. The temperature-dependent properties of Ti-6Al-4V are taken from Davies [8]. For more details about the transient simulation, readers are referred to [33].

Due to simplifications, the temperature found during this analysis do not represent actual transients experienced during the process. Instead, they signify heat accumulation tendencies associated with different geometric features of the AM part. The maximum temperature at the end of the heating step is used to generate the hotspot map as shown in Figure 3.20. The geometries shown in Figures 3.20b to 3.20d are generated such that the worst case overhang is at $\theta_{cr} = 45^\circ$ to facilitate a fairer comparison. Also, a consistent temperature scale is applied, ranging from the sink temperature of 180°C to the highest temperature within all designs. It is evident that the TO structure without any constraint in Figure 3.20a goes to a relatively very high temperature of $T_{max} = 1152.9^\circ\text{C}$. This is due to the existence of long overhangs in the design which causes severe overheating. However, constraining the design to have a common overhang angle also does not ensure overheating risk prevention. This is illustrated in Figure 3.20b where all the overhangs have a common angle of 45° . This is because the funnel-like structures that are formed lead to a thermal bottleneck in the design which causes the temperature to rise up to a maximum of 680.6°C . Hence, an understanding of the influence of the neighboring features is necessary to limit the maximum temperature in the design. This is done in the structure generated using slab-analysis hotspot constraint (physics-based) which emulates the thermal behavior around the features to eliminate features that cause local overheating. This results in a lower maximum temperature of 604.5°C . The geometry generated using the conductivity estimation hotspot constraint (geometry-based) behaves in a similar manner as it estimates the local conductivity around each element and restricts it above a threshold value. This way the local conductivity everywhere is sufficient and the maximum temperature rise is limited to only 566.1°C .

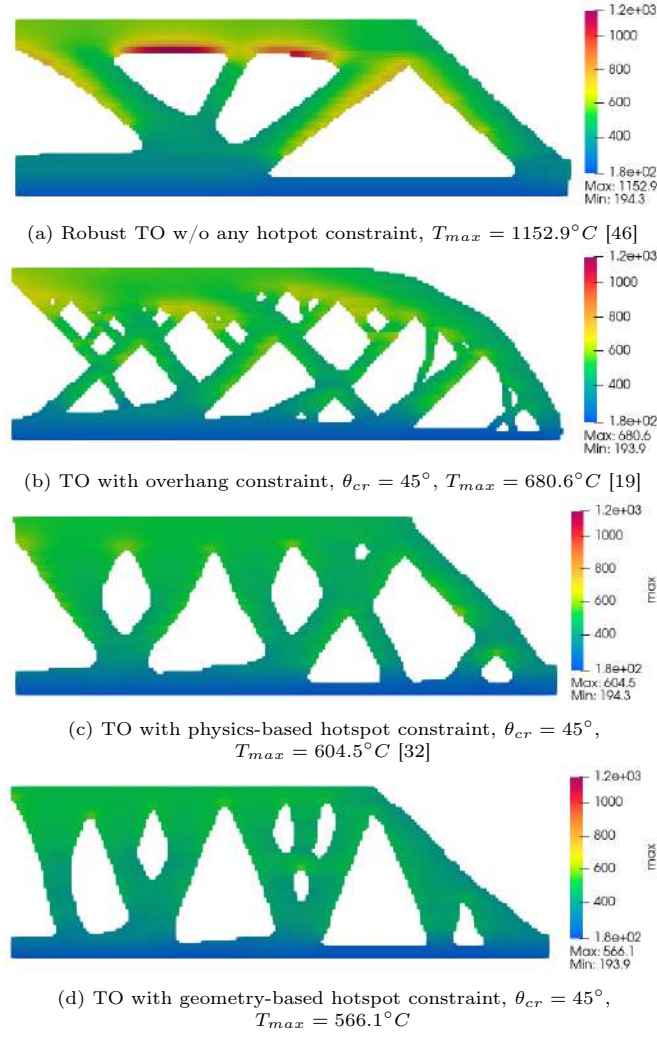


Figure 3.20: High-fidelity transient LBPf process simulation for different TO models used for controlling local overheating in Figures 3.20b to 3.20d compared with the reference robust TO model without any constraint. The constrained designs are simulated to have a common critical angle of $\theta_{cr} = 45^{\circ}$. The maximum temperature generated during the simulation is given in the sub-captions.

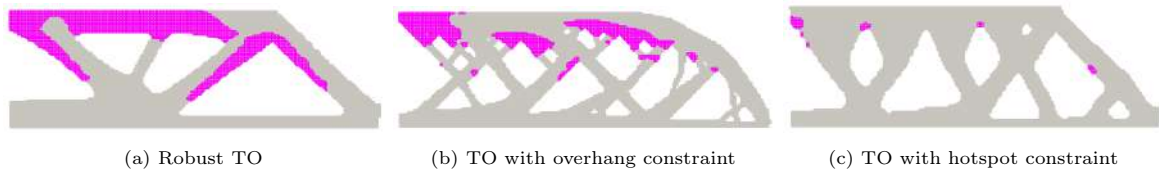


Figure 3.21: Contour plot generated for the three designs whose maximum temperature is higher than the temperature in geometry-based hotspot constraint design $T > 566^{\circ}C$ highlighted in pink.

A plot of the regions where the temperature is higher than the maximum temperature in the conductivity estimation design is shown in Figure 3.21. The highlighted area in pink shows the regions where the temperature is greater than $566^{\circ}C$ obtained in the geometry-based hotspot constraint design, which is taken as a threshold for this contour plot. It is noteworthy that the threshold temperature does not guarantee that local overheating will not happen below this temperature. It is just to use it as a lower limit and highlight the features that go beyond this temperature in other designs. The lower the maximum temperature generated, the lower the local overheating, and the better would be the performance of the fabricated part. As illustrated in Figure 3.21a, the overhangs are susceptible to very high temperatures. In Figure 3.21b, due to the funnel-like and thin structures, heat is not con-

ducted efficiently, which causes high temperatures near those regions. The maximum temperature in the physics-based design is higher than in the geometry-based design, which can be due to the presence of funnel-like structures in Figure 3.21c. Even though they are less prominent than those in overhang constraint design in 3.21b, they still account for thermal bottlenecks and gradual heat accumulation. However, we cannot conclude that the geometry-based hotspot constraint design will always give a lower temperature in all situations. The only takeaway from this comparison is that the result from the conductivity estimation hotspot constraint is comparable to a more thermally accurate hotspot constraint, which is the physics-based hotspot by Ranjan et al. [32].

3.6.2. Computation time comparison

A comparison of the computation times has been done to see the time taken to generate the designs presented in Section 3.6.1. The computer used for the computation of times has a 3.2 GHz processor with 16 GB of RAM and 8 cores. The average CPU time obtained per iteration was recorded and listed as shown in Table 3.4. The code was not very optimized, and minimal parallel computing was used. From the results, it is evident that the geometry-based hotspot constraint design is faster than the physics-based hotspot constraint design. The physics-based slab analysis design in Ranjan et al. [32] has fewer equations to solve than the geometry-based design conductivity estimation design over the entire domain. However, the number of entities within those equations is higher in the former method due to the consideration of the entire rectangular domain as compared to a semicircular domain in conductivity estimation. The computation timing of the conductivity estimation method can be further improved by vectorizing the computed arrays.

Table 3.4: Average CPU time per iteration for different designs mentioned in Section 3.6.1.

Models	CPU time/iteration (sec)
Robust TO	0.15
TO with overhang constraint	0.35
TO with physics-based hotspot constraint	1.34
TO with geometry-based hotspot constraint	1.10

3.7. Extension to 3D

The idea of the conductivity estimation method in 2D can be extended to 3D geometries as well with a slight modification in the conductivity estimation filter. The conductivity estimation filter which was a semicircle in 2D becomes a hemisphere in 3D in order to encapsulate all the features in the three-dimensional domain. The weights defined in Section 3.2.2 are used to penalize the effect of elements that are adjacent and far away from the central element. The grayscale of the conductivity estimation filter shown in Figure 3.23a is an indication of the influence of neighboring elements on the local conductivity i.e. darker shade means higher influence and vice versa. The orientation of the conductivity filter again depends upon the build direction to capture the densities of only the elements that are already printed as shown in Figure 3.23a. The size of the conductivity filter, just like in 2D, depends upon the thermal interaction length given in Section 3.2.3. The hotspot map generated using this conductivity estimation method is shown in Figure 2.1a. The conductivity estimation filter moves along and through the layers encapsulating the nearby elements' densities and computes the local conductivity of each and every element in the domain. The hotspot map is then generated using Eqn 4.17. Again, the high-temperature zones are the overhanging features that have no material underneath them to cause sufficient heat evacuation.

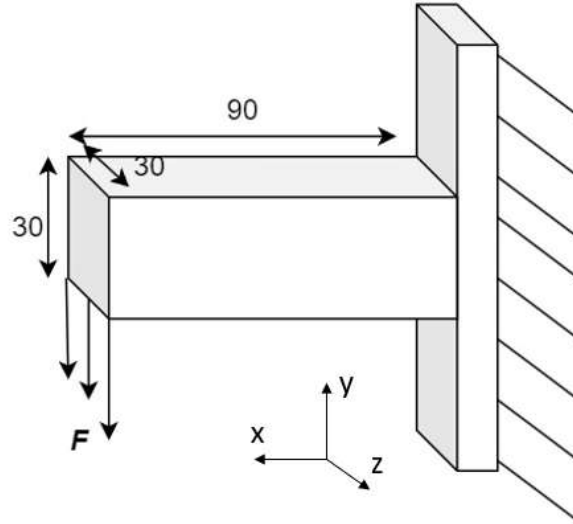


Figure 3.22: Design space and boundary conditions for the 3D simulations. A cantilever beam with one face fixed and load acting on bottom front edge.

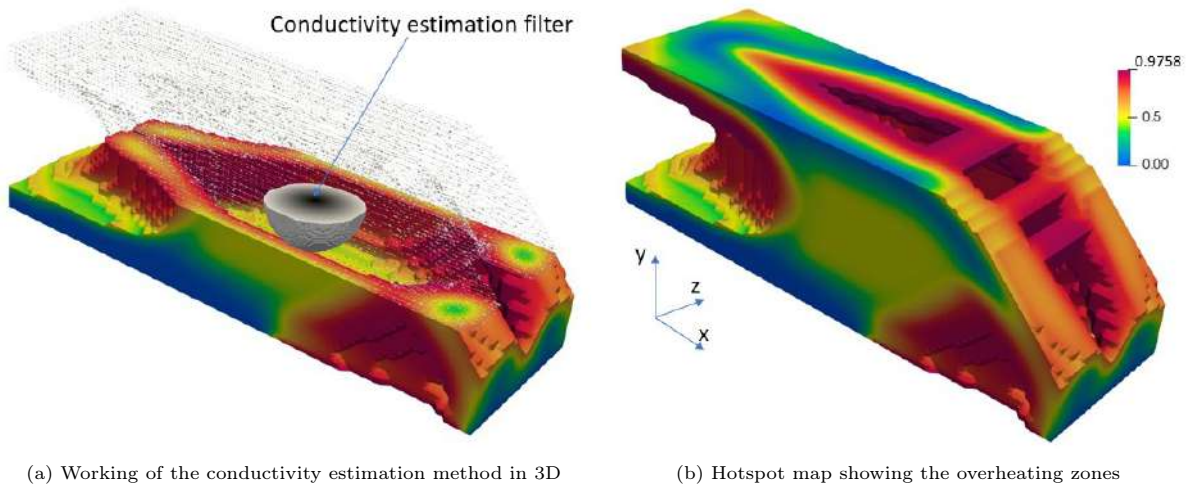


Figure 3.23: Hotspot map generated using the conductivity estimation method in 3D geometries

The same conductivity estimation method can be used as a constraint as done in Section 3.4 and combined with robust formulation discussed in Section 3.4.2. The implementation is pretty straightforward as only the domain changes from \mathbb{R}^2 to \mathbb{R}^3 . The conductivity estimation method is used as a constraint on the compliance minimization TO problem as was done in 2D. The 3D TO code from Liu et al. [25] along with the Robust TO code from Wang et al. [46] was used in addition to the conductivity estimation hotspot constraint for the evaluation of the designs. The boundary conditions and loading of the cantilever beam are given in Figure 3.22. Again, the constraint is applied to the eroded design as it has the least volume among the three designs and will therefore give the worst case of overheating. The critical temperature value was set to $T_{cr} = 0.8$ and two different volume fractions $vf = 0.3$ and $vf = 0.5$ were tested and compared against the TO design without the hotspot constraint. The rest of the Robust TO parameters are similar to the one used in Table 3.3.

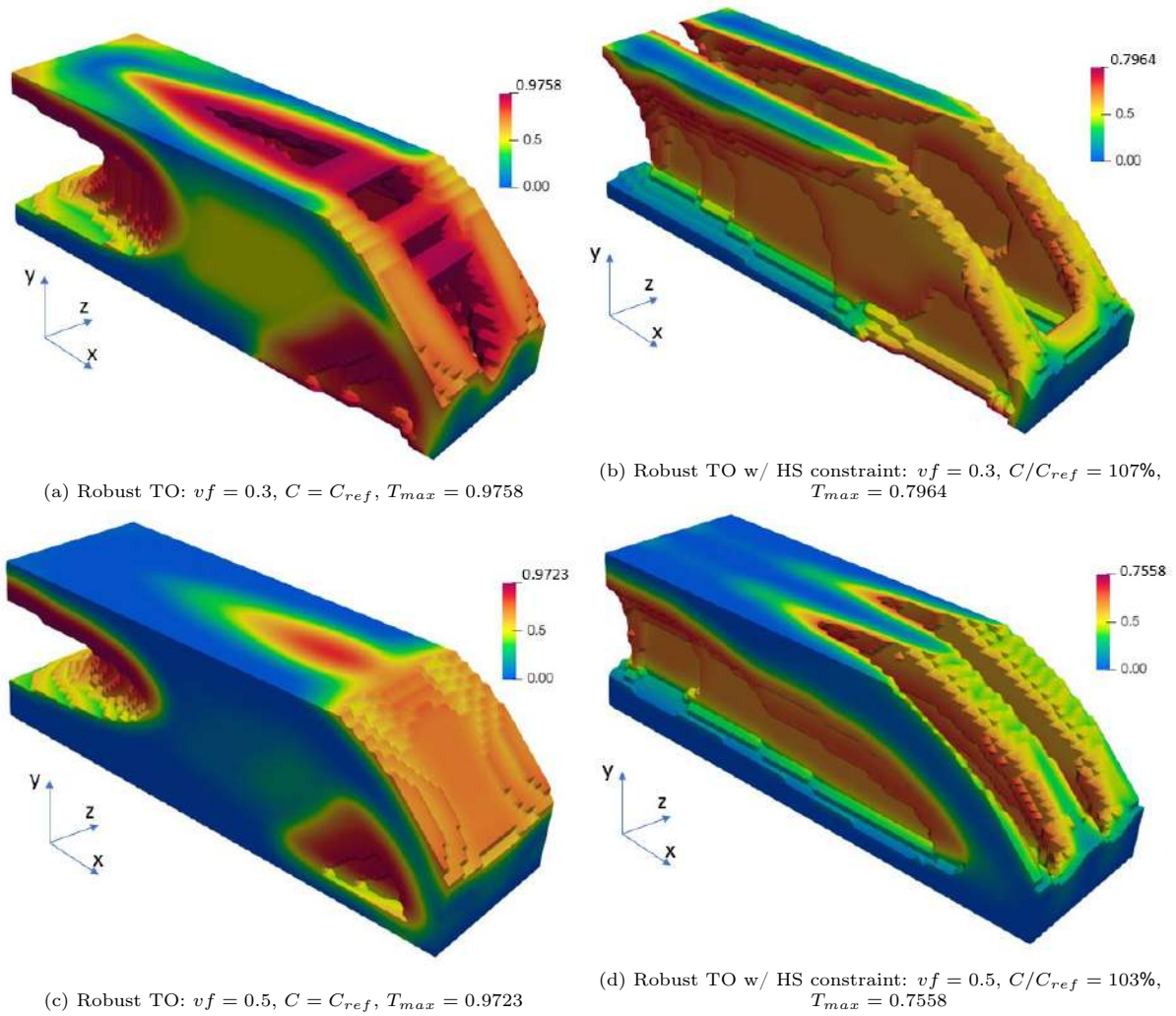


Figure 3.24: Comparison of hotspot map of regular robust TO on the left and robust TO with hotspot constraint on the right for two different volume fractions

The hotspot map results from the 3D Robust TO with conductivity estimation hotspot constraint is shown in Figure 3.24. Both the designs satisfy the hotspot constraint as indicated by the maximum temperature in the plot. Figures 3.24a and 3.24b show the hotspot map of Robust TO without and with the hotspot constraint for the volume fraction of 0.3. It can be seen that the maximum temperature in the design with hotspot constraint $T_{max} = 0.79$ is far less than the regular design $T_{max} = 0.98$. Similar is the case for the volume fraction of 0.5, the one with the hotspot constraint 3.24d is far superior in avoiding local overheating than the regular design in 3.24c. This is because the conductivity estimation hotspot constraint is redistributing material such that the degree of overhang is reduced which is the major cause of inducing heat accumulation. The cross-sectional view of the designs in order to limit local overheating. The sectional views of the designs in Figure 3.24 are given in Figure 3.25. Two section views have been taken, Figures 4.6a to 4.6d show the cross-section along the xy plane viewed from the z axis called S1. Figures 4.6e to 4.6h have a cross-section taken along the yz plane and viewed from the x axis called S2. The respective design (with/ without hotspot constraint) and volume fraction are mentioned in the subcaption. The designs without the hotspot constraint show severe cases of overheating along the long overhangs present. This has been completely eliminated in the designs with the hotspot constraint as only short overhangs of a small degree exist that do not cause much overheating issues. Also, the tear-drop-shaped voids that were seen in the 2D designs reappear in the 3D formulation as seen in Figures 4.6f and 4.6h. Also, there is not much increase in the compliance of the structure as the C/C_{ref} value is only 107% and 103% for volume fractions 0.3 and 0.5 respectively. Thus, the conductivity estimation hotspot proves

to be efficient in eliminating features that cause local overheating without compromising much on the compliance of the structure.

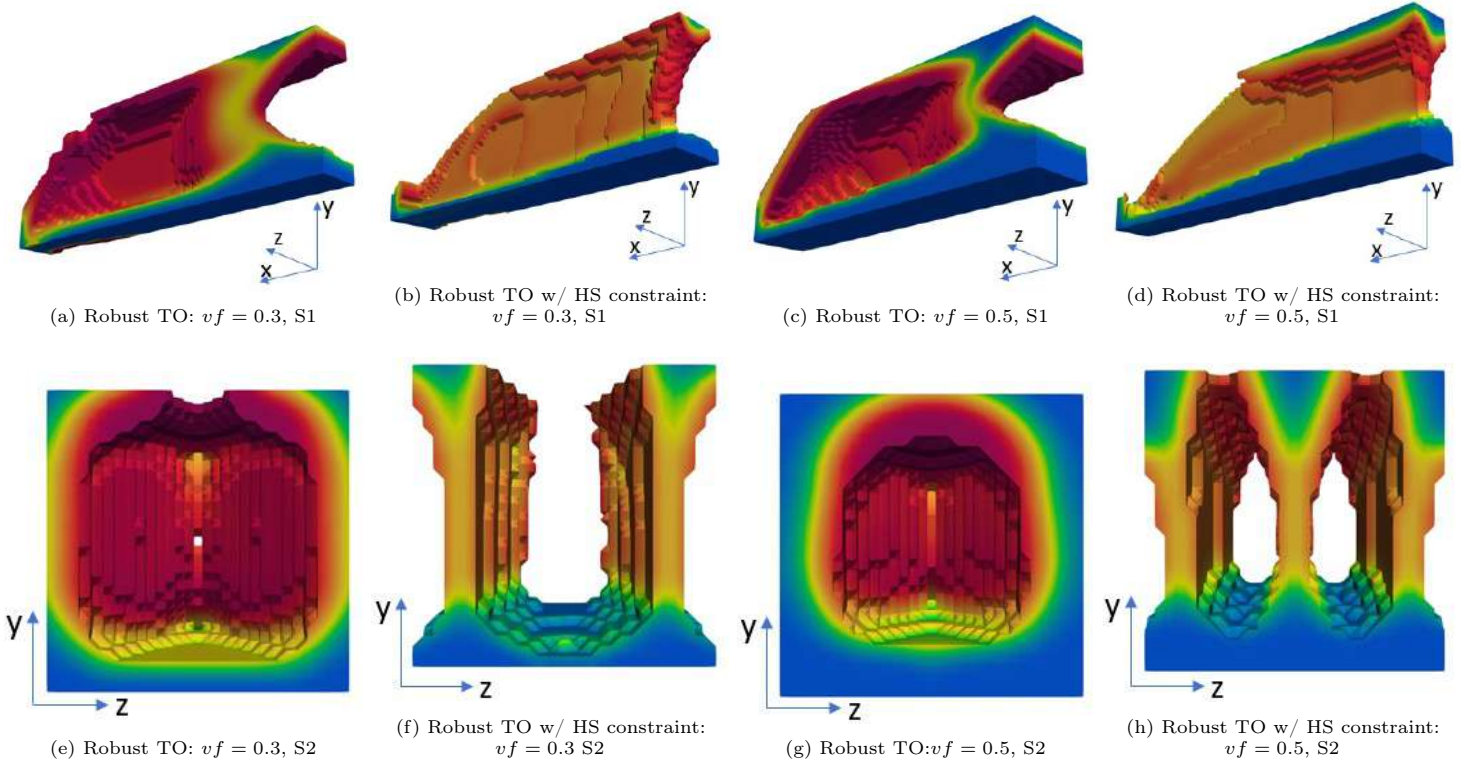


Figure 3.25: Section views of the designs obtained with and without the hotspot constraint

3.8. Conclusion

A novel geometric-based hotspot detection method and its integration with the TO problem to address the local overheating issue in AM is presented in this paper. The method uses a geometry-based filter called the conductivity estimation filter to capture the densities of the nearby elements that are within the thermal interaction length and compute a local conductivity for all the elements in the design domain. This local conductivity is then post-processed to generate the temperature field called the hotspot map. The elemental temperature will be high if the local conductivity of an element is low. This is an indication that there aren't enough material densities around to conduct heat and thus will pose a risk of local overheating. Since the conductivity estimation method uses a mesh-independent filter, it can be pre-computed and thus can be placed outside the TO iteration loop. This gives a huge computational advantage as compared to other hotspot detection methods available in the literature. Although a quantitative estimation of temperature cannot be obtained with this method, a comparison with the high-fidelity transient thermal simulation proved that the conductivity estimation method can detect critical overheating zones very efficiently. Thus, a qualitative estimation of the local overheating can be very easily obtained using this method.

To avoid the features that cause heat accumulation problems in the design phase itself, the conductivity estimation method was combined with TO. To achieve this, the conductivity estimation method was used as a constraint called the hotspot constraint in order to limit the maximum temperature generated in the design domain below a critical limit. A geometrical calibration was done to determine the critical overhang angle for a given critical temperature value based on the feature size. The constraint was made in such a way that it remained active at all the overhang regions, i.e., when there was a void below a solid element, and could be satisfied easily everywhere else. This resulted in the constraint forcing the optimizer to modify the design variables below the solid element in overhang regions and increase their densities in order to reduce the degree of overhang. Finally, robust TO formulation was used to avoid intermediate densities in the design and to have a length-scale control over the feature

size. The constraint doesn't restrict the design to have the same overhang angle everywhere like the overhang filter by Langelaar et al. [20] which could reduce the design freedom. Instead, it redistributes material everywhere such that there is a lower bound on the local volume of solids. This creates an efficient pathway for the heat to conduct and thus minimize the risk of local overheating. The designs obtained using the hotspot constraint with robust TO proved to be far superior in avoiding local overheating when analyzed with a transient thermal simulation and compared against standard TO designs. However, a framework for determining conductivity filter size for a given set of material and process parameters must be developed in addition to the existing calibration used in this paper to tailor-make optimized design for a given process and material properties. Along with this, a huge computational gain is obtained for finer resolutions when using the conductivity estimation hotspot constraint. This is because the arrays of the sensitivities and filters can be pre-computed and less no. of PDE equations are solved.

Finally, it was demonstrated here that extending the hotspot constraint to a 3D environment is fairly simple. The same 2D formulation can be used with a slight modification in the shape of the conductivity estimation filter to incorporate it in 3D. The drop in stiffness values of the structure is even less in 3D than it was in 2D, which means designs free from local overheating can be obtained without compromising on the structural integrity. Currently, the conductivity estimation method can only be used for planar layers. The next step would be to incorporate the fabrication sequence with complex material deposition as in curved layers.

4

Integration with Space-time Topology Optimization

4.1. Introduction to space-time topology optimization

4.1.1. Background

The structure is fabricated by adding material in an incremental way layer-by-layer in additive manufacturing. Very often, the fabrication sequence is determined after the structure is designed and optimized. In typical AM processes such as powder bed fusion, fused deposition modeling, and selective laser sintering, the optimized structure is sliced into layers and manufactured at a particular orientation depending upon overhangs and other constraints. The printer head or the base in which the part is manufactured has three translational degrees of freedom which helps in manufacturing the part. Recent developments in the methods used for additive manufacturing like the introduction of rotational degrees of freedom have significantly improved manufacturing flexibility. One such example is the method called wire-arc additive manufacturing (WAAM) where a robot-assisted arm is used, which can deposit material in curved layers. This additional flexibility in fabrication makes the planning of the fabrication sequence more important and widens up the design space. As mentioned earlier, the structural optimization and planning of the fabrication sequence happen subsequently, which means the optimizer is only concerned with the performance of the final structure and has nothing to do with the intermediate structures formed during fabrication. This is mostly the case if we are considering the fabrication of small structures. But for large-scale structures, the self-weight, material curing and solidification, thermal dissipation, and distortion become significant and are dependent upon the fabrication sequence. If neglected during the design phase may cause serious problems during manufacturing.

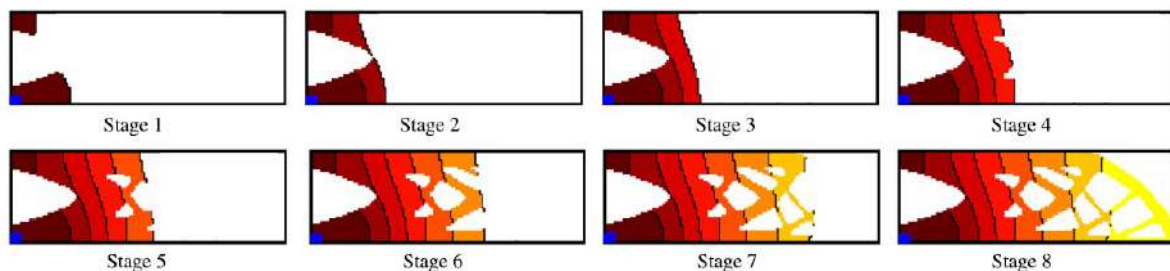


Figure 4.1: A sequence of intermediate structures corresponding to the optimized structure in Stage 8 from [48]

To incorporate the fabrication sequence-dependent parameters into the design, a method has been developed called space-time topology optimization by Wang et al. [48] which concurrently optimizes the structural layout as well as the corresponding fabrication sequence as shown in Figure 4.1. The space-time topology optimization uses two sets of design variables- the density field and the time field. The

density field determines the structural layout which is a standard density-based approach. The fabrication sequence is determined by the second design variable, which is the time field is monotonously increasing which indicates the incremental addition of material. The objective function takes into consideration the mechanical properties such as compliance of the final structure as well the intermediate structure. To this end, a sequence of intermediate structures is defined by the density and the time field. General constraints on intermediate structures, regarding fabrication continuity and process speed, are imposed. This general formulation is demonstrated by integrating a few simplified yet meaningful aspects that are associated with the fabrication sequence, including the self-weight of the intermediate structures, process-dependent loads, and time-dependent mechanical properties.

4.1.2. Space-time topology optimization

In the previous section 4.1.1, an overview of the space-time topology optimization [48] is presented. A short description of the design variables, objective function, constraints, and sensitivities used in the method are given. In space-time topology optimization two design variables are used i.e. the density field and the time field to describe the structural layout and fabrication sequence respectively. The density field (ρ) is known from traditional topology optimization methods as the design parameter which is updated to get the optimized structural layout. The time field (t) is now introduced to encode the order of material deposition. The objective function (J) is defined as a function of density and time field given by,

$$J(\rho, t) = J_{complete}(\rho, t) + J_{process}(\rho, t), \quad (4.1)$$

where, the first term ($J_{complete}$) measures the structural property such as compliance of the whole structure, and the second term ($J_{process}$) calculates properties of the intermediate structures generated during the fabrication process.

4.1.3. Intermediate structures

The design space is discretized and each element is associated with a (pseudo) density value $\rho_e \in [0,1]$ and a (pseudo) time value $t_e \in [0,1]$. The element density value converges either to 0 or 1 indicating whether the element is empty or solid respectively. The time value is continuous and indicates the time at which the material is added to the structure. A higher time value indicates the element is fabricated later. As mentioned earlier, the structural properties of intermediate structures are also computed. In space-time topology optimization, the element with a time value $t_e \leq T$, where intermediate structure at a specific time T is determined by,

$$\rho_e^{[T]} = \begin{cases} \rho_e, & \text{if } t_e \leq T, \\ 0, & \text{otherwise} \end{cases} \quad (4.2)$$

The conditional equations are non-differentiable and hence filtering and projection methods are used to generate the intermediate structure from density and time field. Two sets of design variables, ϕ , and τ for density and time respectively. Convolution operators are used for smoothening both the field and avoiding checkerboard patterns. The smoothed continuous fields are given by $\tilde{\phi}$, and $\tilde{\tau}$. The convolution operator in classical density-based approaches for smoothening yields,

$$\tilde{\phi}_e = \frac{\sum_{i \in S_e} w(\mathbf{x}_i, r_d) v_i \phi_i}{\sum_{i \in S} w(\mathbf{x}_i, r_d) v_i} \quad (4.3)$$

$$\tilde{\tau}_e = \frac{\sum_{i \in S_e} w(\mathbf{x}_i, r_t) v_i \tau_i}{\sum_{i \in S} w(\mathbf{x}_i, r_t) v_i} \quad (4.4)$$

where v_i is the area or volume of an element, and weighting function w is defined as

$$w(x_i, r) = r - \|\mathbf{x}_i - \mathbf{x}_e\| \quad (4.5)$$

where r is the filter radius, \mathbf{x}_e and \mathbf{x}_i are the centroid of element e and its neighboring element $i \in S_e = \{i | w(\mathbf{x}_i, r) > 0\}$, respectively. Here, r_d and r_t can take different values. The smoothed fields

are then projected into discrete density and time values using a Heavyside projection. The projection converts a density value $\rho = \bar{\phi}$ greater than a threshold to close to 1 or a smaller value close to 0.

$$\rho_e = \bar{\phi}_e = \frac{\tanh(\beta_d \eta) + \tanh(\beta_d(\bar{\phi}_e - \eta))}{\tanh(\beta_d \eta) + \tanh(\beta_d(1 - \eta))} \quad (4.6)$$

where β_d is a positive number to control the sharpness of the step function, and η is the density threshold.

Similarly, for the time field, the projection converts a time value $\bar{t}_e^{[T]} = \bar{\tau}_e$ smaller than a given threshold T to close to 1 or a larger value close to 0.

$$\bar{t}_e = \bar{\tau}_e = 1 - \frac{\tanh(\beta_t T) + \tanh(\beta_t(\bar{\tau}_e - T))}{\tanh(\beta_t T) + \tanh(\beta_t(1 - T))} \quad (4.7)$$

where β_t is a positive number to control the sharpness of the step function, and T is the time value threshold.

The intermediate structure is the product of these two projections at time T and is given by,

$$\rho_e^{[T]} = \rho_e \bar{t}_e^{[T]} \quad (4.8)$$

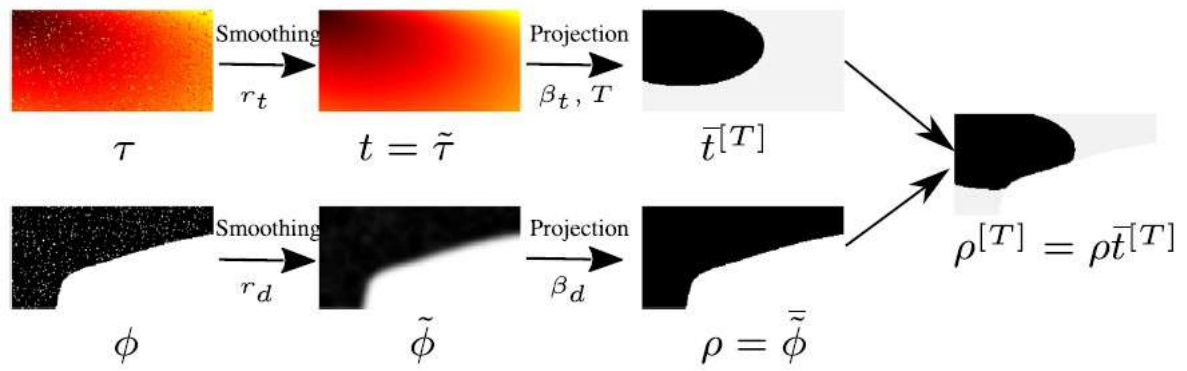


Figure 4.2: Illustration of the density field (bottom), the time field (top), and the corresponding filtering and projection operations for specifying an intermediate structure (right) from [48]

4.1.4. Volume and continuity constraints on intermediate structures

The fabrication speed determines the amount of material that can be deposited per unit of time. To incorporate the fabrication speed in space-time topology optimization the time range $[0,1]$ is divided by a finite number $(N+1)$ of uniformly distributed time points given by,

$$T_i = \frac{i}{N}, \quad i = 0, \dots, N \quad (4.9)$$

where N is the intervals or number of stages in the fabrication process, each with a duration of $\frac{1}{N}$. The fabrication speed is assumed to be constant and the maximum volume of the structure V_0 is equally divided during each of the uniform time intervals. The increment in volume between time points T_i and T_{i-1} is bounded by $\frac{V_0}{N}$. The optimization uses the maximum amount of material volume available. The volume constraint is thus given by,

$$V^{[T_i]} \leq \frac{i}{N} V_0, \quad i = 1, \dots, N \quad (4.10)$$

where $V^{[T_i]}$ is given by

$$V^{[T_i]} = \sum_e \rho_e^{[T_i]} v_e, \quad i = 1, \dots, N \quad (4.11)$$

where v_e is the area or volume of an element.

To avoid the use of support structures in the design, a continuity constraint is formulated to prevent isolated material patches. An isolated material patch is formed when there is a local minimum in the time field i.e. all its adjacent elements have a larger time value and thus it is fabricated later. To prevent this the continuity constraint is given as,

$$g(t_e) = \min_{i \in N_e} (t_i) - t_e \leq 0, \quad \forall e \in M \quad (4.12)$$

where N_e indicates the set of elements adjacent to element e . M is the set of all active elements in the design domain except those prescribed at the start at $t_e = 0$. The continuity constraint is non-differentiable and thus is approximated using a step function. For derivation ref..

4.2. Hotspot detection in STTO designs using conductivity estimation method

The designs made using space-time topology optimization are susceptible to overheating just like the regular TO designs. Currently, there is no method that can detect overheating in designs which includes a fabrication sequence for manufacturing. The slab analysis method given by Ranjan et al. [32] is difficult to implement because the layers can be curved instead of just being planar and doing a slab analysis on a curved layer could get demanding. This is because the time field design variable that controls the fabrication sequence needs to be taken care of as well. However, by doing some modifications to Eqn 3.19 to incorporate the time design variable, the conductivity estimation method can be used to detect hotspots in the STTO designs as well.

In the earlier formulation, the conductivity estimation method was used on designs made by planar layer-by-layer deposition. The build-direction would remain constant and the conductivity filter would orient itself to capture the densities of already printed features. Thus, the semicircular shape of the filter. However, in STTO the layers printed are not planar and change directions over the entire design domain based on the fabrication sequence. The fabrication sequence is defined by a continuous-time field as shown in Figure 4.2. Thus, for a given element whose local conductivity is to be evaluated only the elements that have a time value less than the central element's time value should be considered. This is because only these elements are printed at that time instant and only they will contribute towards heat conduction. Also, the conductivity estimation filter should be able to orient its axis perpendicular to the direction of the isoline in order to follow the curved layers. The conductivity estimation method should satisfy these functional requirements in order to be useful for detecting local overheating in STTO designs.

4.2.1. Modifications to conductivity estimation filter to incorporate with STTO

The conductivity estimation method uses the density field ρ and the time field before projection $\tilde{\tau}$ to calculate the local conductivity of each element. For detecting hotspots in STTO using the conductivity estimation method, a complete circular domain S_e is used for the conductivity filter. Then, a smooth selection method is used to determine which elements will be used for the calculation of the local conductivity. For this, a Sigmoid projection method is used with the time point $\tilde{\tau}$ of the central element as the threshold value $\gamma_e = \tilde{\tau}_e$ as given in Eqn 4.13. This Sigmoid projection is used inside the conductivity filter to project the elements that have a lower time point ($\tilde{\tau}_j < \gamma_e$) than the threshold to values close to 1 i.e. these elements are already printed. The elements that have higher time points than the threshold will be projected to 0 since they are not yet printed and would not contribute towards the heat conduction of the central element. The projection of time value is given by:

$$\bar{\lambda}_j = \frac{1}{1 + e^{\zeta(\tilde{\tau}_j - \gamma_e)}} \quad j \in S_e \quad (4.13)$$

where $\tilde{\tau}_j$ is the smoothed time points of elements inside the filter domain S_e , ζ is the projection sharpness that is kept at a very high value, and S_e is the circular domain of the filter. A schematic of

the working of the Heaviside projection for smooth selection of elements contributing to the calculation of the local conductivity is given in Figure 4.3.

These projected time values λ act as a weight factor, i.e., when they are multiplied with their corresponding densities ρ , only the elements that have the projected time value $\bar{\lambda} > 0$ will have their densities counted for the calculation of local conductivity. Finally, the densities and time value product will be multiplied with the radial weight factor w to consider the decreasing influence of the elements as they go further away from the central element. The modified local conductivity $\bar{\kappa}_e$ is given by:

$$\bar{\kappa}_e = \frac{\sum_{j \in S_e} \rho_j w_j \bar{\lambda}_j}{\sum_{j \in S_e} w_j \bar{\lambda}_j} \quad (4.14)$$

$$\tilde{\mathbf{T}} = (1 - \bar{\kappa})\rho \quad (4.15)$$

here, S_e represents the set of elements in the vicinity of element e defined as $|x_e - x_j| < r$ and $|y_e - y_j| < r$, $\tilde{\mathbf{T}}$ is the domain temperature used for generating the hotspot map. The schematic of the conductivity filter is shown in Figure 4.3.

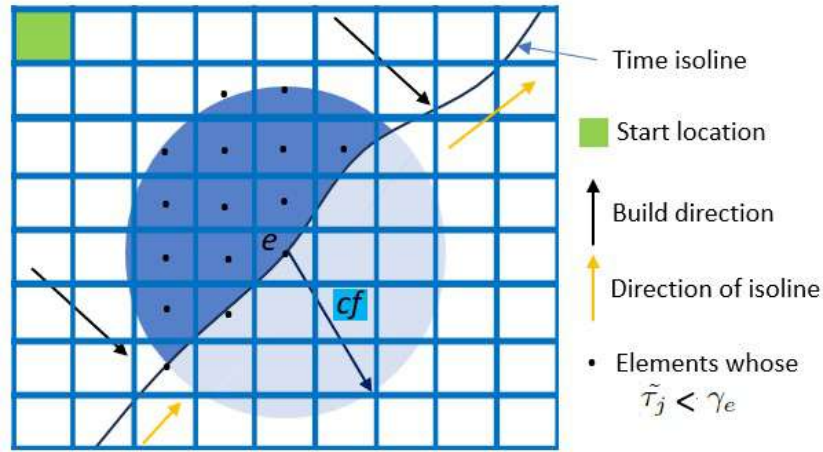


Figure 4.3: Schematic of the working of the Sigmoid projection for the selection of elements whose densities would be taken for evaluating local conductivity.

The conductivity estimation filter is used on the design generated using space-time topology optimization as shown in Figure 4.4. The green box in Figure 4.4a represents the initialization of the time field or in simple terms, the starting point of the fabrication. The black curved lines show the number of stages in the design. Here, the design is realized in 8 stages. The conductivity estimation filter is added to the final geometry that is obtained. The conductivity estimation filter moves through each element in the design domain and using the design field and time field, determines the element densities that will be contributing towards the heat evacuation. The red regions indicate a higher temperature in the design domain. The working of the conductivity estimation filter is given in Figure 4.4a. It appears as it does due to the time field and time value of the central element in consideration and also because of the radial penalization used. The darker shade shows which element densities will have a higher influence on the calculation of the local conductivity. Since very few element densities are available (overhang region), the local conductivity $\bar{\kappa}_e$ given by Eqn 4.16 is very low, and the temperature value according to Eqn 4.15 is very high. This is the same for all the elements in that overhang region and thus the temperature value in that region is very high as shown in Figure 4.4b. Also, in the thin feature region, the temperature goes very high as there is very little material to conduct heat. Thus, the conductivity estimation method is efficient in detecting local overheating regions in designs that include fabrication sequences. Also, it is evident that local overheating exists in designs made by STTO as a higher degree of overhangs and thin features are included in the designs.

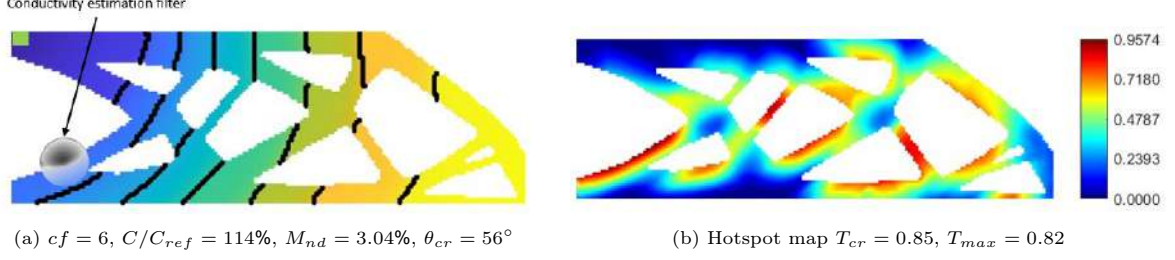


Figure 4.4: Robust TO designs using different conductivity filter size figures 3.17a, 3.17c and 3.17e. Corresponding hotspot maps with maximum temperature figures 3.17b, 3.17d and 3.17f

4.3. Influence of both fabrication sequence and structural layout to limit the heat accumulation

In space-time topology optimization, just like the robust TO, we can use the conductivity estimation method as a hotspot constraint to limit local overheating in the designs. For this, we optimize both the structural layout as well as the fabrication sequence as opposed to robust TO where we only optimized the structural layout. We use the general formulation of the hotspot constraint presented in Section 3.4 and modify it in order to incorporate the time design variable. Recall that, we used a conductivity penalization and an interpolation factor to make the constraint active near the overhangs. Thus, the local conductivity given in Eqn 4.16 is modified by penalizing the densities in it by a conductivity penalization factor q similar to that in Eqn 3.19. The equation of the penalized local conductivity $\bar{\psi}_e$ and elemental temperature ω_e for STTO is given by:

$$\bar{\psi}_e = \frac{\sum_{j \in S_e} \rho_j^q w_j \bar{\lambda}_j}{\sum_{j \in S_e} w_j \bar{\lambda}_j} \quad (4.16)$$

$$\omega_e = (1 - \bar{\psi}_e) \quad (4.17)$$

here, S_e represents the set of elements in the vicinity of element e defined as $|x_e - x_j| < r$ and $|y_e - y_j| < r$.

The maximum elemental temperature should be less than a critical temperature which is made computationally efficient by saying that, the maximum temperature of the design domain Ω should be less than a critical temperature value T_{cr} . The equation is given as:

$$\max(\bar{\omega}^\Omega \epsilon) \leq T_{cr} \quad (4.18)$$

where $\epsilon = \rho^r$ is the interpolation factor used and r is the interpolation exponent. Since the max function is non-differentiable, a P-mean aggregate is taken to find the maximum temperature of the design domain in a smooth manner. Applying P-mean and scaling factor α the hotspot constraint for STTO is given as:

$$g = \frac{\alpha}{T_{cr}} \left[\frac{1}{n} \sum_e (\omega_e \epsilon_e)^P \right]^{1/P} - 1 \leq 0 \quad (4.19)$$

$$g = \frac{\alpha}{T_{cr}} \left[\frac{1}{n} \sum_e ((1 - \bar{\psi}_e) \rho_e^r)^P \right]^{1/P} - 1 \leq 0 \quad (4.20)$$

4.3.1. STTO problem formulation

As STTO uses the Heaviside projection filter to get black-and-white designs, a robust formulation is not introduced in the formulation. The implications of not having a length-scale control haven't been studied for this formulation. The same half MBB beam with boundary conditions given in Figure 3.6 is used with 180×60 elements as a design domain. The problem of compliance minimization of the whole structure as well as the intermediate structure under the assumption of linear elasticity is used for

optimization. The intermediate structure is loaded by self-weight. The global volume constraint, volume constraint on intermediate structures, and continuity constraint given in Section 4.1.4 are used along with the hotspot constraint described in Section 4.1.4. The number of stages N in which the structure is realized is predetermined. The optimization problem for the space-time topology optimization with the conductivity estimation hotspot constraint is given by,

$$\min_{\phi, \tau} = \mathbf{U}^T \mathbf{K}(\rho) \mathbf{U} + \sum_{i=1}^N \alpha_i (\mathbf{U}^{[T_i]})^T \mathbf{K}(\rho^{[T_i]}) \mathbf{U}^{[T_i]} \quad (4.21)$$

$$\text{s.t. } \mathbf{K}(\rho) \mathbf{U} = \mathbf{F} \quad (4.22)$$

$$\mathbf{K}(\rho^{[T_i]}) \mathbf{U}^{[T_i]} = \mathbf{G}(\rho^{[T_i]}), \quad i = 1, 2, \dots, N \quad (4.23)$$

$$0 \leq \phi_e \leq 1 \quad (4.24)$$

$$0 \leq \tau_e \leq 1 \quad (4.25)$$

$$V^{[T_i]} = \sum_e \rho_e^{[T_i]} v_e, \quad i = 1, \dots, N \quad (4.26)$$

$$\frac{1}{\#M} \sum_{e \in M} H(g(t_e)) < \epsilon \quad (4.27)$$

$$\frac{\alpha}{T_{cr}} \left[\frac{1}{n} \sum_e ((1 - \bar{\psi}_e) \rho_e^r)^P \right]^{1/P} - \leq 0 \quad (4.28)$$

where \mathbf{U} is the displacement vector, and \mathbf{F} is the force vector. The first term in the objective function is the compliance of the whole structure and the second term is the compliance of the intermediate structure. The global stiffness matrix \mathbf{K} is assembled from element stiffness matrices given by $\mathbf{k}_e = E_e(\rho_e) \mathbf{k}_0$, where \mathbf{k}_0 is the stiffness of a solid element with unit Young's Modulus and $E_e(\rho_e)$ is the Young's Modulus of an element e , interpolated from the solid isotropic material with penalization (SIMP), given by

$$E_e(\rho_e) = E_{min} + \rho_e^q (E_0 - E_{min}) \quad (4.29)$$

where E_0 is the Young's Modulus of a solid element, E_{min} to prevent \mathbf{K} from becoming singular, and q is the penalization factor taken from standard density-based topology optimization method. $\mathbf{K}(\rho^{[T_i]})$, $\mathbf{U}^{[T_i]}$, and $\mathbf{G}(\rho^{[T_i]})$ are the stiffness matrix, displacement vector and gravity load of intermediate structures respectively at time T_i . α_i is the weighting factor for the influence of the gravity load. Finite element analysis is performed for each intermediate and final structure.

4.4. Results for different fabrication sequences

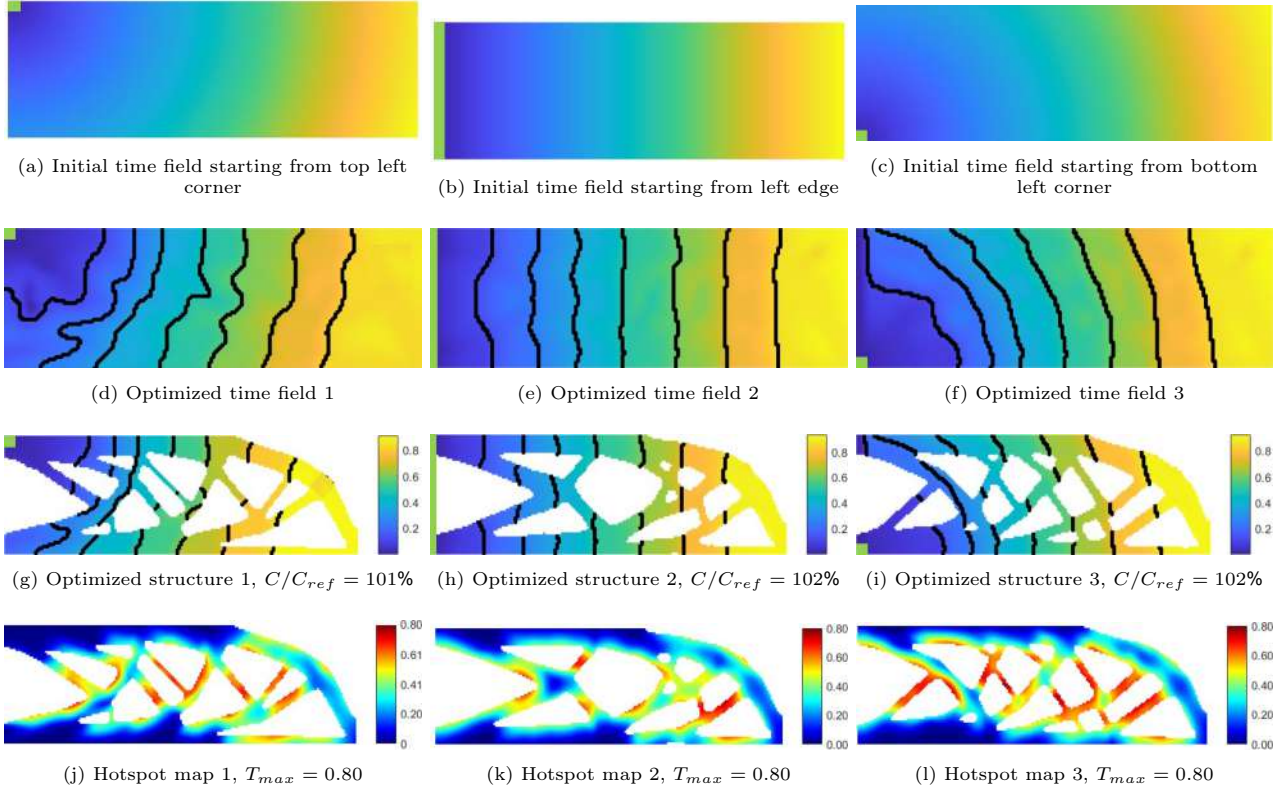


Figure 4.5: Time fields and structures produced with various manufacturing start points (green boxes). The initial time fields, optimized time fields, optimized structures, and corresponding hotspot maps are listed from top to bottom. The initial time fields are created using distance data that correlate to the startpoints. The boundaries between neighboring pieces that have been produced at various stages of manufacturing are shown by the black curves. In this test, there are 8 steps, which is a specified number rather than a design variable. As a result, T_i , the values that are utilized to divide the time field into segments are derived during optimization.

The optimized time and density fields for three different manufacturing start points (indicated by green boxes) and their respective hotspot maps are shown in Figure 4.5. A critical temperature value of $T_{cr} = 0.8$ was used for all these designs. The original time fields are displayed in the first row *figures 4.5a to 4.5c*. The initialization process involves calculating the distance between each element and the start region. The maximum distance value between all items is then used to normalize the distance field. The target volume fraction of 0.5 is used to uniformly initialize the density field while a monotonic field is used to initialize the time field. The density projection β_d is doubled after every 50 iterations to a maximum of 128 and time projection β_t is incremented by 5 after every 30 iterations to a maximum of 50. The second row displays the continuous time fields that have been optimized *figures 4.5d to 4.5f*, with the curves indicating the edges of the various production phases (in this case, there are a total of eight). The optimal structures, displayed in the third row *figures 4.5g to 4.5i*, are colored based on the time fields. Note that, for regular STTO designs without the hotspot constraint, the time field exerts minimal influence on the objective function and it only affects the segmentation of the structures into stages. Thus, the designs look very similar to each other even for different time fields as given by Wang et al. [48]. However, as the hotspot constraint uses the time field to determine the conductivity filter, the optimized structures are very different as shown in *figures 4.5g and 4.5h*. The compliance values are only 1% to 2% higher than the reference design as shown in Figure 4.4a, for time fields 1 and 2 respectively.

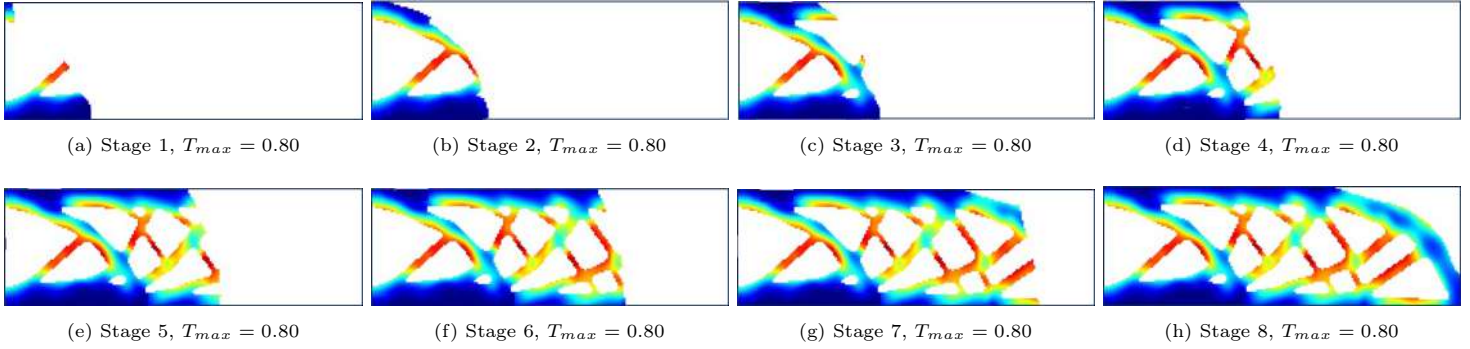


Figure 4.6: Evolution of the hotspot map in each intermediate stage of manufacturing for time field 3

The last row shows the hotspot map *figures 4.5j to 4.5l* for the three different time fields. All these designs are below the critical temperature limit of 0.8. The time and density design variable in the hotspot constraint plays a significant role in modifying the time field and density field to limit local overheating. The constraint forces the optimizer to redistribute the material such that the structural layout and fabrication sequence are simultaneously optimized to prevent local overheating. The time field isolines that determine the fabrication sequence are oriented such that there is sufficient material before the next layer for efficient heat evacuation. Again, the hotspot constraint is trying to shorten the length of overhangs which are the major cause of local overheating, by adding material underneath them. This way the current layer deposited has sufficient material underneath it to efficiently conduct heat and lower the temperature in the region. It can be seen how the time fields affect the features that are formed. For time field 1, the features are more directed toward the leftmost top corner as that is where the starting point is. For the time field 2 design, the features are more directed towards the left edge. Since the baseplate is also towards the left edge for these fabrication sequences, the heat flow to the baseplate would be faster and the risk of local overheating is reduced. However, since there is no length-scale control in the design, there are some thin features existing in the design. Although, they do not show a high temperature as they have sufficient material around them to conduct heat as encapsulated by the conductivity filter. Thus, the use of both density and time fields increases the design freedom. An illustration of the temperature field in different stages during the additive manufacturing process for time field 1 is shown in Figure 4.6. It is noticeable that the optimized fields satisfy the volume, continuity, and hotspot constraints.

Discussion and Recommendations

5.1. Shortcomings of the conductivity estimation method in detecting hotspots

The conductivity estimation method largely depends on the conductivity filter size for calculating the local conductivity of elements. The size of the conductivity filter determines how many solid elements or features will contribute to the conductivity of that central element. The thermal interaction length given in Section 3.2.3 is used to determine the conductivity filter size as elements that are within this length are prominent in heat conduction. However, it may happen that the conductivity estimation filter captures features that do not actually contribute toward heat conduction. This may happen due to the features not being connected directly to the central element where the local conductivity is being examined. As these features are separate from the central element, in actual cases they will not be able to contribute to heat conduction due to the void in between them and there will be a risk of local overheating due to the rise in temperature. However, since the conductivity estimation filter does not check whether a feature is connected or not to the central element it will include those isolated features for the calculation of the local conductivity. Thus, the conductivity estimation method will overestimate the conductivity within the filter domain and will show a lower temperature which is an incorrect estimation of local overheating.

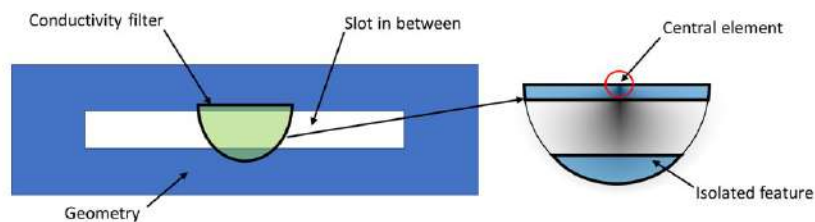


Figure 5.1: Schematic of the working of the Heaviside projection for the selection of elements whose densities would be taken for evaluating local conductivity.

An example of where the conductivity estimation method will fail to give a proper estimate of the local overheating is given in Figure 5.1. Here, a rectangular geometry with a slot in between is given and the conductivity estimation method is applied for the analysis of the hotspot map. An example of the conductivity filter used on the overhang is shown in the figure. The conductivity filter will take the densities of all the solid elements and evaluate the local conductivity of the central element. However as illustrated, the feature under the slot is isolated and not directly connected to the central element inside the filter domain. In reality, this feature under the slot will not contribute towards heat conduction and the feature above the void (overhang) will overheat a lot. There is no way the current approach could find whether there is a disconnection between the central element and other features. Thus, the conductivity estimation method considers all the features inside the conductivity filter and will result in

a lower temperature, defeating the purpose of detecting local overheating. This usually happens when the void sizes are smaller than the conductivity filter size. Therefore, for the correct estimation of local conductivity, it is necessary to eliminate these isolated features inside the conductivity filter domain.

5.1.1. Cluster operator

The problem stated above can be solved by having another filter that is a priori to the conductivity estimation filter which can eliminate any isolated features that are not directly connected to the source i.e. the central element. But this process has to be done smoothly in a continuous manner as it has to be differentiable when using it as a constraint in TO. This is the reason why simple image labeling cannot be used to eliminate the isolated features as the operation is discrete. Hence, a new filter called the cluster operator is introduced that has a filtering domain similar to the conductivity estimation method and can eliminate the isolated features in a continuous manner.

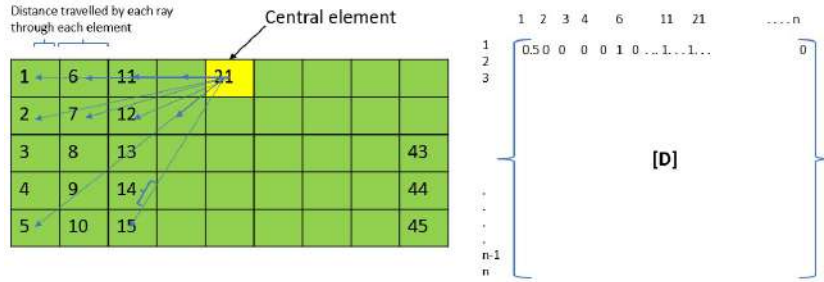


Figure 5.2: Schematic of the working of the Heaviside projection for the selection of elements whose densities would be taken for evaluating local conductivity.

The working of the cluster operator is shown in Figure 5.2. Here, a rectangular filter domain is chosen instead of a semicircular one for explanation. The original cluster method uses a semicircular filter domain. The cluster operator consists of a $n \times n$ distance matrix \mathbf{D} where n is the number of elements inside the conductivity filter. A ray that starts from the central element is pointed towards the center of each element in the filter domain as shown in the figure. It is clear that the rays targeted on each element will have some part in each and every element it passes through. The distance of how much the ray travels in an element is calculated and placed in the matrix \mathbf{D} . Note that, if a ray pointed to a certain element doesn't pass through a given element, its entry in the \mathbf{D} matrix will be zero. Thus, the matrix \mathbf{D} is populated by the entries of how much a ray passes through a given element. The matrix \mathbf{D} is then multiplied by an array of $n \times 1$ consisting of only ones. The product will give an array \mathbf{a} that has the distance traveled by each array from the central element to each element. The matrix \mathbf{D} is again multiplied by an $n \times 1$ array of all the densities inside the filter domain of the original geometry as \mathbf{b} . This array will also have the distances traveled by each array but now if there is a void in between the distance traveled by the ray the distance calculated will be less. The difference between arrays \mathbf{a} and \mathbf{b} is taken and is raised to a negative exponential \mathbf{C} whose equation resembles the bell curve as given in Eqn 5.1. The bell curve projects the elements whose distance in both arrays are same as 1 meaning the ray is unobstructed by a void. The elements that have a void in between will not have the same distance in arrays \mathbf{a} and \mathbf{b} and thus they will be projected to zero meaning they are not directly connected to the central element. The conductivity estimation method is then used over this filter that only takes into account the elements that are projected to 1. This way the features that are disconnected from the central element are eliminated and their contribution is not taken for the calculation of the local conductivity.

$$\mathbf{C} = e^{-(\mathbf{a}-\mathbf{b})^2} \quad (5.1)$$

$$\mathbf{a} = \mathbf{Dn} \quad (5.2)$$

$$\mathbf{b} = \mathbf{D}\boldsymbol{\rho} \quad (5.3)$$

where \mathbf{D} is the distance matrix, \mathbf{n} is an array of ones, and $\boldsymbol{\rho}$ is the density array of the elements inside the filter. The local conductivity will be calculated on the remaining solid elements with their respective radial and angular penalization w . The new conductivity estimation filter $\bar{\kappa}$ is given by:

$$\bar{\kappa}_i = \frac{\sum_{j \in N_e} e^{-(a_j - b_j)^2} w_j}{\sum_{j \in N_e} w_j} \quad (5.4)$$

The illustration of the working of the cluster operator in conductivity estimation is shown in Figure 5.2. The Figure 5.3a shown is the geometry encapsulated by the conductivity estimation i.e. it is within the thermal interaction length from the central element. Note that, even with the neighboring elements' penalization, the conductivity estimation still takes into consideration the contribution of those disconnected features. This will result in an underestimation of temperature at the central element. In order to get a correct estimation of conductivity, these isolated features are smoothly eliminated. Thus, only the densities of the features that are directly connected to the central element will be considered while calculating the local conductivity as shown in Figure 5.3b. As a result, a more accurate estimation of the local temperature can be obtained and the overheating risk detection becomes more conservative.

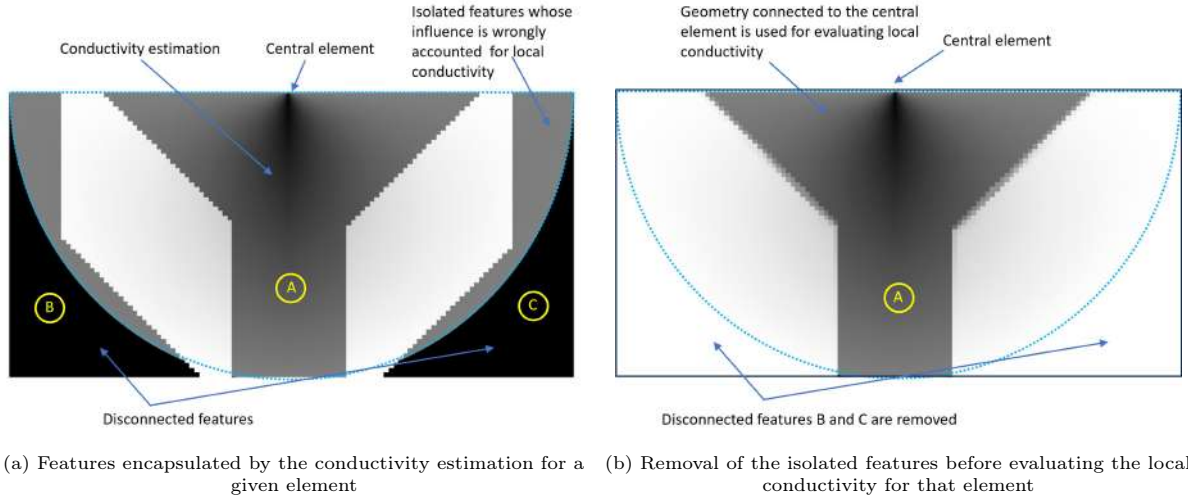


Figure 5.3: Illustration of the working of the cluster operator in conductivity estimation to remove isolated features for a given central element. 5.3a shows that the features 'B' and 'C' are not directly connected to the central element feature 'A'. The smooth elimination of those features using the cluster operator is shown in 5.3b.

5.1.2. Results

The conductivity estimation with and without the cluster operator is compared to find their efficacy in hotspot detection. The geometry used is the design obtained using an overhang filter by Langelaar et al. maxcitenames10 [19]. For reference, a high-fidelity LPBF transient thermal model is also done to investigate certain comparison metrics. Two comparison metrics are used, the Jaccard index to analyze the similarity between the hotspot maps generated. Secondly, the critical zone identification (CZI) map to examine the zones prone to local overheating. The Table 5.1 shows that the value of the Jaccard index for conductivity estimation with cluster operator $(\hat{T}_1, \hat{T}_3) = (\hat{T}_{ref}, \hat{T}_{clust}) = 38.36\%$ is better than without it $(\hat{T}_{ref}, \hat{T}_{cest}) = 32.22\%$. Furthermore, the presence of small voids beneath certain features, indicating regions of decreased conductivity, remained undetected in the absence of the cluster operator, as depicted in Figure 5.4d. These regions of low conductivity are clearly highlighted in the conductivity estimation with cluster operator as seen in Figure 5.4e. These results prove that hotspot detection has become more conservative (worst case of local overheating) when the conductivity estimation is used with the cluster operator. The CZI maps shown in Figure 5.4f also resonates with the transient simulation result more than when the cluster operator is not used.

Table 5.1: Jaccard index for different analysis

JI	Transient analysis
Conductivity estimation	$(\hat{T}_1, \hat{T}_2) = (\hat{T}_{ref}, \hat{T}_{cest}) = 32.22\%$
Conductivity estimation with cluster operator	$(\hat{T}_1, \hat{T}_3) = (\hat{T}_{ref}, \hat{T}_{clust}) = 38.36\%$

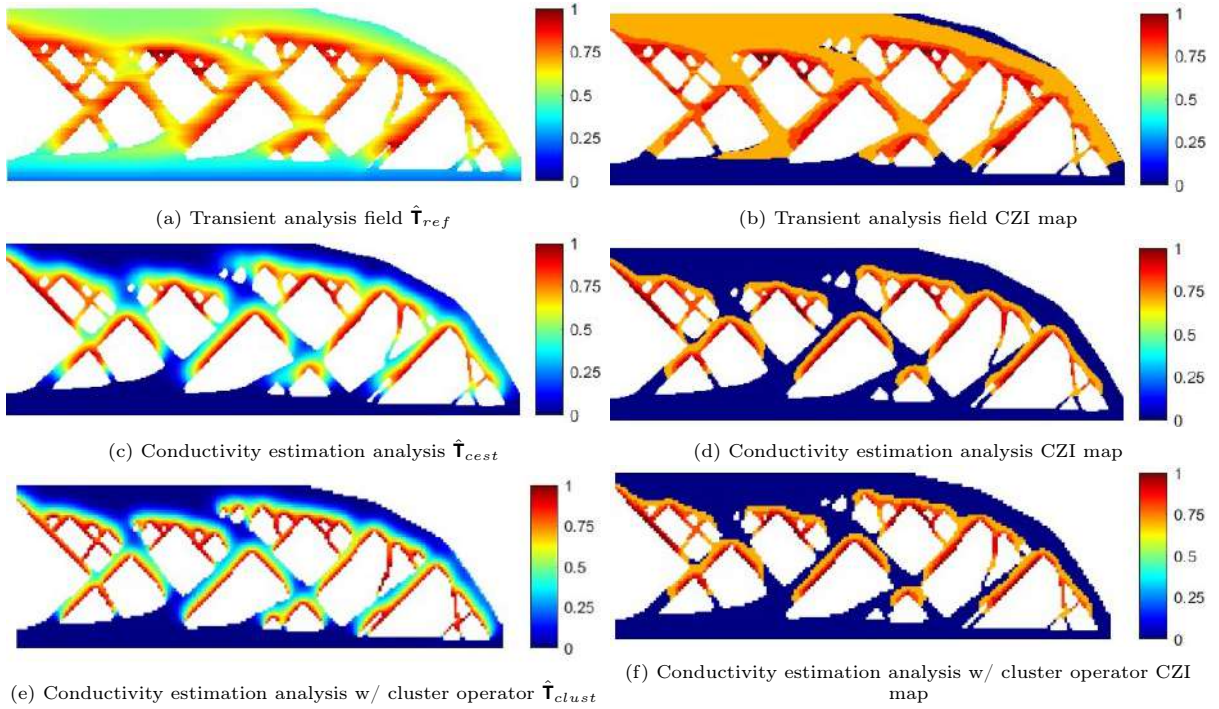


Figure 5.4: Normalized temperature field, i.e., the hotspot maps for different analyses are presented in Figures 3.5a, 3.5c and 3.5e and the corresponding CZI maps are presented in Figures 3.5b, 3.5d and 3.5f.

With the cluster method, the hotspot detection approach tends to err on the side of caution, identifying potential hotspots that might not necessarily lead to overheating but are treated as such to ensure safety. This approach aims to avoid false negatives (missing actual hotspots), even if it means labeling regions as hotspots that might not actually cause overheating in practice. In essence, it leans towards identifying worst-case scenarios to ensure robustness and prevent any potential issues.

5.2. Future scope

The cluster method explained in the previous section can be used as a constraint for TO. However, a major issue with using the conductivity estimation method with the cluster operator is that the cluster operator works properly when the densities are close to 1 and 0. If there are intermediate densities involved, the distances calculated from \mathbf{a} will be very different from that calculated in \mathbf{b} as the ρ will have densities that are less than one and when multiplied by \mathbf{D} will not give the correct length of the ray. One solution is to use some projection filtering method that will make the design more black and white and then the cluster operator can be used on this design. However, the issue of the conductivity estimation method calculating incorrect local conductivity when the void is smaller than the filter radius does not exist when it is used as a constraint for TO in Section 3.4.2. As explained in Section 3.5.3, the voids in the design go away if the filter size is reduced. Thus the topology is adjusted based on the size of the filter and how many elements it captures for calculating local conductivity. It would be interesting to see how the cluster operator in the conductivity estimation method as a hotspot constraint alters the structural layout.

A better understanding of the selection of conductivity estimation filter size is required as it has the most influence on the designs that are obtained. The thermal interaction length that determines the conductivity filter size can be obtained for different process parameters and materials in order to obtain better designs for preventing the risk of local overheating. Also, a deeper analysis of the AM transient thermal interaction can tell us the behavior of heat conduction within the thermal interaction length. In this paper, a linear weighting of the influence of neighboring elements is taken but this can change to a nonlinear weighting depending on the material properties and process parameters. Hence, it is important to fully understand the nature of conduction in transient simulation to properly approximate the influence of neighboring elements.

In Chapter 4 the working of the conductivity estimation hotspot constraint and its influence on the geometries obtained from STTO is given. However, a thorough understanding of the process parameters and different time fields needs to be studied in order to fully understand the influence of the hotspot constraint. Also, the robot load which is another feature of the STTO design can be used along with the hotspot constraint. Finally, this hotspot constraint can be extended to three-dimensional STTO designs.

6

Conclusions

This thesis introduces a novel approach for detecting local overheating issues in Additive Manufacturing (AM) processes, which is integrated with a topology optimization (TO) framework. The method utilizes a geometry-based approach named "conductivity estimation" to capture element densities within the thermal interaction range. This allows the computation of local conductivity values for all elements in the design domain, which are then processed to create a "hotspot map" indicating areas of local overheating. Elevated elemental temperatures are indicative of low local conductivity, signifying potential overheating risks due to insufficient material for heat conduction. Notably, the simple nature of the filter domain allows pre-computation and placement outside the TO iteration loop, offering a significant computational advantage over existing hotspot detection techniques. While the method doesn't provide quantitative temperature estimates, a comparison with high-fidelity thermal simulations demonstrates its efficient detection of critical overheating zones. Consequently, it offers a qualitative assessment of local overheating concerns.

To proactively address heat accumulation issues during the design phase, the conductivity estimation approach is combined with TO. This integration involves using the method as a constraint, referred to as the "hotspot constraint," that limits maximum temperatures below critical thresholds. A geometric calibration determines the critical overhang angle based on feature size and desired temperature limits. This constraint remains active in overhang regions, where voids exist beneath solid elements while being easily satisfied elsewhere. As a result, the optimizer adjusts design variables beneath solid elements in overhang regions to reduce the degree of overhang, enhancing heat conduction pathways. The presented TO formulation emphasizes robustness and provides length-scale control over feature sizes. Unlike restrictive overhang filters, this approach doesn't enforce uniform overhang angles, thereby preserving design freedom and redistributing material to ensure a minimum local solid volume. The effectiveness of designs incorporating the hotspot constraint within robust TO is confirmed through transient thermal simulations, outperforming standard TO designs in mitigating local overheating. Moreover, leveraging pre-computed arrays of sensitivities and filters yields substantial computational gains. Extending the proposed hotspot constraint to three-dimensional scenarios is demonstrated, with minor modifications of the 2D formulation to accommodate a 3D environment. Notably, the decrease in structural stiffness in 3D designs remains minimal, underscoring their suitability for addressing overheating without compromising structural integrity.

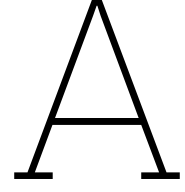
Finally, this conductivity estimation hotspot constraint is incorporated in space-time topology optimization designs. Here, not only the structural layout but also the fabrication sequence is optimized simultaneously in order to prevent local overheating. This helps us limit local overheating in manufactured structures using non-planar fabrication layers thus providing more design freedom. However, further research is needed to establish a framework for determining conductivity filter sizes based on material and process parameters to further refine the constraint.

References

- [1] Guido AO Adam and Detmar Zimmer. “Design for Additive Manufacturing Element transitions and aggregated structures”. In: *CIRP Journal of Manufacturing Science and Technology* 7.1 (2014), pp. 20–28.
- [2] Erik Andreassen, Anders Clausen, Mattias Schevenels, Boyan S Lazarov, and Ole Sigmund. “Efficient topology optimization in MATLAB using 88 lines of code”. In: *Structural and Multidisciplinary Optimization* 43 (2011), pp. 1–16.
- [3] Xingwang Bai, Paul Colegrove, Jialuo Ding, Xiangman Zhou, Chenglei Diao, Philippe Bridgeman, Jan roman Hönnige, Haiou Zhang, and Stewart Williams. “Numerical analysis of heat transfer and fluid flow in multilayer deposition of PAW-based wire and arc additive manufacturing”. In: *International Journal of Heat and Mass Transfer* 124 (2018), pp. 504–516.
- [4] M P Bendsøe and O Sigmund. Material interpolation schemes in topology optimization. Tech. rep.
- [5] Tyler E Bruns and Daniel A Tortorelli. “Topology optimization of non-linear elastic structures and compliant mechanisms”. In: *Computer methods in applied mechanics and engineering* 190.26-27 (2001), pp. 3443–3459.
- [6] Apratim Chakraborty, Reza Tangestani, Rasim Batmaz, Waqas Muhammad, Philippe Plamondon, Andrew Wessman, Lang Yuan, and Étienne Martin. “In-process failure analysis of thin-wall structures made by laser powder bed fusion additive manufacturing”. In: *Journal of Materials Science & Technology* 98 (2022), pp. 233–243.
- [7] Amal Charles, Ahmed Elkaseer, Lore Thijs, Veit Hagenmeyer, and Steffen Scholz. “Effect of process parameters on the generated surface roughness of down-facing surfaces in selective laser melting”. In: *Applied Sciences* 9.6 (2019), p. 1256.
- [8] Michele Chiumenti, Eric Neiva, Emilio Salsi, Miguel Cervera, Santiago Badia, Joan Moya, Zhuoer Chen, Caroline Lee, and Christopher Davies. “Numerical modelling and experimental validation in Selective Laser Melting”. In: *Additive Manufacturing* 18 (2017), pp. 171–185.
- [9] M Cloots, AB Spierings, and K Wegener. “Assessing new support minimizing strategies for the additive manufacturing technology SLM”. In: *2013 International Solid Freeform Fabrication Symposium*. University of Texas at Austin. 2013.
- [10] Tom Craeghs, Florian Bechmann, Sebastian Berumen, and Jean-Pierre Kruth. “Feedback control of Layerwise Laser Melting using optical sensors”. In: *Physics Procedia* 5 (2010), pp. 505–514.
- [11] Tom Craeghs, Stijn Clijsters, Jean-Pierre Kruth, Florian Bechmann, and Marie-Christin Ebert. “Detection of process failures in layerwise laser melting with optical process monitoring”. In: *Physics Procedia* 39 (2012), pp. 753–759.
- [12] G. Dhondt. *CalculiX CrunchiX UserS Manual Version 2.16*. 2020. URL: <http://www.dhondt.de/>.
- [13] Marcel Graf, Andre Hälsig, Kevin Höfer, Birgit Awiszus, and Peter Mayr. “Thermo-mechanical modelling of wire-arc additive manufacturing (WAAM) of semi-finished products”. In: *Metals* 8.12 (2018), p. 1009.
- [14] NE Hodge, RM Ferencz, and JM3218840 Solberg. “Implementation of a thermomechanical model for the simulation of selective laser melting”. In: *Computational Mechanics* 54.1 (2014), pp. 33–51.
- [15] Paul A Hooper. “Melt pool temperature and cooling rates in laser powder bed fusion”. In: *Additive Manufacturing* 22 (2018), pp. 548–559.
- [16] Paul Jaccard. “The distribution of the flora in the alpine zone. 1”. In: *New phytologist* 11.2 (1912), pp. 37–50.

- [17] Liu. Jikai, Gaynor. Andrew T, Chen. Shikui, Kang. Zhan, Suresh. Krishnan, Takezawa. Akihiro, Li. Lei, Kato. Junji, Tang. Jinyuan, and Wang. Charlie CL. “Current and future trends in topology optimization for additive manufacturing”. In: *Structural and multidisciplinary optimization* 57 (2018), pp. 2457–2483.
- [18] Darya Kastsian and D Reznik. “Reduction of local overheating in selective laser melting”. In: *Simulation for additive manufacturing Sim-AM*, Munich (2017).
- [19] Matthijs Langelaar. “Topology optimization of 3D self-supporting structures for additive manufacturing”. In: *Additive manufacturing* 12 (2016), pp. 60–70.
- [20] Matthijs Langelaar. “An additive manufacturing filter for topology optimization of print-ready designs”. In: *Structural and multidisciplinary optimization* 55 (2017), pp. 871–883.
- [21] Matthijs Langelaar. “An additive manufacturing filter for topology optimization of print-ready designs”. In: *Structural and Multidisciplinary Optimization* 55.3 (Mar. 2017), pp. 871–883. DOI: 10.1007/s00158-016-1522-2.
- [22] Boyan S Lazarov, Fengwen Wang, and Ole Sigmund. “Length scale and manufacturability in density-based topology optimization”. In: *Archive of Applied Mechanics* 86 (2016), pp. 189–218.
- [23] Chau Le, Julian Norato, Tyler Bruns, Christopher Ha, and Daniel Tortorelli. “Stress-based topology optimization for continua”. In: *Structural and Multidisciplinary Optimization* 41 (2010), pp. 605–620.
- [24] Martin Leary, Matthew McMillan, Darpan Shidid, Hans VanToor, Maciej Mazur, and Milan Brandt. “Numerical methods to predict overheating in SLM lattice structures”. In: *International Congress on Applications of Lasers & Electro-Optics*. AIP Publishing. 2014, pp. 895–902.
- [25] Kai Liu and Andrés Tovar. “An efficient 3D topology optimization code written in Matlab”. In: *Structural and Multidisciplinary Optimization* 50 (2014), pp. 1175–1196.
- [26] Topology optimization for additive manufacturing. Topology optimized aerospace bracket. URL: <https://d3i71xaburhd42.cloudfront.net/1bb56e8c9e8e5cbf8bbfcb935f1047ae42a048d9/3-Figure1-1.png>.
- [27] Raya Mertens, Stijn Clijsters, Karolien Kempen, and Jean-Pierre Kruth. “Optimization of scan strategies in selective laser melting of aluminum parts with downfacing areas”. In: *Journal of Manufacturing Science and Engineering* 136.6 (2014), p. 061012.
- [28] Filippo Montevecchi, Giuseppe Venturini, Niccolò Grossi, Antonio Scippa, and Gianni Campatelli. “Heat accumulation prevention in Wire-Arc-Additive-Manufacturing using air jet impingement”. In: *Manufacturing Letters* 17 (2018), pp. 14–18.
- [29] W Ou, GL Knapp, T Mukherjee, Y Wei, and T DebRoy. “An improved heat transfer and fluid flow model of wire-arc additive manufacturing”. In: *International Journal of Heat and Mass Transfer* 167 (2021), p. 120835.
- [30] LA Parry, IA Ashcroft, and RD Wildman. “Geometrical effects on residual stress in selective laser melting”. In: *Additive Manufacturing* 25 (2019), pp. 166–175.
- [31] Shubham Patel, James Mekavibul, Jami Park, Anchit Kolla, Ryan French, Zachary Kersey, and Gregory C Lewin. “Using machine learning to analyze image data from advanced manufacturing processes”. In: *2019 systems and information engineering design symposium (SIEDS)*. IEEE. 2019, pp. 1–5.
- [32] R Ranjan, C Ayas, M Langelaar, and F van Keulen. “Controlling local overheating in topology optimization for additive manufacturing”. In: *Structural and Multidisciplinary Optimization* 65.6 (2022), p. 162.
- [33] Rajit Ranjan, Can Ayas, Matthijs Langelaar, and Fred van Keulen. “Fast detection of heat accumulation in powder bed fusion using computationally efficient thermal models”. In: *Materials* 13.20 (2020), p. 4576.
- [34] Rajit Ranjan, Can Ayas, Matthijs Langelaar, and Fred van Keulen. “Fast detection of heat accumulation in powder bed fusion using computationally efficient thermal models”. In: *Materials* 13.20 (Oct. 2020), pp. 1–25. DOI: 10.3390/ma13204576.

- [35] Rajit Ranjan, Zhuoer Chen, Can Ayas, Matthijs Langelaar, and F Van Keulen. “Overheating control in additive manufacturing using a 3D topology optimization method and experimental validation”. In: *Additive Manufacturing* 61 (2023), p. 103339.
- [36] Ibiye Aseibichin Roberts. “Investigation of residual stresses in the laser melting of metal powders in additive layer manufacturing”. In: (2012).
- [37] Ole Sigmund. Design of Material Structures Using Topology Optimization Topology optimization for thermoelectric energy conversion problems View project Topology Optimization for Computational Fabrication View project. Tech. rep. 1994. URL: <https://www.researchgate.net/publication/261173987>.
- [38] Ole Sigmund. “Morphology-based black and white filters for topology optimization”. In: *Structural and Multidisciplinary Optimization* 33 (2007), pp. 401–424.
- [39] Ole Sigmund and Kurt Maute. Topology optimization approaches: A comparative review. Dec. 2013. DOI: 10.1007/s00158-013-0978-6.
- [40] Leandro João da Silva, Henrique Nardon Ferraresi, Douglas Bezerra Araújo, Ruham Pablo Reis, and Américo Scotti. “Effect of thermal management approaches on geometry and productivity of thin-walled structures of er 5356 built by wire+ arc additive manufacturing”. In: *Coatings* 11.9 (2021), p. 1141.
- [41] Felix Spranger, Benjamin Graf, Michael Schuch, Kai Hilgenberg, and Michael Rethmeier. “Build-up strategies for additive manufacturing of three dimensional Ti-6Al-4V-parts produced by laser metal deposition”. In: *Journal of Laser Applications* 30.2 (2018).
- [42] Krister Svanberg. “The method of moving asymptotes a new method for structural optimization”. In: *International journal for numerical methods in engineering* 24.2 (1987), pp. 359–373.
- [43] Truventor. URL: <https://blogs.truventor.ai/blogs/what-are-the-applications-of-additive-manufacturing/>.
- [44] JA Van Toor. “A knowledge based system to support design for selective laser melting”. PhD thesis. Delft University of Technology, 2014.
- [45] Di Wang, Yongqiang Yang, Ziheng Yi, and Xubin Su. “Research on the fabricating quality optimization of the overhanging surface in SLM process”. In: *The International Journal of Advanced Manufacturing Technology* 65 (2013), pp. 1471–1484.
- [46] Fengwen Wang, Jakob S Jensen, and Ole Sigmund. “Robust topology optimization of photonic crystal waveguides with tailored dispersion properties”. In: *JOSA B* 28.3 (2011), pp. 387–397.
- [47] Fengwen Wang, Boyan Stefanov Lazarov, and Ole Sigmund. “Correction: On projection methods, convergence and robust formulations in topology optimization”. In: *Structural and Multidisciplinary Optimization* 65.10 (2022), p. 278.
- [48] Weiming Wang, Dirk Munro, Charlie CL Wang, Fred van Keulen, and Jun Wu. “Space-time topology optimization for additive manufacturing: Concurrent optimization of structural layout and fabrication sequence”. In: *Structural and Multidisciplinary Optimization* 61 (2020), pp. 1–18.
- [49] Dongqing Yang, Gang Wang, and Guangjun Zhang. “Thermal analysis for single-pass multi-layer GMAW based additive manufacturing using infrared thermography”. In: *Journal of Materials Processing Technology* 244 (2017), pp. 215–224.
- [50] Yabin Yang, Xin Zhou, Quan Li, and Can Ayas. “A computationally efficient thermo-mechanical model for wire arc additive manufacturing”. In: *Additive Manufacturing* 46 (2021), p. 102090.
- [51] Wenyong Zhang, Mingming Tong, and Noel M Harrison. “Resolution, energy and time dependency on layer scaling in finite element modelling of laser beam powder bed fusion additive manufacturing”. In: *Additive Manufacturing* 28 (2019), pp. 610–620.
- [52] Mingdong Zhou, Yichang Liu, and Zhongqin Lin. “Topology optimization of thermal conductive support structures for laser additive manufacturing”. In: *Computer Methods in Applied Mechanics and Engineering* 353 (2019), pp. 24–43.



Appendix for Chapter-3

A.1. Influence of nonlinear weights and different conductivity filter size for the conductivity estimation method

The conductivity estimation method is combined with different linear and non-linear weights in order to understand the effect of neighboring elements as their distance changes from the central element whose local conductivity is being calculated. The elements which are far away from the central element of the filter have less contribution in conducting heat and hence they are penalized with a low weight. Conversely, the elements closer to the central element have a higher contribution to heat conduction and hence their influence is upsurged. The conductivity estimation without any weights is compared against one linear and three non-linear weight functions for three different filter radii of 6mm, 12mm, and 20mm. The geometry used is the same as that used in Section 3.2.5. The local conductivity combined with the weight functions is given by the equation,

$$\kappa_w^{(I)} \propto \frac{\sum_{J \neq I}^N \rho^{(J)} w^{(J)}}{\sum_{J \neq I}^N w^{(J)}} \quad \forall J \quad (\text{A.1})$$

The linear weight function w_1 is given by,

$$w_1 = r - |x_i^{(I)} - x_i^{(J)}| \quad \text{where } x_2^{(J)} < x_2^{(I)} \quad (\text{A.2})$$

The cosine weight function w_2 is given by,

$$w_2 = r \cos \left(\frac{|x_i^{(I)} - x_i^{(J)}| \pi}{2r} \right) \quad \text{where } x_2^{(J)} < x_2^{(I)} \quad (\text{A.3})$$

The inverse exponential weight function w_3 is given by,

$$w_3 = r \left(\frac{1}{1 + \exp((|x_i^{(I)} - x_i^{(J)}| - r)\lambda)} \right) \quad \text{where } x_2^{(J)} < x_2^{(I)} \quad (\text{A.4})$$

The exponentially decaying weight function w_4 is given by,

$$w_4 = r \exp(-\lambda |x_i^{(I)} - x_i^{(J)}|) \quad \text{where } x_2^{(J)} < x_2^{(I)} \quad (\text{A.5})$$

All these weights functions take a maximum value of the radius of the filter r and a minimum value of 0 as shown in Figure A.1. $|x_i^{(I)} - x_i^{(J)}|$ is the distance of the neighboring elements J with the central element of the filter I . Here, λ is a constant that controls the slope of the curve. In the linear weight function as given in Equation A.2, w_1 drops linearly as distance from the central element increases. For the cosine weight function as given in Equation A.3, w_2 drops slowly throughout as distance from center element increases. Thus influence of elements which are closer as well as farther away from the central

element is higher than when using linear weight function. In inverse exponential weight function given in Equation A.4, w_3 drops slowly till half the filter radius then drops quickly for remaining elements inside the filter. This is actually beneficial as a bigger filter radius can be used and elements which are close to the filter boundary are penalized heavily so their effect is negligible. In the exponentially decaying weight function given in Equation A.5, w_4 decreases strictly monotonically. The neighbouring elements are penalized heavily from the start and their influence is less compared to other weight functions. Thus, larger filter radius can be used and more features can be captured.

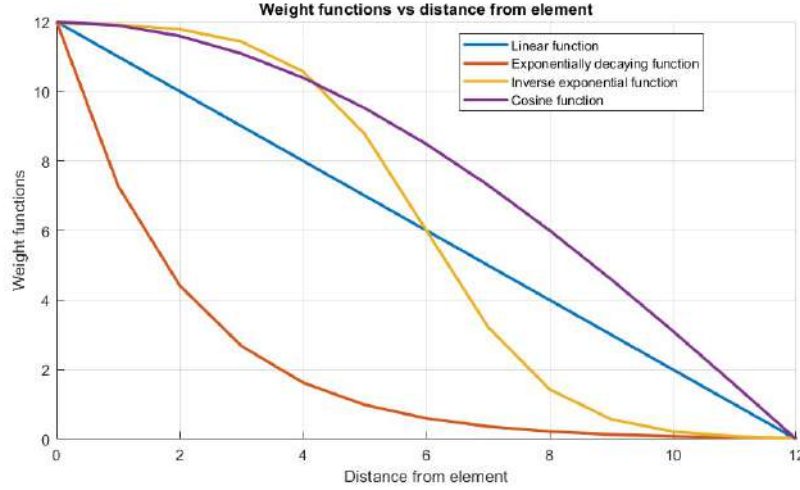
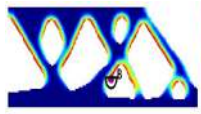
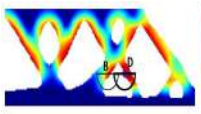
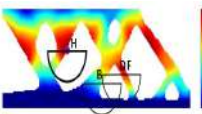
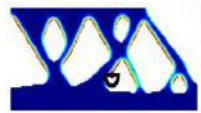
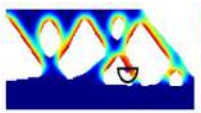
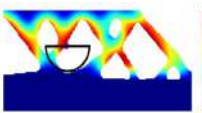
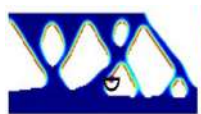
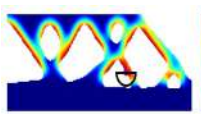
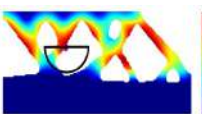
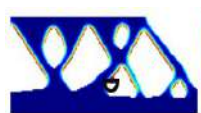
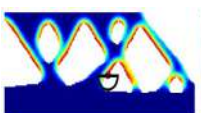
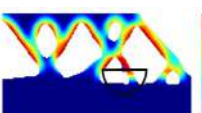

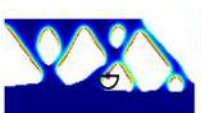
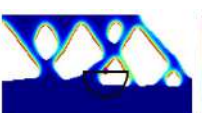


Figure A.1: Variation of weight functions vs distance from the element. The filter radius is taken as 12.

The variation of linear and non-linear weights in the conductivity estimation method for different filter radii is shown in Table A.1 and compared against the hotspot map of conductivity estimation without any weights. A baseplate with a width equal to the filter radius is added at the bottom for simulation so that the bottom layers have the correct local conductivity value. The problem with using conductivity estimation without weights was that using larger filter radii would incorporate neighboring features that do not contribute to heat evacuation. In linear and cosine weight functions, the influence of the elements which are at the boundary of the filter are not penalized much and therefore the hotspot map output and maximum temperature location are similar to that of conductivity estimation without weights. However, in the inverse exponential and exponentially decaying weight functions, the filter boundary elements are penalized heavily and we get a different hotspot map compared to the one without weights. Therefore, even though the 20mm filter is touching the neighboring overhang in the inverse exponential case similar to that of one with no weights, the overhang influence is neglected as it lies on the boundary of the filter.

The variation of the maximum temperature obtained for each hotspot map from Table A.1 is plotted against the filter radii used as shown in Figure A.2. The maximum temperature of conductivity estimation without weights increases linearly with increasing filter radii. Thus if we have to set a critical temperature value that is based on this maximum temperature for the hotspot constraint, it is dependent upon the filter radius used. Similar is the case for linear and cosine weight functions. However, for inverse exponential and exponentially decaying weight functions, the maximum temperature from different filter radii doesn't fluctuate much. Hence, the critical temperature is more or less independent of the filter radii.

Table A.1: Influence of linear and non-linear weights for different filter radii

Weight function	r=6	r=12	r=20
Without weights			
Linear weight function			
Cosine weight function			
Inverse exponential weight function			
Exponentially decaying weight function			

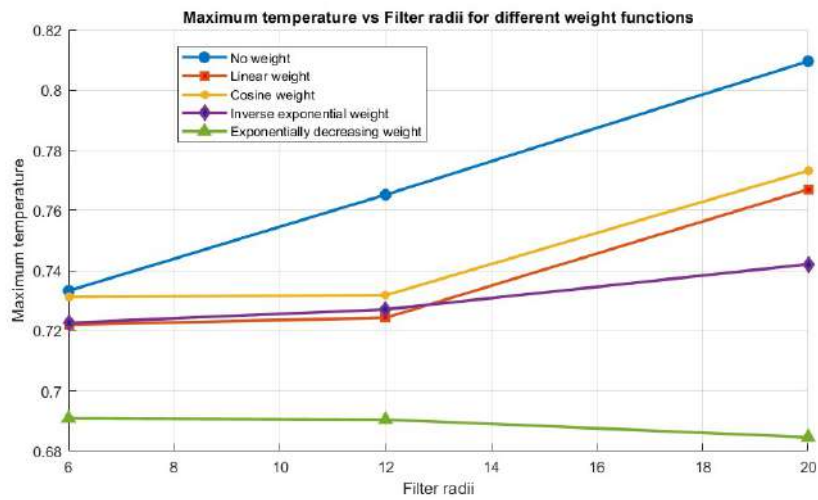


Figure A.2: Variation of maximum temperature vs filter radii for different weight functions.

A.2. Comparison of conductivity estimation method on geometry obtained from overhang filter

Another comparison of the conductivity estimation method with existing AM hotspot detection methods is shown in Figure A.3. The geometry used is the design obtained using the overhang filter in [21]. This geometry has a different set of features than the one used in Section 3.2.5. The geometry used has a constant overhang angle of 45° throughout the geometry. Even though the geometry has a single overhang angle, the heat accumulated zones are different throughout depending upon the features in the vicinity as seen from the transient thermal simulation in Figure A.3a. Similar to Section 3.2.5, the conductivity estimation method in Figure A.3e is compared against the transient thermal simulation in Figure 3.5a and the simplified steady-state slab analysis in Figure A.3c from [34]. The comparison metrics used were the Jaccard index given by Eqn 3.9 and the CZI maps. Again from Table A.2, the Jaccard index of the conductivity estimation method ($\hat{T}_{ref}, \hat{T}_{cest} = 44.93\%$) is lower than that of the slab analysis method ($\hat{T}_{ref}, \hat{T}_{slab} = 52.3\%$) wrt the transient simulation. But its relatively better than the Jaccard index obtained in Section 3.2.5. This is because, accuracy of the conductivity estimation method depends largely upon the conductivity filter radius chosen. Earlier, the filter size was small and the feature size was big compared to it so the conductivity filter would return a higher conductivity and thus, a lower temperature. But in this case, the feature size is relatively smaller and so due to larger voids around the feature, the conductivity filter would yield a lower conductivity and correspondingly a higher temperature. However, the CZI map of the conductivity estimation method in Figure A.3f is very similar to the transient simulation CZI map in Figure A.3b. This shows that the conductivity estimation method is capable enough to identify the critically heating zones and thus gives a good qualitative estimation of the overheating risks that may occur during AM process.

Table A.2: Jaccard index for different analysis

JJ	Slab analysis	Transient analysis
Conductivity estimation	$(\hat{T}_1, \hat{T}_2) = (\hat{T}_{slab}, \hat{T}_{cest}) = 49.82\%$	$(\hat{T}_1, \hat{T}_2) = (\hat{T}_{ref}, \hat{T}_{cest}) = 44.93\%$
Slab analysis	-	$(\hat{T}_1, \hat{T}_2) = (\hat{T}_{ref}, \hat{T}_{slab}) = 52.3\%$

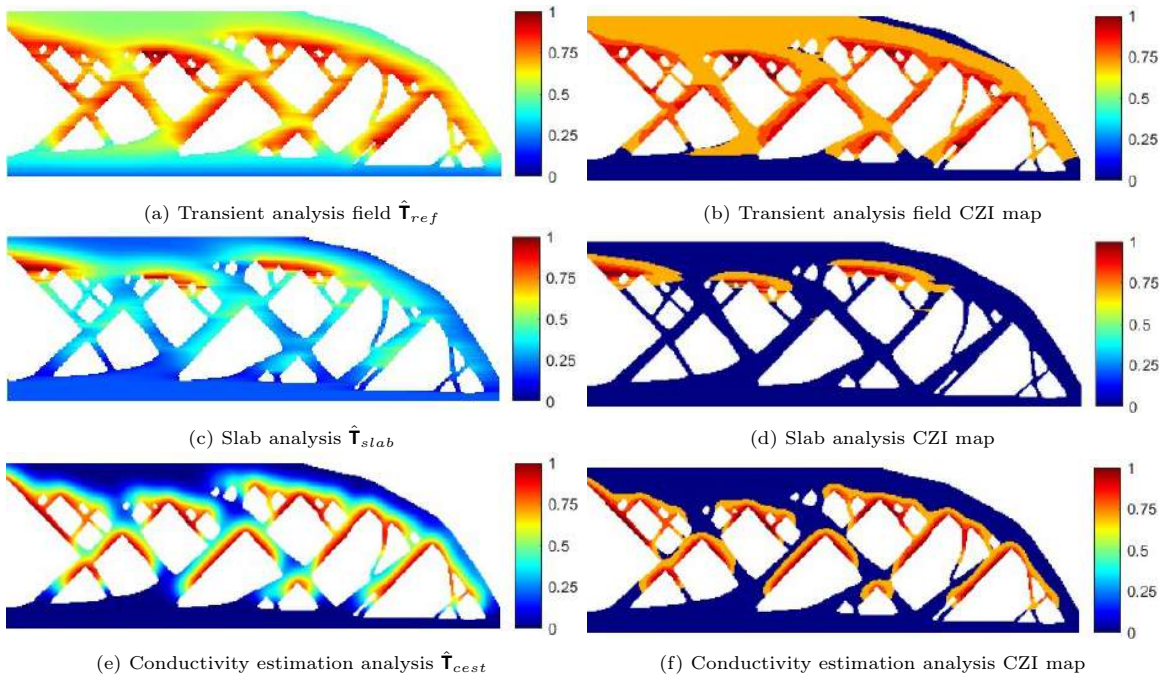


Figure A.3: Normalized temperature field, i.e., the hotspot maps for different analyses are presented in Figures 3.5a, 3.5c and 3.5e and the corresponding CZI maps are presented in Figures 3.5b, 3.5d and 3.5f.

A.3. Analytical sensitivities for the hotspot constraint

In numerical optimization, the gradient of the objective c and the constraint g respective to the design variable ϕ is needed. It is calculated using the chain rule as follows:

$$\frac{\partial c}{\partial \phi_e} = \sum_{i \in M_e} \left(\frac{\partial c}{\partial \rho_i} \frac{\partial \rho_i}{\partial \tilde{\phi}_i} \frac{\partial \tilde{\phi}_i}{\partial \phi_e} \right) \quad (\text{A.6})$$

$$\frac{\partial g}{\partial \phi_e} = \sum_{i \in M_e} \left(\sum_{j \in N_i} \left(\frac{\partial g}{\partial \gamma_j} \frac{\partial \gamma_j}{\partial \rho_i} \right) \frac{\partial \rho_i}{\partial \tilde{\phi}_i} \frac{\partial \tilde{\phi}_i}{\partial \phi_e} \right) \quad (\text{A.7})$$

where $\gamma(\bar{\mu}, \rho)$ in the conductivity estimation hotspot constraint given by Eqn 3.23. The objective function sensitivity $\frac{\partial c}{\partial \rho_i}$ can be evaluated as:

$$\frac{\partial c}{\partial \rho_i} = -p\rho_i^{p-1}(E_0 - E_{\min})u_i^T k_0 u_i \quad (\text{A.8})$$

The constraint function sensitivity $\frac{\partial g}{\partial \gamma_j} \frac{\partial \gamma_j}{\partial \rho_i}$ can be evaluated as:

$$\frac{\partial g}{\partial \gamma_j} = \frac{\alpha}{nT_{cr}} \left[\frac{1}{n} \sum_j^n ((1 - \bar{\mu}_j)\rho_j^r)^P \right]^{1/P-1} \quad (\text{A.9})$$

$$\frac{\partial \gamma_j}{\partial \rho_i} = \begin{cases} ((1 - \bar{\mu}_j)\rho_j^r)^{P-1} \left((1 - \bar{\mu}_j)r\rho_j^{r-1} - \frac{q\rho_j^{q-1}\rho_k^r w_k}{\sum_{k \in N_j} w_j} \right), & \text{if } i = j \\ -((1 - \bar{\mu}_j)\rho_j^r)^{P-1} \left(\frac{q\rho_j^{r+q-1}w_k}{\sum_{k \in N_j} w_j} \right), & \text{otherwise} \end{cases} \quad (\text{A.10})$$

The rest of the components can be evaluated as follows:

$$\frac{\partial \rho_i}{\partial \tilde{\phi}_i} = \beta \frac{1 - \tanh^2(\beta(\eta - \tilde{\phi}_i))}{\tanh(\beta\eta) + \tanh(\beta(1 - \eta))} \quad (\text{A.11})$$

$$\frac{\partial \tilde{\phi}_i}{\partial \phi_e} = \frac{\omega_{e,i}}{\sum_{k \in M_i} \omega_{k,i}} \quad (\text{A.12})$$

Note that, the densities utilized for the sensitivity analysis of the objective function pertain to the intermediate densities, while for the hotspot constraint sensitivity, the eroded densities are considered. Similarly, the η used in Eqn A.11 is η_i when used in objective function sensitivity and η_e when used in hotspot constraint sensitivity.

A.4. Hotspot constraint on eroded, intermediate, and dilated designs

The hotspot constraint given by Eqn 3.23 is applied on all three designs i.e. eroded, intermediate, and dilated in the robust formulation as shown in Figure A.4. The goal was to investigate the best design to implement the hotspot constraint. An intermediate threshold $\eta_i = 0.5$ and dilated threshold $\eta_d = 0.25$ was used for projection. From the relation, the eroded projection becomes $\eta_e = 1 - \eta_d = 0.75$. Since, the intermediate and dilated designs shown in Figures A.4b and A.4c respectively have to maintain a minimum feature size, the design freedom reduces. This results in minimal redistribution of material to minimize compliance while having to satisfy the constraints. Also, the constraint is artificially satisfied due to the presence of isolated features in the design domain. Since the eroded designs have the least feature size meaning the upper bound on feature thickness is lower and thus, the optimizer is able to redistribute the material quite efficiently. Furthermore, a reduction in volume leads to an increased risk of overheating among the three designs, representing the most unfavorable scenario. Thus, the conductivity estimation hotspot constraint exhibits optimal performance when applied to the eroded structure.

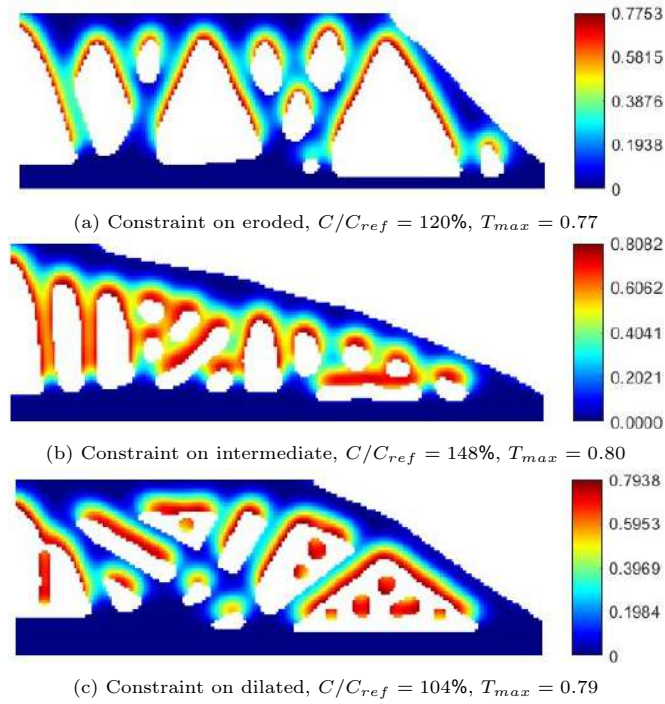


Figure A.4: Hotspot map generated using hotspot constraint on eroded, intermediate and dilated designs in the robust TO formulation.

A.5. Compliance and max temperature values for different q and r values

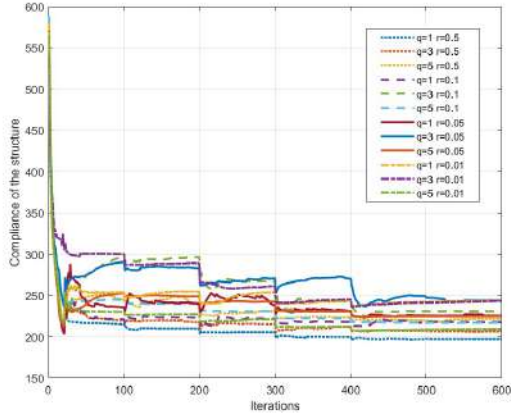


Figure A.5: Compliance plot of the structures with different q and r

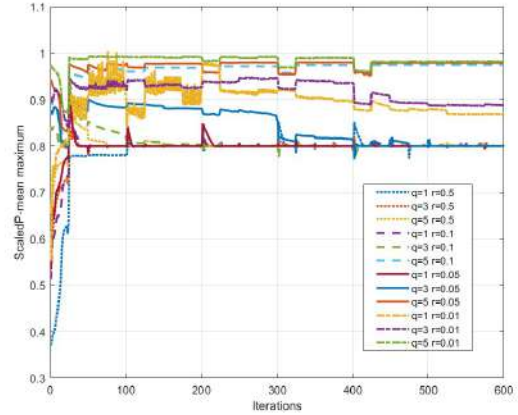


Figure A.6: Scaled P-mean maximum value of the structures with different q and r

A.6. Robust TO with hotspot constraint with different load cases and boundary conditions

The efficacy of the conductivity estimation hotspot constraint is examined across diverse design spaces, each characterized by distinct boundary conditions. This empirical investigation aims to assess the constraint's robustness and effectiveness in various spatial contexts. By subjecting the constraint to differing boundary conditions, we ascertain its adaptability and reliability across a spectrum of scenarios, contributing to a comprehensive understanding of its performance characteristics. The study involves testing three different boundary conditions and two build directions. All the designs are constrained to have a maximum temperature limit of $T_{cr} = 0.8$ that will restrict the geometry to have a critical overhang angle of $\theta_{cr} = 40^\circ$. The resulting geometries are then compared to structures without the hotspot constraint. The different boundary conditions are given in Figure A.7.

The designs from the three different load cases are given in Figure A.8. All the structures have a volume fraction of 0.4. The figures on the left indicate the design obtained using robust TO without any hotspot constraint. The figures on the right indicate the optimized structure preventing local overheating. Out of that, the top figures indicate a build direction which is from left to right along the x axis, and those at the bottom figures are built from bottom to top along the y axis. The designs without the hotspot constraint are post-analyzed using conductivity estimation to detect the zones prone to overheating. The build directions are taken care of by the orientation of the conductivity estimation filter, indicated by the red semicircle i.e. for left to right layer-by-layer deposition, the material will appear from the left, so the conductivity estimation is oriented such that it encapsulates the features that are printed. The size of the conductivity estimation filter was calculated based on the thermal interaction length.

The hotspot maps have the same colorbar range indicating pseudo temperature values from 0 to 1. It is clear that the designs without the hotspot constraint are prone to local overheating due to the presence of large overhangs and thin features. Even with a different build direction, these overheating zones are still encountered. The use of hotspot constraint suppresses the overheating-causing features and maintains a minimum local conductivity everywhere. Also, the overhangs don't go below the critical overhang angle of 40° . It is worth noting that, since the boundary conditions LC1 and LC3 are symmetrical about the x axis, the geometry obtained when the build direction is from left to right Figures A.8b and A.8j is stiffer than those obtained from bottom to top build Figures A.8d and A.8l. This is because the conductivity estimation filter is also symmetric about the x axis which results in redistribution of material in a symmetrical manner. This is not the case when the build direction is from bottom to top and the design freedom reduces. Moreover, it is not possible to always obtain a

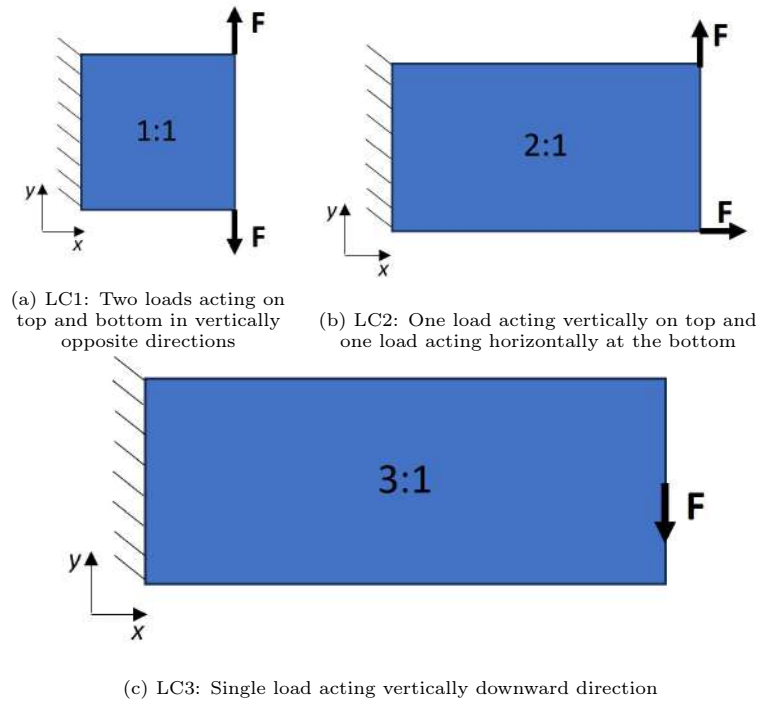


Figure A.7: Design spaces and boundary conditions for different analysis.

design that is free from local overheating in all build directions. For example in Figure A.8h, the hotspot constraint is getting violated ($T_{max} = 0.96$) as in order to minimize the compliance the optimizer has to add material in the region indicated by the black circle. As the design freedom is already reduced due to an asymmetrical loading and build direction, the hotspot constraint is not able to efficiently redistribute the material in that region leading to overhangs still existing in the design. Hence, a proper build direction should be chosen in order to get the required stiffness and overheating prevention in the designs based on the loading conditions.

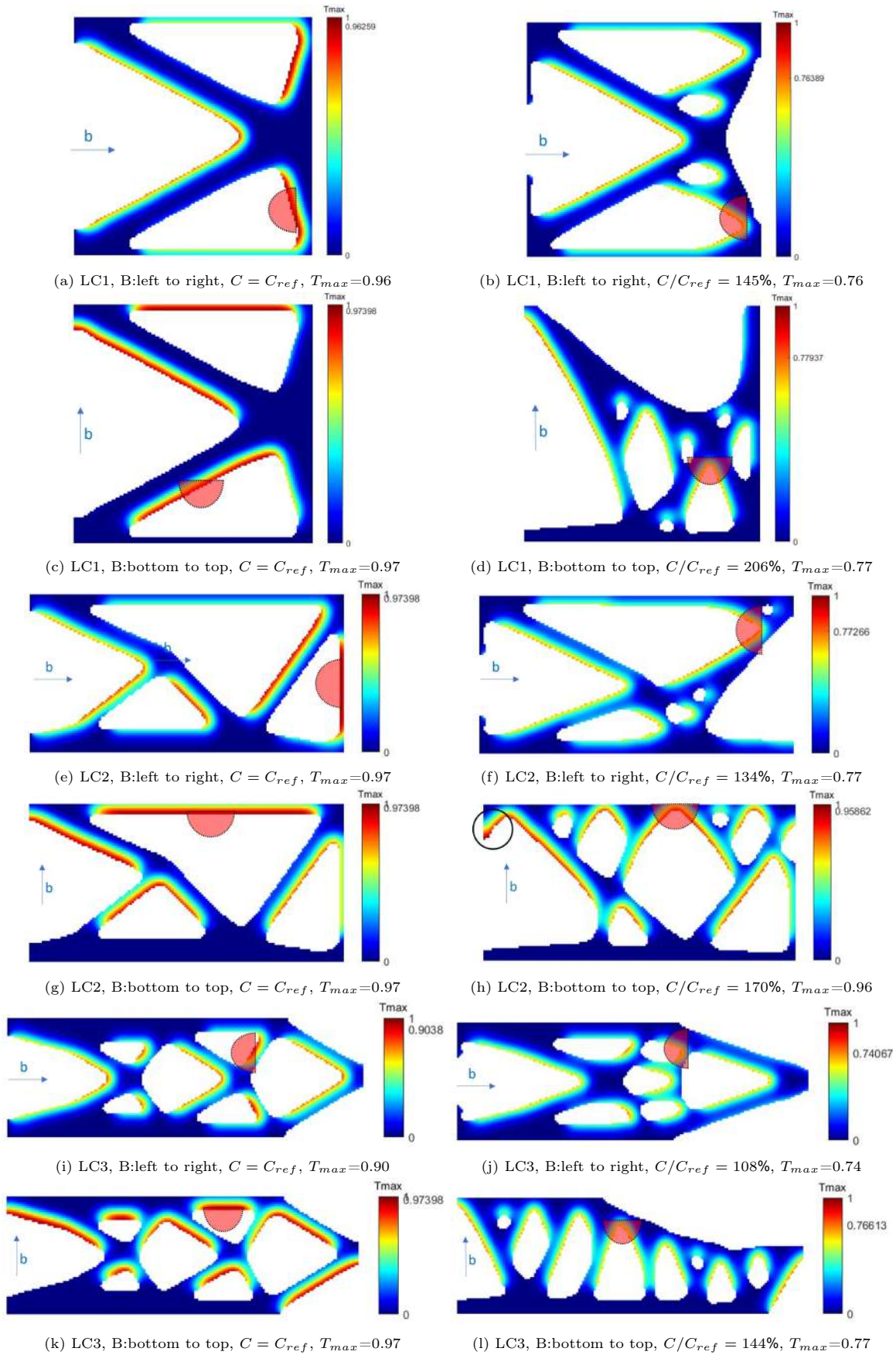


Figure A.8: Hotspot maps for designs obtained for boundary conditions LC1, LC2 and LC3. Figures A.8a, A.8c, A.8e, A.8g, A.8i and A.8j shows the structure w/o hotspot constraint and post-analyzed using conductivity estimation hotspot detection in two different build directions. Figures A.8b, A.8d, A.8f, A.8h, A.8j and A.8l shows the respective designs with hotspot constraint having the corresponding build direction. The red semicircle indicates the size of the conductivity estimation filter w.r.t. the design space and orientation are according to the build direction.

B

Appendix for Chapter-4

B.1. Analytical sensitivities for the hotspot constraint for STTO

The hotspot constraint given by Eqn 4.20 is differentiated w.r.t. the design variables ϕ and τ to get their sensitivities. The sensitivity w.r.t. the density field is given as:

$$\frac{\partial g}{\partial \phi_e} = \sum_{i \in M_e} \left(\sum_{j \in N_i} \left(\frac{\partial g}{\partial \zeta_j} \frac{\partial \zeta_j}{\partial \rho_i} \right) \frac{\partial \rho_i}{\partial \tilde{\phi}_i} \frac{\partial \tilde{\phi}_i}{\partial \phi_e} \right) \quad (\text{B.1})$$

where $\zeta(\bar{\psi}, \rho)$ in the conductivity estimation hotspot constraint. The component $\frac{\partial g}{\partial \gamma_j} \frac{\partial \gamma_j}{\partial \rho_i}$ can be evaluated as:

$$\frac{\partial g}{\partial \zeta_j} = \frac{\alpha}{n T_{cr}} \left[\frac{1}{n} \sum_j^n ((1 - \bar{\psi}_j) \rho_j^r)^P \right]^{1/P-1} \quad (\text{B.2})$$

$$\frac{\partial \zeta_j}{\partial \rho_i} = \begin{cases} ((1 - \bar{\psi}_j) \rho_j^r)^{P-1} \left((1 - \bar{\psi}_j) r \rho_j^{r-1} - \frac{q \rho_j^{q-1} \rho_k^r w_k \bar{\lambda}_k}{\sum_{k \in N_j} w_j \lambda_j} \right), & \text{if } i = j \\ -((1 - \bar{\psi}_j) \rho_j^r)^{P-1} \left(\frac{q \rho_j^{q-1} \rho_k^r w_k \bar{\lambda}_k}{\sum_{k \in N_j} w_j \lambda_j} \right), & \text{otherwise} \end{cases} \quad (\text{B.3})$$

The sensitivity w.r.t. the time field is given as:

$$\frac{\partial g}{\partial \tau_e} = \sum_{i \in M_e} \left(\sum_{j \in N_i} \left(\frac{\partial g}{\partial \zeta_j} \frac{\partial \zeta_j}{\partial \bar{\lambda}_j} \frac{\partial \bar{\lambda}_j}{\partial \tilde{\tau}_i} \right) \frac{\partial \tilde{\tau}_i}{\partial \tau_e} \right) \quad (\text{B.4})$$

where $\frac{\partial g}{\partial \zeta_j}$ is same as that in Eqn B.2. $\frac{\partial \zeta_j}{\partial \bar{\lambda}_j}$, $\frac{\partial \bar{\lambda}_j}{\partial \tilde{\tau}_i}$ are evaluated as:

$$\frac{\partial \zeta_j}{\partial \bar{\lambda}_j} = \begin{cases} ((1 - \bar{\psi}_j) \rho_j^r)^{P-1} \left(\frac{\sum_{k \in N_i} (\rho_k^q w_k \frac{\partial \bar{\lambda}_k}{\partial \tilde{\tau}_i}) - \bar{\psi}_j \sum_{k \in N_i} (w_k \frac{\partial \bar{\lambda}_k}{\partial \tilde{\tau}_i})}{\sum_{k \in N_i} w_j \lambda_j} \right), & \text{if } i = j \\ ((1 - \bar{\psi}_j) \rho_j^r)^{P-1} \left((\bar{\psi}_j - \rho_j^q) \left(\frac{w_k \rho_k^r}{\sum_{k \in N_i} w_j \lambda_j} \right) \frac{\partial \bar{\lambda}_j}{\partial \tilde{\tau}_i} \right), & \text{otherwise} \end{cases} \quad (\text{B.5})$$

where $\frac{\partial \bar{\lambda}_j}{\partial \tilde{\tau}_i}$ is given as:

$$\frac{\partial \bar{\lambda}_j}{\partial \tilde{\tau}_i} = -(1 + e^{\zeta(\bar{\tau}_j - \tilde{\tau}_i)}) \zeta e^{\zeta(\bar{\tau}_j - \tilde{\tau}_i)} \quad (\text{B.6})$$

The components $\frac{\partial \tilde{\phi}_i}{\partial \phi_e}$, $\frac{\partial \tilde{\tau}_i}{\partial \tau_e}$ from Eqn 4.3, 4.4 respectively are given as:

$$\frac{\partial \tilde{\phi}_i}{\partial \phi_e} = \frac{w(\mathbf{x}_i, r_d)v_i}{\sum_{k \in M_i} w(\mathbf{x}_i, r_d)v_i} \quad (\text{B.7})$$

$$\frac{\partial \tilde{\tau}_i}{\partial \tau_e} = \frac{w(\mathbf{x}_i, r_t)v_i}{\sum_{k \in M_i} w(\mathbf{x}_i, r_t)v_i} \quad (\text{B.8})$$